Magnetic anisotropy of transition metal based thin films investigated by magnetooptic Kerr effect

Dissertation (kumulativ)

zur Erlangung des Grades eines
Doktors der Naturwissenschaften (Dr. rer. nat.)

dem Fachbereich Physik der Universität Osnabrück
vorgelegt von

Timo Kuschel, Dipl. Phys.

Osnabrück, November 2011

for my family

'I headed down the track
my baggage on my back
I left the city far behind

walking down the road
with my heavy load
trying to find some peace of mind

father said:
you'll be sorry son
if you leave your home this way

and when you realize
the freedom money buys
you'll come running home some day'

Gary Cowton

Contents

1 Introduction

The discovery of the giant magneto resistance (GMR) in 1988 by Peter Grünberg [1] and simultaneously by Albert Fert [2] was one of the most important preconditions for the development of the spintronic research. This spin-dependent effect in a magnetic/non-magnetic/magnetic layer system is for example applied in computer hard drives.

If the non-magnetic layer is replaced by an insulating spacer the resulting spin-dependency of the electron tunneling probability is called tunneling magneto resistance (TMR). This effect was discovered by Michel Jullière in 1975 [3] and is the base of spin-dependent devices like magnetic tunnel junctions (MTJs), which are for example key components in magnetoresistive random access memory (MRAM) devices [4, 5].

In MTJs the tunnel barrier acts as a spin valve [6, 7] demonstrating the basic idea of spintronics. Here, the information carrier is the electron spin not the electron charge as in classical electronics. This concept led to further discoveries of spin-dependent effects in the recent years, for example the spin Hall effect [8, 9] and the inverse spin Hall effect [10]. The latest discovered spin-dependent effect is the spin Seebeck effect discovered by Ken-ichi Uchida in 2008 [11]. This spin caloric effect induces a spin current by a temperature gradient. Furthermore, a Seebeck effect can also be detected in MTJs which is called magneto Seebeck effect [12].

The most common materials of MTJ electrodes are based on transition metals like Co and Fe or on intermetallic compounds as $Co_{50}Fe_{50}$ [13, 14] due to their high Curie temperatures and huge spin polarizations. Epitaxial alloys used as electrode materials even increase the TMR effect of the MTJs [15, 16, 17]. Therefore, it is necessary to analyze the structural and magnetic properties of such magnetic films.

In the present work the properties of amorphous, polycrystalline and monocrystalline thin films composed of the transition metals Co and Fe are investigated. Here, the main focus of the research is on the magnetic anisotropy of the films and the magnetization reversal process if an external magnetic field is applied. The films are mainly probed by x-ray radiation and magnetooptic Kerr effect.

In order to extent the scientific field of the group of Prof. Wollschläger to magnetic thin films, a magnetooptic Kerr effect setup was built up during the diploma work of the present author [18]. In the current work this setup is further extended to perform vectorial magnetometry. Thus, the separated components of the magnetization vector can be obtained to determine the magnitude and the direction of the magnetization. Therefore, the complete magnetic reversal process can be reconstructed.

The theoretic background of magnetic thin films and of the main analysis techniques including magnetooptic Kerr effect, x-ray reflectivity and x-ray diffraction is explained in Chap. 2. While the investigated material systems are introduced in Chap. 3, the experimental details of the setups in Osnabrück and in Hamburg (DESY) are described in Chap. 4. Here, also the sample preparation techniques in Osnabrück and in Sendai (Japan) are presented.

The results are published in different scientific journals and included in the present cumulative thesis. The uniaxial magnetic anisotropy in amorphous and polycrystalline Co films of different thicknesses on glass is investigated in Chap. 5 (Ref. [19]). The improvement of the vectorial magnetometry technique including second order effects is presented in Chap. 6 (Ref. [20]). The processing is done by the example of crystalline Fe films on MgO. Here, an additional theoretic derivation verifies the developed measurement technique.

The magnetic properties of different annealed $\mathrm{Co_{50}Fe_{50}}$ films on MgO are characterized in Chap. 7 (Ref. [21]) by a detailed magnetooptic Kerr effect analysis including vectorial magnetometry and anisotropy studies using the Stoner-Wohlfarth model. Anomalous anisotropy behavior for a certain $\mathrm{Co_{50}Fe_{50}}$ film is discussed in Chap. 8 (Ref. [22]).

Further structural and magnetic results for the Fe films on MgO are additionally presented in Chap. 9. The thesis is concluded by a summary of the most important results and closed by an outlook to future investigations.

2 Theoretic background

In the theoretic part of the present thesis, the physical and mathematical background of the main analysis techniques used in this work are introduced. Magnetic thin films are investigated by magnetooptic Kerr effect to obtain magnetic properties (Chap. 2.2) and by x-ray radiation to determine the structural details of the film (Chap. 2.3). But first of all the typic structural and magnetic properties of thin films are reported in Chap. 2.1.

2.1 Thin films

Thin films are typically characterized by a film thickness of several micrometers down to the nanometer range including films of only one atomic layer, so-called monolayers. These thin films often have different structural and magnetic properties compared with bulk material. The structural classification of these films is summarized in Chap. 2.1.1 whereas thin film magnetism is described in Chap. 2.1.2.

2.1.1 Structural properties

Structural properties of thin films like the growth mode and the atomic lattice ordering are introduced in this chapter. The different types of growth affect the roughness of the film, which can be analyzed by x-ray reflectivity. The atomic structure in bulk samples and also in thin films can be amorphous, polycrystalline or monocrystalline. Additionally, the crystalline structure can be classified. The experimental technique for determination of the crystal structure used in this work is x-ray diffraction.

2.1.1.1 Types of thin film growth

There are three different basic types of thin film growth in a classic model of epitactic growth. These types differ in relation of surface tensions between adsorbate, substrate and interface. In Fig. 2.1(a) the surface tensions of adsorbate (γ_A), substrate (γ_S) and interface between adsorbate and substrate (γ_G) are shown.

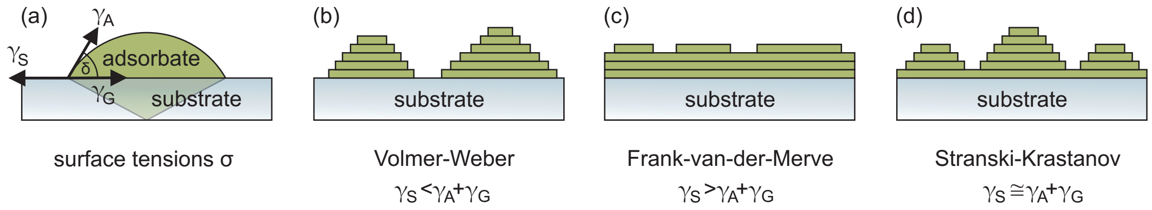

Figure 2.1: (a) Definition of the surface tensions γ and the contact angle δ. The different basic growth modes are (b) Volmer-Weber, (c) Frank-van-der-Merve and (d) Stranski-Krastanov.

For thermodynamic equilibrium it is given

$$\gamma_S = \gamma_A + \gamma_G \cos(\delta) \tag{2.1}$$

with contact angle δ between γ_A and γ_G. If $\gamma_S < \gamma_A + \gamma_G$, then the bondings between the adsorbate atoms are relatively strong compared to the bondings between the substrate atoms. Hence, the formation of adsorbate islands is favored which is pictured in Fig. 2.1(b) and called Volmer-Weber growth mode [23].

If $\gamma_S > \gamma_A + \gamma_G$, the bondings between the adsorbate atoms are relatively weak compared to the bondings between the substrate atoms. This leads to a layer-by-layer growth, the so-called Frank-van-der-Merve growth mode [24] as presented in Fig. 2.1(c).

A mix of both growth modes can occur in the case of similar surface tensions ($\gamma_S \cong \gamma_A + \gamma_G$). If the surface tension of the adsorbate is increasing during growth of the first layers due to relaxation of the atomic lattice, the initial layer-by-layer growth converts into an island growth. This type of growth mode is shown in Fig. 2.1(d) and named Stranski-Krastanov [25].

The surface tension of transition metals is relatively large compared to typic substrates used here (e.g. MgO(001) [26]). Thus, the Volmer-Weber growth is the most common type of thin film growth for these systems. Therefore, these films have a certain roughness which can be analyzed by x-ray reflectivity and atomic force microscopy.

2.1.1.2 Categorization of crystal structures

Each crystal structure can be expressed as a repeated set of atoms called atomic base. This base is ordered in a periodic three dimensional lattice as sketched in Fig. 2.2. The smallest arrangement of this lattice which can be repeated by defined translation operations is the unit cell. The characteristic lattice parameters are the length of the unit cell edges and the angles between them.

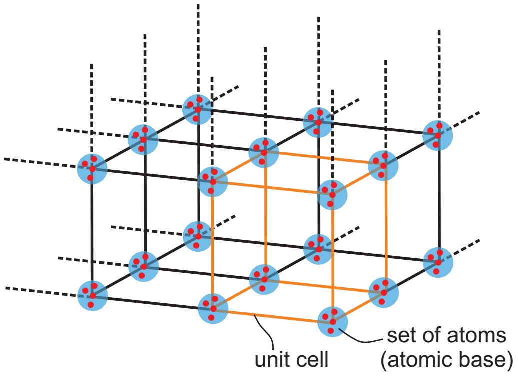

Figure 2.2: Definition of the crystal structure by an atomic base and a periodic lattice.

Bravais bulk lattices

In order to categorize the different crystal lattices one can distinguish them by their symmetry concerning rotation and inversion operations of the unit cell.

For example a cubic unit cell has a four-fold symmetry with respect to a rotation axis which connects the centers of two opposed sites, since the unit cell can be rotated by 90° to obtain the same structure. This rotation can be repeated four times until each atom is on its initial position, so it is called four-fold. There are three such four-fold symmetry axes in a cubic unit cell as shown in Fig. 2.3(a).

Furthermore, a cubic unit cell contains four three-fold symmetry axes (Fig. 2.3(b)). Each of them connects two opposed cubic summits. At last there are six two-fold symmetry axes in the cubic unit cell (Fig. 2.3(c)), which connects the centers of two opposed edges.

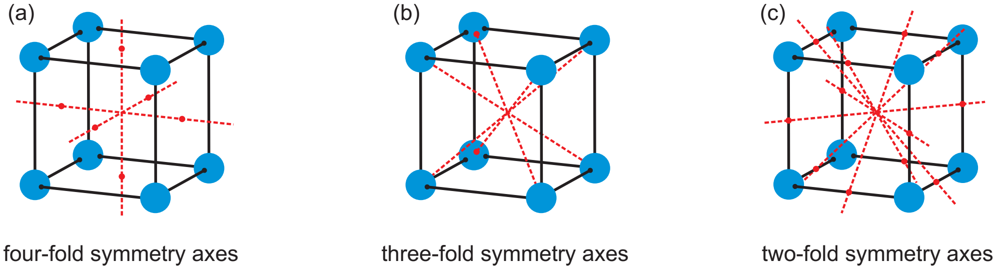

four-fold symmetry axes three-fold symmetry axes two-fold symmetry axes

Figure 2.3: Rotation symmetries for a cubic unit cell including (a) three four-fold symmetry axes, (b) four three-fold symmetry axes and (c) six two-fold symmetry axes.

Considering all rotation and inversion operations one can define 14 volume lattices named after Bravais, who assigned these 14 Bravais lattices into seven systems concerning the different symmetry properties [27]. These systems are triclinic, monoclinic, orthorhombic, rhombohedral, tetragonal, hexagonal and cubic. Since only the latter three systems are of importance in the present thesis, let us focus on them.

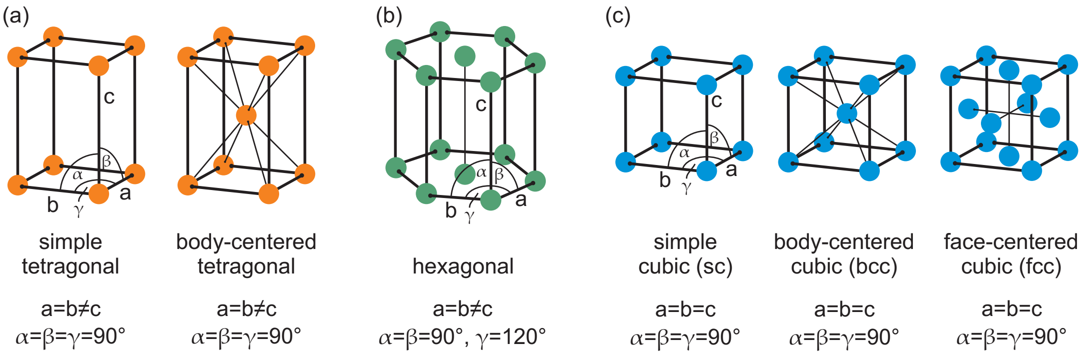

Figure 2.4: Six of the 14 Bravais lattices assigned in three of seven lattice systems: a) tetragonal system, (b) hexagonal system and (c) cubic system.

There are two types of tetragonal systems, a simple tetragonal lattice and a body-centered tetragonal lattice with square basal faces (lengths of unit cell $a = b \neq c$) as well as orthogonal edges (angles between them $\alpha = \beta = \gamma = 90°$) as sketched in Fig. 2.4(a). There is no base- or face-centered tetragonal unit cell, since they can also be expressed as simple or body-centered tetragonal unit cells, respectively. In the present work, this type of crystal lattice occurs when a cubic lattice of a thin film is tetragonal distorted due to pseudomorph growth on a slightly mismatched adsorbate.

The hexagonal unit cell with $a = b \neq c$, $\alpha = \beta = 90°$ and $\gamma = 120°$ is shown in Fig. 2.4(b). It represents one of two typic crystalline Co structures.

The cubic system in Fig. 2.4(c) shows a simple cubic lattice (sc), a body-centered cubic lattice (bcc) and a face-centered cubic lattice (fcc). Here, all edges of the unit cell have the same length ($a = b = c$) and are orthogonal ($\alpha = \beta = \gamma = 90°$). The favored crystalline structure of Fe is bcc and the second typic structure of crystalline Co is fcc.

Miller indices

The different directions in a certain lattice are indicated by Miller indices. These integer values denote a multiple of the length of the unit cell for each direction x_1, x_2 and x_3 along the edges of the unit cell. Thus, the described direction can always be expressed as a vector.

The common notation of directions in crystal lattices using Miller indices are square brackets. As an example the direction [1 2 1] for a simple cubic lattice is sketched in Fig 2.5(a). The plane perpendicular to this vector is the (1 2 1) plane, named after the normal direction.

The Miller indices of a plane can also be calculated by the points of intersection between the plane and the x_1-, x_2- and x_3-axes. In the example of Fig 2.5(a) the axes are intersected at $x_1 = 2$, $x_2 = 1$ and $x_3 = 1$. After determination of the reciprocal intersection values $1/x_1 = 1/2$, $1/x_2 = 1$ and $1/x_3 = 1$ the smallest set of integer values with the same ratios as the reciprocal intersection values is calculated. The obtained Miller indices are (1 2 1) which is consistent with the definition by the normal vector of the plane.

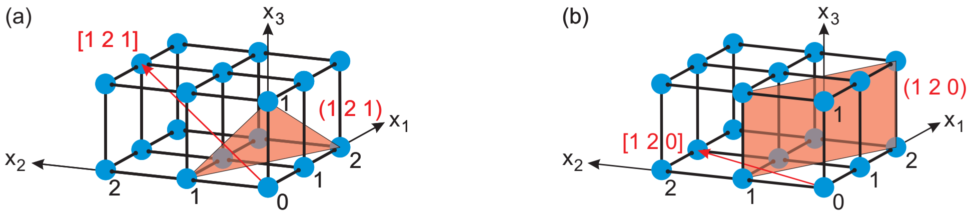

Figure 2.5: Definition of Miller indices. (a) First example is the direction [1 2 1] for a simple cubic lattice corresponding to the (1 2 1) plane which intersects the axes at $x_1 = 2$, $x_2 = 1$ and $x_3 = 1$. (b) Second example shows [1 2 0] corresponding to the (1 2 0) plane which intersects the axes at $x_1 = 2$, $x_2 = 1$ and $x_3 = \infty$ (no intersection with the x_3-axis).

A second example is shown in Fig 2.5(b). The direction [1 2 0] corresponds to the (1 2 0) plane which intersects the axes at $x_1 = 2$ and $x_2 = 1$. There is no intersection with the x_3-axis. Thus, the intersection value $x_3 = \infty$ with $1/x_3 = 0$ can be used to obtain the Miller indices.

Additional common notations are $\langle 1\,2\,0 \rangle$ for all equivalent directions with respect to [1 2 0] and $\{1\,2\,0\}$ representing all equivalent planes with respect to (1 2 0).

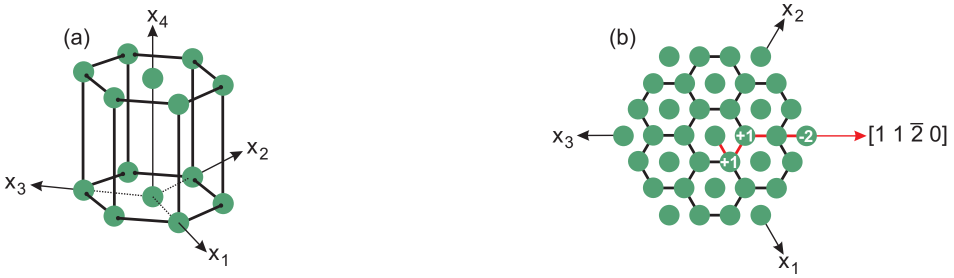

Figure 2.6: Definition of Miller indices for hexagonal crystal structures. (a) An additional in-plane axis is introduced (sideview). (b) As an example the $[1\,1\,\bar{2}\,0]$ direction is described (topview).

For hexagonal crystal structures there is an additional axis defined as presented in Fig. 2.6(a). The three in-plane axes x_1, x_2 and x_3 are connected by $x_3 = -(x_1 + x_2)$ [27]. Therefore, the direction of the negative x_3 axis has to be expressed by the Miller indices $[1\,1\,\bar{2}\,0]$ as constructed in Fig. 2.6(b). Generally, negative Miller indices are displayed by an overbar.

Bravais surface lattices

Surfaces can have different structural properties compared to the bulk structure of the same material. For example unsaturated bondings at the surface can result in reconstructions of the surface lattice. If these reconstructions change the surface lattice with respect to the unreconstructed surface, then the structure is called superstructure.

The surface lattices are classified into five Bravais lattices as summarized in Fig. 2.7. These lattices are square, rectangular, centered rectangular, hexagonal and oblique.

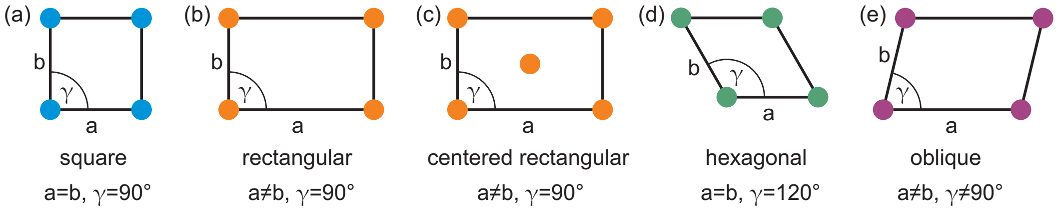

Figure 2.7: The five Bravais lattices for the classification of surface structures: (a) square, (b) rectangular, (c) centered rectangular, (d) hexagonal and (e) oblique.

Fig. 2.8 presents an example of a square surface lattice on the (001) surface of a fcc lattice with bulk lattice constant a_B. Since the edges of the surface unit cell is rotated by 45° with respect to the edges of the fcc lattice edges, the lattice constant of the surface unit cell is $a_S = a_B/\sqrt{2}$.

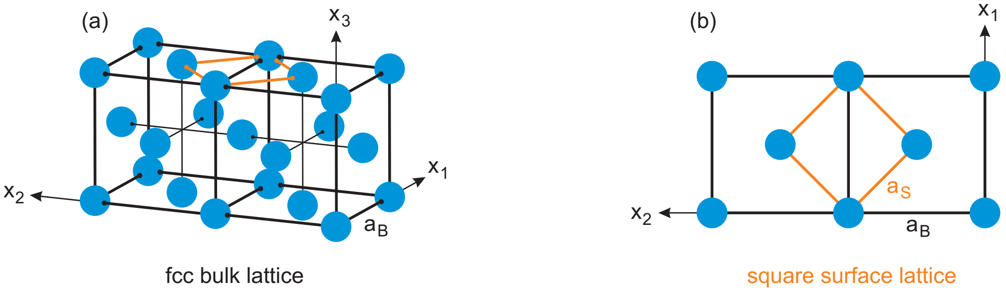

Figure 2.8: Square surface unit cell of the (001) surface of a fcc lattice. (a) Sideview of the fcc lattice with bulk lattice constant a_B. (b) Topview onto (001) surface of the fcc lattice with surface lattice constant $a_S = a_B/\sqrt{2}$.

2.1.2 Magnetic properties

Thin films have different magnetic properties compared to bulk material. This is originated in contributions of the surface and in properties of the thin film itself as explained in this chapter in the context of magnetic anisotropies. The magnetization of the film, which is affected by these magnetic anisotropies, is composed by the magnetic moments of magnetic domains in the sample. In this chapter the influence of magnetic domains during the reversal process of the sample magnetization is discussed.

As an introduction into thin film magnetism the ferromagnetism of the transition metals Fe, Co and Ni is described.

2.1.2.1 Ferromagnetism of Fe, Co and Ni

The electron configuration of Fe, Co and Ni is based on the Argon configuration. Furthermore, the complete 4s shell and at least half the 3d shell are occupied by electrons. The exact configuration is [Ar]$3d^6 4s^2$ for Fe, [Ar]$3d^7 4s^2$ for Co and [Ar]$3d^8 4s^2$ for Ni.

In solid states the energy niveaus overlap and form energy bands. For Fe, Co and Ni solids the 3d and 4s bands are decisive for the electric conductivity. The electrons within these bands contribute to the ferromagnetism by uncompensated spin states. Since these electrons are conduction electrons and therefore, not bound to the atomic cores, the orbital momentum is mainly irrelevant for the magnetic properties. Thus, the main contribution to the magnetic moments is yield by the spin of the conduction electrons.

The ferromagnetism of matter is originated in the parallel alignment of these magnetic moments which are generated by uncompensated spins of the electrons. The quantum mechanical origin of this parallel spin orientation is the exchange interaction explained in the following.

The Pauli principle signifies that the overall wave function of two electrons, which consists of spatial and spin part, has to be antisymmetric. Thus, either the spin part of the wave function has to be symmetric and the spatial part has to be antisymmetric or vice versa.

An antisymmetric spin part represents antiparallel spin orientation in connection with a symmetric spatial part which means electrons being localized very closely together. This is energetically unfavored due to the Coloumb repulsion between the charged particles which increases the potential energy. Therefore, an antisymmetric spatial part in connection with a symmetric spin part is favored at first sight.

But a symmetric spin part means parallel alignment of the spins. If several electrons have parallel spin, then they have to occupy different energetic states than for antiparallel alignment, since two particles with antiparallel spin can occupy the same energetic state. The occupation of more energy states increases the kinetic energy of the particles which is also not favored.

In conclusion, parallel alignment of the spin increases the kinetic energy, antiparallel alignment the potential energy. Thus, both alignments compete with each other. The system tries to minimize the total energy which is achieved either by totally compensated spins or by partially uncompensated spins.

Ferromagnetic material systems have partially uncompensated spins and therefore, a energetically different electronic structure for the different spin states (↑ and ↓) resulting in shifted density of states as sketched in Fig. 2.9. Thus, a majority of one spin state is obtained, if the Fermi level is adequate positioned. This is the base of ferromagnetism.

The transition metals Fe, Co and Ni fulfill these properties of the electronic structure and therefore, they are ferromagnetic.

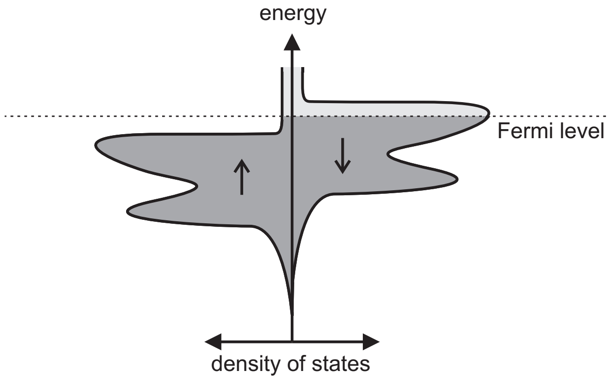

Figure 2.9: Schema for the density of states of a ferromagnetic material. The shifted density of states for the different spins (↑ and ↓) leads to a majority of one spin state, if the Fermi level is adequate positioned.

2.1.2.2 Magnetic anisotropy of thin films

The direction of the magnetization in a ferromagnet depends on several contributions which are summarized under the topic of magnetic anisotropy. These contributions define the energy density E. The magnetization $\vec{M}$ is aligned in the direction of the local minimum of E. This classic Stoner-Wohlfarth model [28] is valid for coherent rotation of the magnetization, i.e. the film has monodomain state and the magnitude of the magnetization vector is constant.

The energy density E is defined as

$$E = -\vec{H} \cdot \vec{M} + \sum_i E_i \tag{2.2}$$

with Zeeman term $-\vec{H} \cdot \vec{M}$ and anisotropy contributions E_i. For the minimum of E of isotropic media the magnetization $\vec{M}$ is aligned parallel to the external magnetic field $\vec{H}$. In anisotropic media the anisotropy contributions change the energy landscape and a different direction from $\vec{H}$ can be favored for $\vec{M}$.

The main anisotropy contributions for magnetic thin films are shape anisotropy, magnetocrystalline anisotropy, growth-induced uniaxial anisotropy, magnetoelastic anisotropy, interface anisotropy, and exchange bias, which are introduced in the following.

Shape anisotropy

Elongated samples prefer to be magnetized along the largest spatial expansion. For example, an iron bar prefers a magnetization direction along the elongation of the bar and thin films have in-plane magnetization, i.e. parallel to the sample surface. This effect is generated by the shape anisotropy which comes from the demagnetization field $\vec{B}_{\text{demag}}$ at the surface of the sample.

Here, the magnetic dipoles at the surface are uncompensated and form the demagnetization field, which is opposed to the external magnetic field. The contribution to the energy density E is

$$E_{\text{demag}} = -\int \vec{B}_{\text{demag}} \, d\vec{M} \ . \tag{2.3}$$

The demagnetization field $\vec{B}_{\text{demag}}$ can be described by

$$\vec{B}_{\text{demag}} = -\mu_0 \, \hat{\aleph} \, \vec{M} \tag{2.4}$$

with vacuum permeability μ_0 and demagnetization tensor $\hat{\aleph}$. For a thin film the magnetization component $M_\perp$ which is directed out-of-plane (normal to the sample surface) is decisive. Therefore, the integral of Eq (2.3) is solved with $\vec{B}_{\text{demag}} = -\mu_0 \, M_\perp$ to

$$E_{\text{demag}} = \frac{1}{2} \, \mu_0 \, M_\perp^2 \ . \tag{2.5}$$

The out-of-plane component $M_\perp$ of the magnetization can be expressed using saturation magnetization M_S, which equates to the magnitude of the magnetization vector and the angle $\vartheta_\perp$ between $\vec{M}$ and the normal of the sample surface. The result is

$$E_{\text{demag}} = \frac{1}{2}\,\mu_0\,M_S^2\,\cos^2\vartheta_\perp\ . \tag{2.6}$$

Since the shape anisotropy of thin films expressed in Eq. (2.6) is maximized for $\vartheta_\perp = 0°$ and minimized for $\vartheta_\perp = 90°$, the magnetization $\vec{M}$ is preferred in-plane aligned, if there are no other anisotropy contributions. If the magnetization vector is completely directed in-plane during the reversal process the shape anisotropy has no contributions to the energy density E, since E_{demag} is zero for $\vartheta_\perp = 90°$. This is the case for the samples investigated in the present work.

Magnetocrystalline anisotropy

The crystalline structure of the film induces an additional anisotropy due to the spin-orbit interaction. If there are no other anisotropy contributions the magnetocrystalline anisotropy makes the magnetization align along a defined direction with respect to the crystal structure.

For a hexagonal crystal structure, e.g. for crystalline Co films, the magnetocrystalline contribution is [29]

$$E_{\text{hex}} = K_1\,\sin^2\vartheta_{\text{hex}} + K_2\,\sin^4\vartheta_{\text{hex}} \tag{2.7}$$

with the angle ϑ_{hex} between magnetization $\vec{M}$ and the hexagonal c-axis (cf. Chap. 2.1.1.2). Furthermore, K_1 and K_2 are material- and temperature-dependent anisotropy coefficients. For positive K_1 and K_2 the c-axis ($\vartheta_{\text{hex}} = 0°$) is the preferred direction for $\vec{M}$, if no other anisotropy contributes. Then the anisotropy is called uniaxial.

The magnetocrystalline anisotropy for cubic crystal structures is defined as [30]

$$E_{\text{cub}} = K_1\,\left(\alpha_1^2\,\alpha_2^2 + \alpha_2^2\,\alpha_3^2 + \alpha_3^2\,\alpha_1^2\right) + K_2\,\alpha_1^2\,\alpha_2^2\,\alpha_3^2 \tag{2.8}$$

using the direction cosines α_1, α_2 and α_3 with respect to the edges of the cubic structure. For example, the [100] direction in the bcc lattice of crystalline Fe structures is the energetic favored direction for $\vec{M}$, while in the fcc lattice of crystalline Ni the favored direction for $\vec{M}$ is the [111] direction. This anisotropy is fourfold due to the cubic crystal structure.

If the sample magnetization is strictly in-plane aligned due to the shape anisotropy, the three dimensional magnetocrystalline anisotropy converts into a two dimensional one. Therefore, one magnetization component is permanently zero. Thus, for a cubic crystal structure Eq. (2.8) is simplified to

$$E_{\text{cub}} = K_1\,\left(\alpha_1^2\,\alpha_2^2\right) = K_1\,\left(\cos^2\vartheta\,\sin^2\vartheta\right) = \frac{K_1}{4}\sin^2 2\vartheta\ . \tag{2.9}$$

Here, the angle ϑ describes the direction of $\vec{M}$ with respect to a specific crystal direction.

Growth-induced uniaxial anisotropy

A permanent preferred axis for the magnetization can be induced during sample preparation by oblique deposition or external magnetic fields [31, 32]. But also substrate shape, vicinal surfaces or strain in the substrate can cause this growth-induced anisotropy [33, 19]. In most cases it can be described by a uniaxial anisotropy contribution, which is

$$E_{\text{uni}} = K_U \, \sin^2(\vartheta - \vartheta_U) \; . \tag{2.10}$$

Here again, the angle ϑ describes the direction of $\vec{M}$ with respect to a specific crystal direction and ϑ_U defines the direction of energetic minimum for the uniaxial anisotropy. The uniaxial anisotropy coefficient K_U expresses the strength of this contribution to the energy density E. A detailed analysis of the uniaxial anisotropy for amorphous and polycrystalline Co on glass is part of the present thesis and presented in Chap. 5 (published in Ref. [19]).

Magnetoelastic anisotropy

If a crystal is deformed by shearing, a magnetoelastic anisotropy can be induced. The contribution to the energy density is [30]

$$E_{\text{ela}} = B_1 \, \left(\alpha_1^2 \, \epsilon_{11}^{\text{ela}} + \alpha_2^2 \, \epsilon_{22}^{\text{ela}} + \alpha_3^2 \, \epsilon_{33}^{\text{ela}}\right) + B_2 \, \left(\alpha_1 \, \alpha_2 \epsilon_{12}^{\text{ela}} + \alpha_2 \, \alpha_3 \epsilon_{23}^{\text{ela}} + \alpha_3 \, \alpha_1 \epsilon_{31}^{\text{ela}}\right) \tag{2.11}$$

using the magnetoelastic coupling coefficients B_1 and B_2 and the elements of the elasticity tensor $\hat{\epsilon}^{\text{ela}}$. The magnetoelastic anisotropy can be neglected in the present study, since we only obtain tetragonal distortion of some sample lattices which results in a cubic magnetooptical in-plane anisotropy due to the shape anisotropy.

Interface anisotropy

For ultra thin films there is a interface anisotropy generated by the spin-orbit interaction due to symmetry break of the crystal structure at the interfaces. This anisotropy can be stronger than the shape anisotropy and cause a preferred out-of-plane magnetization for ultra thin films. If this is valid, the magnetocrystalline anisotropy coefficient K_1 is composed by a volume contribution K_1^{vol} and an interface contribution K_1^{if} depending on the thickness D of the film. One can summarize both contributions to an effective magnetocrystalline anisotropy coefficient K_1^{eff} which is

$$K_1^{\text{eff}} = K_1^{\text{vol}} + \frac{2}{D} \, K_1^{\text{if}} \; . \tag{2.12}$$

Since the here investigated samples are mostly in-plane aligned, the interface anisotropy is irrelevant compared to the shape anisotropy and can be neglect. Therefore, the samples are not thin enough to show an influence on the interface anisotropy.

Exchange bias

If an antiferromagnetic layer is coupled to the investigated ferromagnetic film, the exchange bias effect can occur. The magnetic moments are pinned in one direction and the reversal process of the magnetization is asymmetric with respect to the sign of the external magnetic field, i.e. the external field for reaching the magnetic saturation has a different absolute value for positive and negative field. This effect is unidirectional, which describes a one-fold anisotropy. Since no antiferromagnetic layers are used here, exchange bias is neglected.

Energy density used in the present work

Summarizing the relevant anisotropies mentioned above for the present study, the resulting energy density for a thin film with cubic structure is [34]

$$E = -\vec{H} \cdot \vec{M} + E_{\text{cub}} + E_{\text{uni}} = -\vec{H} \cdot \vec{M} + \frac{K_1}{4} \sin^2 2\vartheta + K_U \sin^2(\vartheta - \vartheta_U) \ . \tag{2.13}$$

There are several ways to obtain the anisotropy constants K_1 and K_U for specific directions ϑ_U of the uniaxial anisotropy. One of these processing methods will be introduced in Chap. 2.1.2.4 after the reversal process of the magnetization is described in more details.

2.1.2.3 Magnetic domains and reversal process

The magnetic moments of a ferromagnet are arranged in magnetic domains, so-called Weiss domains. Within such a domain all magnetic moments are parallel aligned in the direction of the minimum energy density. Neighboring domains have different alignment of magnetic moments. They are separated by walls where the magnetic moments rotate from the alignment of one neighboring domain to the alignment of the other neighboring domain. If this rotation is completely in-plane the domain wall is called Neel Wall. If during rotation the magnetic moments are aligned out-of-plane the domain wall is a Bloch wall. Weiss domains have an expansion of about 10^{-8} m to 10^{-6} m. The domain wall between them can have a thickness of 10^{-9} m [29].

If an external magnetic field is applied the domain walls between the magnetic domains move. Thus, magnetic domains can change their size. They also can appear or disappear, if the external field is varied. The existence of different magnetic domains is called multidomain state. For a very large external magnetic field the magnetic moments are all aligned parallel to the external field direction. This is a monodomain state with no Bloch or Neel walls anymore. In this situation, all anisotropy contributions are overcome and only the Zeeman term of the energy density (cf. Eq. (2.2)) defines the minimum of the energy density.

The movement of the domain walls can be influenced for example by defects in the crystal structure. Thus, changing the external magnetic field is a partially irreversible process. This hysteretic behavior can be visualized by a magnetization curve which presents the magnetization M in dependence on the external magnetic field H. A typical magnetization curve for a magnetic reversal process is shown in Fig. 2.10 labeled by the significant values of saturation magnetization M_S, magnetic remanence M_R, switching fields H_S, and coercive field H_C. The different curves for increasing and decreasing external field represent the hysteretic behavior of the magnetization curve.

In saturation magnetization M_S all magnetic moments are parallel aligned, which is the monodomain state. If the external field is decreased, the magnetization also decreases. The origin is the formation of multidomain states. The magnetic moments are aligned in different directions and hence, the magnetization as the sum of the magnetic moments is decreased. For non-integrable measurement techniques (as for example for magnetooptic Kerr effect) there can be a second cause for the decrease of magnetization. Since only one magnetization component is detected in some cases, the decrease of magnetization can be originated by a coherent

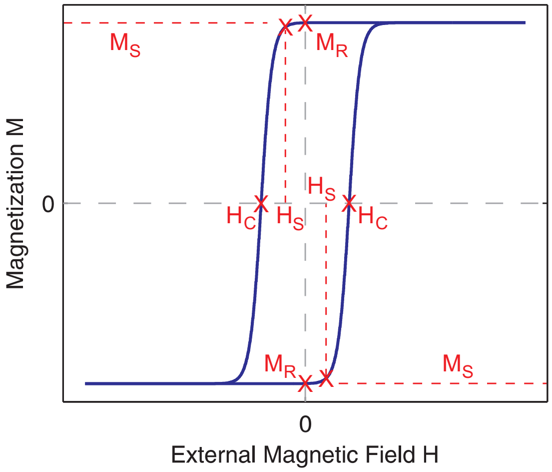

Figure 2.10: Typic magnetization curve with hysteretic behavior. The saturation magnetization M_S, the magnetic remanence M_R, the coercive field H_C and the switching field H_S are marked.

rotation of the magnetization (keeping the monodomain state). Thus, the projection of the magnetization to the sensitive detection direction reduces the measured magnetization value.

If the external field vanishes the remaining magnetization is the magnetic remanence M_R. After applying a reversed external field the magnetization switches into another direction. The external field which causes this switching is named switching field H_S. When the external field is increased, the magnetic moments can be summed up to zero, since the opposed directions of magnetic moments in the different domains annihilate themselves during summation. The external field which induces this vanishing magnetization is called coercive field H_C. There is also a second interpretation for non-integrable measurement techniques. The magnetization can be aligned perpendicular to the sensitive detection direction. Thus, the projection is zero.

If the external field is further increased in the reversed direction, monodomain state is formed again and the opposed saturation magnetization is reached. The second part of the magnetization curve can be explained in the same way. In order to distinguish coherent rotation of the magnetization and formation of multidomain states as an interpretation of the magnetization decrease, vectorial magnetometry should be performed. This technique can reconstruct the magnetization vector including direction and magnitude as will be explained in Chap. 2.2.2.

The magnetic anisotropy contributions introduced in Chap. 2.1.2.2 form an energy landscape with preferred directions for the magnetization (magnetic easy axes) and energetic disadvantageous directions (magnetic hard axes). Typic magnetization curves in a magnetic easy and hard axis are presented in Fig. 2.11. A magnetic easy axis (Fig. 2.11(a)) is characterized by a large remanence and a large coercive field. The magnetization curve has square-like shape. The state of the magnetization in magnetic remanence is the same as in saturation magnetization. One can write $M_R \approx M_S$ in magnetic easy direction. In magnetic hard direction (Fig. 2.11(b)) both magnetic remanence and coercive field are smaller than in magnetic easy direction. The magnetization curve has no square-like shape anymore, but is more rounded.

The magnetic remanence differs significantly from the saturation magnetization.

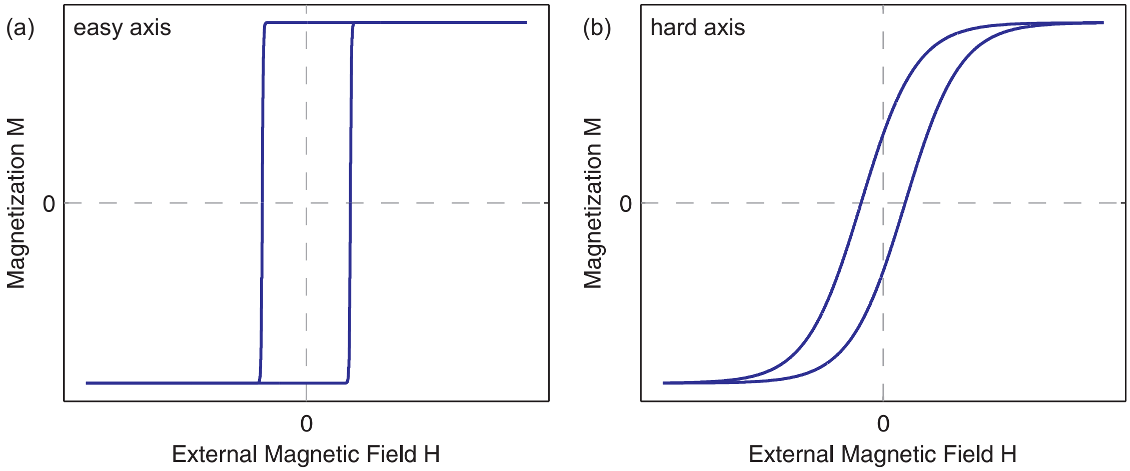

Figure 2.11: Typic magnetization curves for (a) magnetic easy and (b) magnetic hard axis.

2.1.2.4 Determination of anisotropy constants from magnetization curves of different sample directions

In the present work, the anisotropy constants are obtained by measuring magnetization curves of different sample directions of the investigated thin films with cubic crystal structure. From the energy density of Eq. (2.13) one can determine the anisotropy constants K_U of the uniaxial magnetic anisotropy (UMA) and K_1 of the cubic magnetic anisotropy (CMA). This processing is described in detail in Chap. 7 (Ref. [21]) and summarized in the following for the case of UMA parallel to one of the magnetic easy axes of the CMA.

In Fig. 2.12 a CMA superimposed by a UMA parallel to one of the magnetic easy axes of the CMA is sketched resulting in a more easy axis and less easy axis. This parallel alignment defines the CMA angle $\vartheta_U = 0°$ of Eq. (2.13). Three relevant angles are defined. The angle ϑ is the common magnetization angle (cf. Eq. (2.13)) between the magnetization $\vec{M}$ and a specific crystal axis which is one of the magnetic easy axes of the CMA and defined as 0° direction of crystal structure. The angle $\gamma = \alpha - \vartheta$ is the rotation angle of $\vec{M}$ with respect to the external field $\vec{H}$ and the angle α is the azimuthal sample angle between the 0° direction of crystal structure and $\vec{H}$.

Determination of UMA constant K_U

For determination of K_U we convert Eq. (2.13) into an equation $E(\vartheta)$ by using $\vec{H} \cdot \vec{M} = H\, M_S \cos(\alpha - \vartheta)$. The result for $\vartheta_U = 0°$ is

$$E(\vartheta) = \frac{K_1}{4} \sin^2 2\vartheta + K_U \sin^2(\vartheta) - H M_S \cos(\alpha - \vartheta) \; . \tag{2.14}$$

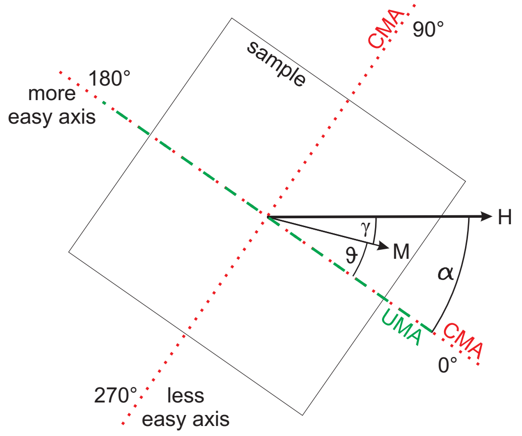

Figure 2.12: Magnetic axes for a UMA parallel to one of the magnetic easy axes of the CMA. This results in a more easy axis and a less easy axis. Three relevant angles are defined: ϑ between $\vec{M}$ and the 0° direction of the crystal structure, γ between $\vec{H}$ and $\vec{M}$) as well as α between $\vec{H}$ and the 0° direction of the crystal structure.

The energy for a magnetic switch from one magnetic easy axis to another can be obtained by Eq. (2.14), if the start and the end of the switching can be described by a monodomain state, since Eq. (2.14) is only valid for monodomain states. This energy is the domain wall pinning energy which is the energy concerning the nucleation of a multidomain state and can be calculated by the difference of the energy at the beginning and the end of the switching [35].

The domain wall pinning energy ϵ_{90° for a 90° switching of the magnetization vector from $\vartheta = 0^\circ$ to $\vartheta = 90^\circ$ (upper signs) and from $\vartheta = 90^\circ$ to $\vartheta = 0^\circ$ (lower signs) is

$$\epsilon_{90^\circ} = \pm E(\vartheta = 0^\circ) \mp E(\vartheta = 90^\circ) = \mp K_U \mp H_S^{0^\circ \longrightarrow 90^\circ/90^\circ \longrightarrow 0^\circ} M_S(\cos\alpha - \sin\alpha) \quad (2.15)$$

with switching field $H_S^{0^\circ \longrightarrow 90^\circ/90^\circ \longrightarrow 0^\circ}$ using upper signs in Eq. (2.15) for the switching $0^\circ \longrightarrow 90^\circ$ and lower signs for the switching $90^\circ \longrightarrow 0^\circ$.

The domain wall pinning energies of the other 90° switchings can be calculated in the same way. Therefore, the switching fields for all eight possible switchings are

$$\begin{aligned}
H_S^{0^\circ \longrightarrow 90^\circ/90^\circ \longrightarrow 0^\circ}(\alpha) &= \frac{\mp\epsilon_{90^\circ} - K_U}{M_S(\cos\alpha - \sin\alpha)} \;, \\
H_S^{90^\circ \longrightarrow 180^\circ/180^\circ \longrightarrow 90^\circ}(\alpha) &= \frac{\mp\epsilon_{90^\circ} + K_U}{M_S(\cos\alpha + \sin\alpha)} \;, \\
H_S^{180^\circ \longrightarrow 270^\circ/270^\circ \longrightarrow 180^\circ}(\alpha) &= \frac{\pm\epsilon_{90^\circ} + K_U}{M_S(\cos\alpha - \sin\alpha)} \quad \text{and} \\
H_S^{270^\circ \longrightarrow 0^\circ/0^\circ \longrightarrow 270^\circ}(\alpha) &= \frac{\pm\epsilon_{90^\circ} - K_U}{M_S(\cos\alpha + \sin\alpha)} \;. \qquad (2.16)
\end{aligned}$$

These eight switching fields can be summarized to two independent switching fields as presented in Chap. 7 (Ref. [21]) due to symmetry reasons. Thus, the reciprocal residual switching fields H_A and H_B depending on the azimuthal sample angle α describe a sine shaped behavior. We obtain

$$\frac{1}{H_{A/B}(\alpha)} = A_{A/B}\,\sin(\frac{\pi}{4}+\alpha) \tag{2.17}$$

with the amplitudes

$$A_{A/B} = -\,\frac{\sqrt{2}\,M_S}{\epsilon_{90^\circ} \pm K_U}\ . \tag{2.18}$$

After fitting the experimentally obtained reciprocal switching fields $H_{A/B}$, the scaled domain wall pinning energy ϵ_{90°/M_S and UMA constant K_U/M_S can be calculated by these amplitudes $A_{A/B}$ via

$$\begin{aligned} \frac{\epsilon_{90^\circ}}{M_S} &= -\frac{1}{\sqrt{2}}\left(\frac{1}{A_B}+\frac{1}{A_A}\right) \qquad \text{and} \\ \frac{K_U}{M_S} &= \frac{1}{\sqrt{2}}\left(\frac{1}{A_B}-\frac{1}{A_A}\right)\ . \end{aligned} \tag{2.19}$$

Determination of CMA constant K_1

For determination of K_1 we convert Eq. (2.14) from $E(\vartheta)$ into an equation $E(\gamma)$ using $\gamma = \alpha - \vartheta$. For $\vartheta_U = 0^\circ$ (UMA parallel to one of the CMA easy axes) we obtain

$$E(\gamma) = \frac{K_1}{4}\sin^2(2(\alpha-\gamma)) + K_U \sin^2(\alpha-\gamma) - HM_S\cos\gamma\ . \tag{2.20}$$

The rotation angle γ in Eq. (2.20) can be exchanged by $\cos\gamma =: m$ and consequently $\sin\gamma = \sqrt{1-m^2}$. For equilibrium condition $\partial E/\partial m = 0$, there is

$$\begin{aligned} H(m) =& \frac{K_1}{M_S}\left[(2m-4m^3)\cos 4\alpha + \frac{1-8m^2+8m^4}{2\sqrt{1-m^2}}\sin 4\alpha\right] \\ &-\frac{K_U}{M_S}\left[2m\cos(2(\alpha-\vartheta_U)) + \frac{1-2m^2}{\sqrt{1-m^2}}\sin(2(\alpha-\vartheta_U))\right]\ . \end{aligned} \tag{2.21}$$

This equation is solved for $H(m)$, since there is no analytical solution for $m(H)$, which is the standard form of the magnetization curves. Nevertheless, $m(H)$ can be determined numerically and thus, one can fit $m(H)$ to a set of experimentally determined magnetization curves with different azimuthal sample angles α for the curve parts of coherent rotation (monodomain state).

The scaled UMA constant K_U/M_S in Eq. (2.21) is small compared to the scaled CMA constant K_1/M_S. Therefore, K_U/M_S should not be treated as a fitting parameter, but kept constant using the determined values of the switching field fitting. The fit procedure delivers the CMA constant K_1/M_S.

2.2 Investigation of thin film magnetism via magnetooptic Kerr effect

The magnetooptic Kerr effect (MOKE) is a well examined physical phenomenon which can be utilized to investigate the magnetic character of matter. Especially, magnetic properties of thin films like magnetic anisotropies, the reversal process of the magnetization in the film and magnetic domain states can be obtained by this technique. Nevertheless, there are still some open theoretic questions as mentioned in this chapter.

One has to distinguish between a simple analysis of the hysteretic behavior of the film magnetism and a detailed reconstruction of the magnetization reversal process. Therefore, the basic physical theory of MOKE is presented in Chap. 2.2.1, while the theoretic part which consists of the distinction to the different components of the magnetization vector is summarized as vectorial magnetometry in Chap. 2.2.2.

Within the present thesis, the MOKE technique was extended using a combination of different vectorial magnetometry techniques. The developed theoretic background for this extension is summarized in this chapter and reported in detail in Chap. 6 which is also published in Ref. [20].

2.2.1 Magnetooptic Kerr effect

In order to introduce the MOKE, the principles and the origin of the effect are described in this chapter. The dependence of the MOKE on the reflection coefficients is presented as a basic connection for the confirmation of the relationship between MOKE and magnetization in the examined magnetic film, which is then discussed in the context of vectorial magnetometry in the next chapter.

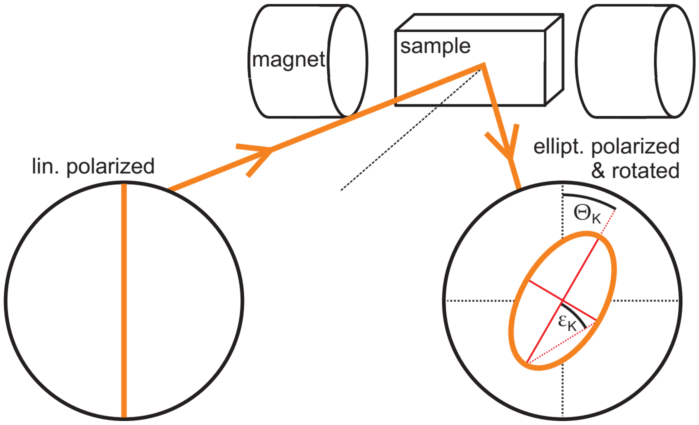

Figure 2.13: Principle description of MOKE. If linear polarized light is reflected by a magnetized sample, the polarization of the reflected light is rotated by the Kerr angle Θ_K and elliptic which is indicated by the Kerr ellipticity angle ϵ_K.

2.2.1.1 Principles of magnetooptic Kerr effect

The MOKE was named after the Scottish physicist John Kerr who firstly reported his discovery in 1877 [36]. He observed a change in polarization state when linear polarized light is reflected from a magnetized sample. In general, the polarization of the reflected light is elliptic and the major axis of the ellipse is rotated with respect to the direction of the polarization of the incident light as sketched in Fig. 2.13. Furthermore, MOKE can cause a change in intensity of the reflected light.

The rotation of the polarization is described by the Kerr angle Θ_K which is the angle between the direction of the linear polarization of the incident light and the major axis of the elliptic polarization of the reflected light (cf. Fig. 2.13). The change of polarization from linear to elliptic state is characterized by the Kerr ellipticity which depends on the ratio between the minor and the major axes of the ellipse. The Kerr ellipticity can be expressed by an angle ϵ_K which is marked in Fig. 2.13.

Both Kerr angle and Kerr ellipticity have a well defined dependence on the magnetization in the sample. In simplest case they are direct proportional to the magnetization of the illuminated part of the sample. But in most cases this relationship is more complicated and and can only be expressed by a superposition of different types of MOKE which are introduced in Chap. 2.2.2. In Fig. 2.14 the different physical values which define the Kerr angle and the Kerr ellipticity are pictured.

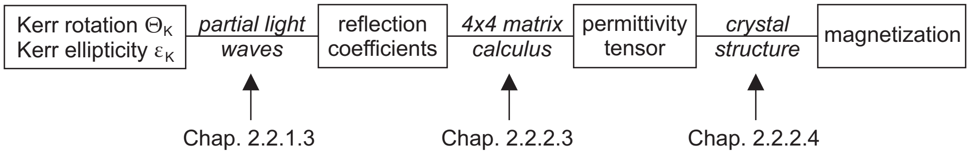

Figure 2.14: Relationship between MOKE and magnetization in the investigated film. The different connections between the physical values are labeled by the chapters in the present thesis where these connections are discussed.

The characteristic Kerr quantities depend on the change of properties of partial light waves which describe the incident light (Chap. 2.2.1.3). This change during reflection of light from the sample is expressed by the reflection coefficients which can be related to the permittivity tensor by the 4×4 matrix calculus (Chap. 2.2.2.3). Different crystal structures generate different permittivity tensors. Hence, the magnetization in a film with certain crystal structure defines the permittivity tensor and therefore, the relationship to the characteristic Kerr quantities (Chap. 2.2.2.4).

The information depth of the MOKE technique is restricted to the penetration depth of the incident light. In case of metallic films the penetration depth can be supposed to be at least 20 nm [37]. Therefore, the first 140 layers of an exemplary Fe film with layer distance of 1.43 Å are probed. Nevertheless, the influence of thicker films can also be examined indirectly, since the magnetization in the probed part of the sample is affected by the magnetism of the residual part of the film.

2.2.1.2 Origin of magnetooptic Kerr effect

Linear polarized light can be described by the superposition of two circular polarized light waves (right and left circular polarized). Therefore, the rotation of linear polarization is the consequence of a phase shift between the two circular polarized light waves. This phase shift is called circular birefringence and can be generated for example by different velocities for the right and left circular polarized light waves in a medium. If this effect is caused by a magnetic field, it is named magnetic circular birefringence. The well known manifestation of this effect is the Faraday effect [38], when linear polarized light propagates through a medium and the polarization rotates in dependence of the external magnetic field.

The change of polarization state from linear to elliptic can be explained by the change of the ratio of the amplitudes of the superposed circular polarized light waves. This so-called circular dichroism can be generated by different absorption coefficients for right and left circular polarized light in a medium. For example optic active molecules can change the polarization state by different absorption of right and left circular polarized light. If this effect is based on magnetism, it is called magnetic circular dichroism.

In most cases, the MOKE contains both magnetic circular birefringence (causing the Kerr rotation) and magnetic circular dichroism (generating the Kerr ellipticity). The preconditions for these effects in a magnetized sample are the spin-orbit coupling and the exchange interaction. The spin-orbit coupling describes the interaction between the spin of an electron and its angular momentum leading to a splitting of the electron energy levels. The exchange interaction between the electron spins is based on the Pauli principle and induces an energy gain for parallel and an energy loss for antiparallel spin alignment. If one of both effects either spin-orbit coupling or exchange interaction would be absent, no circular dichroism or birefringence would occur and therefore, no MOKE takes place as explained in the following using the example of circular dichroism.

In Fig. 2.15 electric dipole transitions of a magnetic material from d to p states are schematically presented. The transitions for spin up ($\uparrow$) and spin down ($\downarrow$) are shown on the left side. The resulting absorption spectra of left and right circular polarized light is presented on the right side. The notation $|lm\uparrow\rangle$ and $|lm\downarrow\rangle$ denotes the energy levels with l as orbital quantum number ($l = 1$ for p states, $l = 2$ for d states) and m as magnetic quantum number ($m = -l, ..., l$). The transition energy without exchange interaction and spin-orbit coupling is E_t. The exchange splitting of the d states shifts the energy levels for spin up and spin down by the exchange energy E_{ex}, while the spin-orbit coupling splits the energy levels by the coupling energy E_{so} in dependence on the alignment of the spin indicated by the magnetic quantum number m. The exchange splitting of the p states is neglected here.

The absorption spectrum for exchange interaction and spin-orbit coupling (Fig. 2.15(a)) demonstrates that the absorption is energetically shifted for left and right circular polarized light which is magnetic circular dichroism. The absorption spectrum for only spin-orbit coupling (Fig. 2.15(b)) and for only exchange interaction (Fig. 2.15(c)) have no complete separation of absorption energies for left and right circular polarized light. Hence, no magnetic circular dichroism and therefore, no birefringence occurs. In conclusion, both effects spin-orbit coupling as well as exchange interaction are necessary for the MOKE.

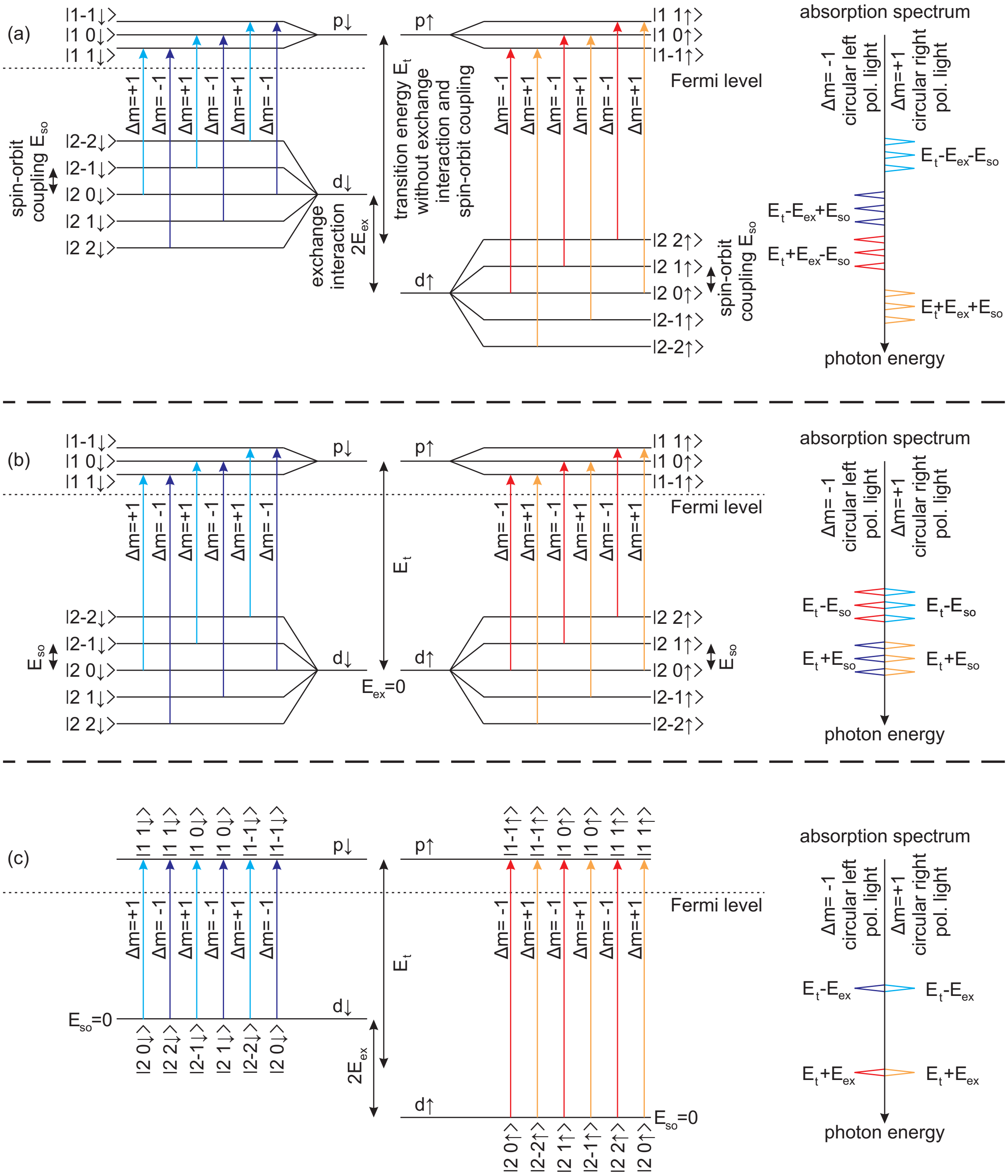

Figure 2.15: Schematic drawing of the absorption of left and right circular polarized light for the electric dipole transitions from d to p states indicated by arrows. On the right side the absorption spectra of left and right circular polarized light is presented (inspired by Ref. [39, 40]). (a) Absorption for both exchange interaction and spin-orbit coupling. (b) Absorption for only spin-orbit coupling. (c) Absorption for only exchange interaction.

2.2.1.3 Description of magnetooptic Kerr effect by reflection coefficients

Superposition of circular polarized light waves

If the linear polarization of the incident light is described by a superposition of right and left circular polarized light waves, the Kerr amplitude can be expressed by the complex reflection coefficients r_+ and r_- for left and right circular polarized light, respectively, as explained in the following.

Figure 2.16: (a) Linear polarization of the incident light (superscript i). (b) Elliptic and rotated polarization of the reflected light (superscript r). The polarizations $E^{i/r}$ with the polarization angle $\varphi^{i/r}$ are described by superposition of right and left circular polarized light waves ($E_-^{i/r}$ and $E_+^{i/r}$ with phase $\varphi_-^{i/r}$ and $\varphi_+^{i/r}$, respectively). Furthermore, the Kerr angle Θ_K and the Kerr ellipticity ϵ_K as well as the minor axis E_{min} and the major axis E_{max} of the ellipse are marked.

The polarization state of the incident and the reflected light is presented in Fig. 2.16. The Kerr angle Θ_K can be described by the difference of the polarization angle of the incident and the reflected light, φ^i and φ^r, respectively. The Kerr ellipticity angle ϵ_K depends on the ratio of the minor and major axis of the ellipse, E_{min} and E_{max}, respectively. This leads to

$$\Theta_K = \varphi^r - \varphi^i \quad \text{and} \tag{2.22}$$

$$\epsilon_K = \arctan\left(\frac{E_{min}}{E_{max}}\right) . \tag{2.23}$$

The description of the polarization states by circular polarized light waves can be performed by complex values with amplitude and phase. Therefore, right and left circular polarized light is defined as

$$E_- = |E_-|\, \mathrm{e}^{-i\varphi_-} \quad \text{and} \quad E_+ = |E_+|\, \mathrm{e}^{i\varphi_+} . \tag{2.24}$$

In Fig. 2.16(a) the incident linear polarization is described by the polarization angle φ^i which depends on the phases φ_-^i and φ_+^i of the circular polarized light waves. For linear polarization the amplitudes $\left|E_-^i\right|$ and $\left|E_+^i\right|$ of the superposed circular polarizations are the same. We conclude for incident light

$$\varphi^i = \frac{\varphi^i_+ - \varphi^i_-}{2} + 180^\circ \quad \text{and} \tag{2.25}$$

$$\left|E^i_+\right| = \left|E^i_-\right| \ . \tag{2.26}$$

The rotated and elliptic polarization of the reflected light is shown in Fig. 2.16(b). The polarization angle φ^r of the reflected light is given with respect to the direction of the major axis E_{max} of the ellipse. It can again be expressed by the phases φ^r_- and φ^r_+ of the circular polarized light waves. Here, the amplitudes $\left|E^r_-\right|$ and $\left|E^r_+\right|$ are different due to the circular dichroism which leads to the elliptic polarization with minor axis E_{min} and major axis E_{max}. We conclude for reflected light

$$\varphi^r = \frac{\varphi^r_+ - \varphi^r_-}{2} + 180^\circ \ , \tag{2.27}$$

$$E_{min} = \left|E^r_-\right| - \left|E^i_+\right| \quad \text{and} \quad E_{max} = \left|E^r_+\right| + \left|E^i_-\right| \ . \tag{2.28}$$

We want to express the Kerr rotation Θ_K dependent on the phase shifts between incident and reflected light waves $\Delta_- = \varphi^r_- - \varphi^i_-$ and $\Delta_+ = \varphi^r_+ - \varphi^i_+$ corresponding to left and right circular polarized light, respectively. After insertion of Eq. (2.25) and Eq. (2.27) into Eq. (2.22) we obtain

$$\Theta_K = \varphi^r - \varphi^i = \frac{\varphi^r_+ - \varphi^r_-}{2} - \frac{\varphi^i_+ - \varphi^i_-}{2} = \frac{\Delta_+ - \Delta_-}{2} \ . \tag{2.29}$$

The Kerr ellipticity angle ϵ_K can be described by the ratio of the amplitudes of the circular polarized light waves $|r_\pm| = \frac{\left|E^r_\pm\right|}{\left|E^i_\pm\right|}$ using Eqs. (2.23) and (2.28). Since the amplitudes of the circular polarized incident light waves are the same (cf. Eq. (2.26)) the result for small ϵ_K is

$$\epsilon_K = \frac{E_{min}}{E_{max}} = \frac{\left|E^r_-\right| - \left|E^r_+\right|}{\left|E^r_+\right| + \left|E^r_-\right|} = \frac{|r_-|\,\left|E^i_-\right| - |r_+|\,\left|E^i_+\right|}{|r_+|\,\left|E^i_+\right| + |r_-|\,\left|E^i_-\right|} = \frac{|r_-| - |r_+|}{|r_+| + |r_-|} \ . \tag{2.30}$$

For the mathematical description of the Kerr effect a complex Kerr amplitude $\Phi_K = \Theta_K - i\,\epsilon_K$ is defined [41, 42] with the Kerr angle Θ_K as the real part and the Kerr ellipticity angle ϵ_K as the imaginary part. Using Eqs. (2.29) and (2.30) the resulting Kerr amplitude for small Kerr effects is

$$\Phi_K = \Theta_K - i\,\epsilon_K = \frac{\Delta_+ - \Delta_-}{2} - i\,\frac{|r_-| - |r_+|}{|r_+| + |r_-|} = i\,\frac{r_+ - r_-}{r_+ + r_-} \tag{2.31}$$

as calculated in more detail in Ref. [18]. Here, $r_\pm = |r_\pm|\ \mathrm{e}^{i\,\Delta_\pm}$ are the reflection coefficients summarizing the phase shift $\Delta_\pm$ and the ratio of the amplitudes of the circular polarized light waves $|r_\pm|$. Beside these description of MOKE by reflection coefficients of circular polarized light waves, a second description is more common.

Superposition of linear polarized light waves

The polarization of light can also be described by superposed linear polarized light waves, which are parallel (p) and perpendicular (s) polarized with respect to the incidence plane of light. Therefore, the Kerr rotation and the Kerr ellipticity can be expressed by the elements of the reflection matrix $\hat{r}$ which is defined as

$$\hat{r} \;=\; \begin{pmatrix} r_{ss} & r_{sp} \\ r_{ps} & r_{pp} \end{pmatrix} . \tag{2.32}$$

This matrix is integrated in the Jones matrix calculus [43] describing the polarization of light by Jones vectors and optical components (including the reflection by a sample) by Jones matrices.

Figure 2.17: (a) Linear polarization of the incident light (superscript i). (b) Elliptic and rotated polarization of the reflected light (superscript r). The polarizations $E^{i/r}$ are described by superposition of s- and p-polarized light waves ($E_s^{i/r}$ and $E_p^{i/r}$, respectively). Furthermore, the Kerr angle Θ_K and the Kerr ellipticity ϵ_K are marked.

As sketched in Fig. 2.17 the polarization vectors of the incident and the reflected light, $\vec{E}^i$ and $\vec{E}^r$, respectively, are defined as

$$\vec{E}^i = \begin{pmatrix} E_s^i \\ E_p^i \end{pmatrix} \quad \text{and} \quad \vec{E}^r = \hat{r}\cdot\vec{E}^i = \begin{pmatrix} r_{ss}\,E_s^i + r_{sp}\,E_p^i \\ r_{ps}\,E_s^i + r_{pp}\,E_p^i \end{pmatrix} = \begin{pmatrix} E_s^r \\ E_p^r \end{pmatrix} \tag{2.33}$$

with E_s^i and E_p^i as the complex components of the incident polarization $\vec{E}^i$ for s- and p-polarized light, respectively. The components of the reflected polarization vector are expressed by using the superscript r instead of i. In Fig. 2.17(a) the example of s-polarized incident light is shown. Here, $\left|\vec{E}^i\right|$ equates the component E_s^i, since $E_p^i = 0$, for p-polarized incident light vice versa. Therefore, we obtain for the ratio of the components E_p^r and E_s^r in Eq. (2.33)

$$\frac{E_p^r}{E_s^r} = \frac{r_{ps}}{r_{ss}} \qquad \text{for incident linear s-polarized light and} \tag{2.34}$$

$$\frac{E_s^r}{E_p^r} = \frac{r_{sp}}{r_{pp}} \qquad \text{for incident linear p-polarized light.} \tag{2.35}$$

The elliptic and rotated polarization of the reflected light in Fig. 2.17(b) can further be described as an ellipse [44] with the Jones vector $E_0(\cos\epsilon, i\,\sin\epsilon)$ which is rotated by the matrix

$$\hat{R}(\alpha) \quad = \quad \begin{pmatrix} \cos\alpha & -\sin\alpha \\ \sin\alpha & \cos\alpha \end{pmatrix} \tag{2.36}$$

for any rotation angle α. For the polarization of the reflected light generated from incident s-polarized light we obtain

$$\vec{E}^r = \hat{R}(-\Theta_s)\cdot E_0 \begin{pmatrix} \cos\epsilon_s \\ i\,\sin\epsilon_s \end{pmatrix} = E_0 \begin{pmatrix} \cos\Theta_s\,\cos\epsilon_s + i\,\sin\Theta_s\,\sin\epsilon_s \\ -\sin\Theta_s\,\cos\epsilon_s + i\,\cos\Theta_s\,\sin\epsilon_s \end{pmatrix} \tag{2.37}$$

using the Kerr rotation Θ_s and the Kerr ellipticity angle ϵ_s generated from incident s-polarized light. The ratio of the components E^r_p and E^r_s in Eq. (2.37) for small Kerr effects yield

$$\frac{E^r_p}{E^r_s} = -\frac{\sin\Theta_s\,\cos\epsilon_s - i\,\cos\Theta_s\,\sin\epsilon_s}{\cos\Theta_s\,\cos\epsilon_s + i\,\sin\Theta_s\,\sin\epsilon_s} = -\frac{\tan\Theta_s - i\,\tan\epsilon_s}{1 + i\,\tan\Theta_s\,\tan\epsilon_s} \approx -\left(\Theta_s - i\,\epsilon_s\right)\ . \tag{2.38}$$

For incident p-polarized light the polarization of the reflected light is

$$\vec{E}^r = \hat{R}(-\Theta_p)\cdot\hat{R}(-90^\circ)\cdot E_0 \begin{pmatrix} \cos\epsilon_p \\ i\,\sin\epsilon_p \end{pmatrix} = E_0 \begin{pmatrix} -\sin\Theta_p\,\cos\epsilon_p + i\,\cos\Theta_p\,\sin\epsilon_p \\ -\cos\Theta_p\,\cos\epsilon_p - i\,\sin\Theta_p\,\sin\epsilon_p \end{pmatrix}. \tag{2.39}$$

The ratio between the components E^r_p and E^r_s in Eq. (2.39) can also be calculated for small Kerr effects, which leads to

$$\frac{E^r_s}{E^r_p} = \frac{\sin\Theta_p\,\cos\epsilon_p - i\,\cos\Theta_p\,\sin\epsilon_p}{\cos\Theta_p\,\cos\epsilon_p + i\,\sin\Theta_p\,\sin\epsilon_p} = \frac{\tan\Theta_p - i\,\tan\epsilon_p}{1 + i\,\tan\Theta_p\,\tan\epsilon_p} \approx \Theta_p - i\,\epsilon_p\ . \tag{2.40}$$

Comparison between Eq. (2.34) and Eq. (2.38) for s-polarized incident light as well as between Eq. (2.35) and Eq. (2.40) for p-polarized incident light results in

$$\Phi_s = \Theta_s - i\,\epsilon_s \approx -\frac{r_{ps}}{r_{ss}} \qquad \text{and} \qquad \Phi_p = \Theta_p - i\,\epsilon_p \approx \frac{r_{sp}}{r_{pp}} \tag{2.41}$$

with Φ_s and Φ_p as complex Kerr amplitude for s- and p-polarized incident light, respectively. This is the description of MOKE by elements of the reflection matrix.

2.2.2 Vectorial magnetometry

The orientation of the magnetization in the sample affects the way, how the Kerr rotation and the Kerr ellipticity are composed by different types of MOKE. These basic types as well as the phenomenon of second-order effects are explained in this chapter. Both linear and quadratic parts of MOKE influence the permittivity tensor, which varies for different crystal structures. The measured Kerr signals can be adequately scaled and processed in order to separate the course of the components of the magnetization. This processing is developed experimentally and theoretically in the present thesis and explained in this chapter for tetragonal and cubic crystal structures including second order effects and all possible directions of the magnetization vector.

2.2.2.1 Basic types and setup geometries of magnetooptic Kerr effect

The three different magnetization vector components of the sample have distinct contributions to the MOKE. Therefore, one distinguishes between three basic types of MOKE: longitudinal, polar and transversal. These basic types of MOKE which depend on the direction of the magnetization $\vec{M}$ should not be confused with the three different geometries of MOKE setups which depend on the direction of the external magnetic field $\vec{H}$. Here, one distinguishes also between longitudinal, polar and transversal setup geometry. For better understanding, the differences between the basic types and the setup geometries of MOKE are explained in the following.

Basic types of magnetooptic Kerr effect

The different basic types of MOKE are pictured in Fig. 2.18 and can be classified by the orientation of the magnetization $\vec{M}$ with respect to the incidence plane of light as well as to the sample surface. Here, the incidence plane of light is always perpendicular to the sample surface. It has to be emphasized that this classification of MOKE types is independent on the direction of the external magnetic field $\vec{H}$.

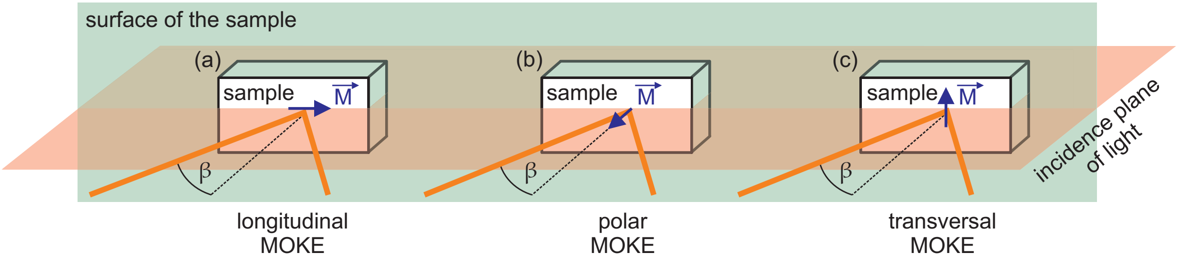

Figure 2.18: Basic types of MOKE dependent on the orientation of the magnetization $\vec{M}$ with respect to the incidence plane of light and to the sample surface. The incidence angle β is with respect to the surface normal. (a) LMOKE. (b) PMOKE. (c) TMOKE.

Longitudinal MOKE type

The longitudinal MOKE (LMOKE) occurs, if the magnetization $\vec{M}$ is aligned parallel to the plane of incidence of light and also parallel to the sample urface (cf. Fig. 2.18(a)). This in-plane magnetization generates a change in polarization (Kerr rotation and Kerr ellipticity), but no change of intensity. The LMOKE for s-polarized incident light has a different sign than for p-polarized incident light, i.e. the Kerr rotation and Kerr ellipticity have opposed rotation sense. The strength of LMOKE depends on the incidence angle β (with respect to the surface normal). The effect is weaker for smaller β and vanishes for $\beta = 0°$ (normal incidence).

Polar MOKE type

The polar MOKE (PMOKE) is generated by the out-of-plane magnetization component (perpendicular to the sample surface) as sketched in Fig. 2.18(b). Like the LMOKE, the PMOKE causes a change in polarization, but no change of intensity. However, there is no switching of sign between s- and p-polarized incident light. The strength of PMOKE is larger for smaller β

and reaches maximum for $\beta = 0°$. Furthermore, for normal incidence the strength of PMOKE is independent from the polarization state (s- or p-polarized incident light).

Transversal MOKE type

The transversal MOKE (TMOKE) occurs for magnetization $\vec{M}$ perpendicular to the incidence plane of light (cf. Fig. 2.18(b)). Therefore, it is in-plane aligned. In principle, no Kerr rotation or Kerr ellipticity is generated, but the intensity of p-polarized light is changed as explained below. Comparable to LMOKE the strength of TMOKE depends on β. For smaller β the effect is weaker and vanishes for $\beta = 0$. Since in this work only the change of polarization (Kerr rotation and Kerr ellipticity) is detected, we do not measure any TMOKE.

Setup geometries of magnetooptic Kerr effect

In contrast to the different basic types of MOKE one can distinguish between different setup geometries as shown in Fig. 2.19. The definition for longitudinal, polar and transversal setup is the same as for the basic types but with respect to the orientation of the external magnetic field $\vec{H}$ instead of the magnetization direction. For all setup geometries the magnetization $\vec{M}$ can be aligned in every possible direction, especially for small $\vec{H}$ the magnetization has not to be aligned parallel to the external field. Therefore, one can detect all three types of MOKE in all three setup geometries, e.g. one obtains both LMOKE and PMOKE as a superposition of Kerr rotation and Kerr ellipticity, if the magnetization has components in-plane and out-of-plane.

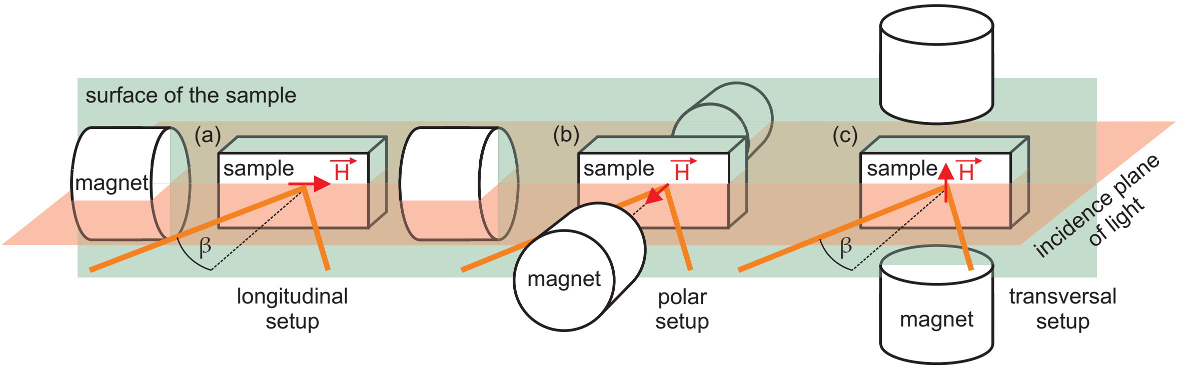

Figure 2.19: Setup geometries of MOKE dependent on the orientation of the external magnetic field $\vec{H}$ with respect to the incidence plane of light and to the sample surface. The incidence angle β is given with respect to the surface normal. (a) Longitudinal setup. (b) Polar setup. (c) Transversal setup.

If samples with preferred in-plane magnetization reversals are investigated, the longitudinal and the transversal setup geometries are used in order to saturate in-plane the sample magnetization. For samples with energetically favored out-of-plane direction the polar setup geometry is used, since the magnetization in these samples is very hard to saturate in-plane. In the present work the longitudinal and the transversal setup geometry is applied, because only samples with in-plane saturation magnetization are investigated.

Consequences for the detection of the different types of MOKE
The measured signal is a combination of the different MOKE types. One can write the reflection matrix $\hat{r}$ from Eq. (2.32) in dependence of LMOKE, PMOKE and TMOKE as

$$\hat{r} = \begin{pmatrix} r_{ss} & r_{sp}(\text{LMOKE, PMOKE}) \\ r_{ps}(\text{LMOKE, PMOKE}) & r_{pp}^{(0)} + r_{pp}^{(mag)}(\text{TMOKE}) \end{pmatrix} . \tag{2.42}$$

It has to be noted, that r_{ss} is independent from magnetization and that r_{pp} is composed by a constant term $r_{pp}^{(0)}$ and a term $r_{pp}^{(mag)}$ which depends on TMOKE. This is the reason, why TMOKE changes only the intensity of p-polarized incident light.

Comparison of Eq. (2.42) with the description of the complex Kerr amplitudes Φ_s and Φ_p (Eq. (2.41)) using reflection coefficients yields

$$\Phi_s = -\frac{r_{ps}(\text{LMOKE, PMOKE})}{r_{ss}} \quad \text{and} \quad \Phi_p = \frac{r_{sp}(\text{LMOKE, PMOKE})}{r_{pp}^{(0)} + r_{pp}^{(mag)}(\text{TMOKE})} . \tag{2.43}$$

Since the influence of $r_{pp}^{(mag)}$ to Eq. (2.43) is a contribution of the second order in off-diagonal elements, it is negligible compared with $r_{pp}^{(0)}$. Therefore, we can conclude that Φ_s and Φ_p are exclusively defined by LMOKE and PMOKE. The TMOKE has no appreciable contribution to the Kerr rotation and to the Kerr ellipticity. Thus, when measuring the change of polarization, we only detect contributions of the magnetization components parallel to the incidence plane of light (LMOKE, PMOKE) and we cannot detect the influence of the component perpendicular to the incidence plane of light (TMOKE). When measuring the change of intensity, it is the other way round.

2.2.2.2 Quadratic magnetooptic Kerr effect

In principle, MOKE is direct proportional to the magnetization of the sample as already mentioned in Chap. 2.2.1.1. However, in 1965 Metzger et al. [45] predicted that there could also be a dependence on higher order between Kerr effect and magnetization. The first reported experimental MOKE magnetization curve including second order effects was reported in 1990 by Zhong et al. [46] for Ni-Fe bilayers. This quadratic MOKE (QMOKE) contributes to the linear part in the magnetization curve and results in an asymmetric behavior. While QMOKE has an *even* course in magnetization the linear MOKE is *odd*.

In Fig. 2.20 a principle curve including linear MOKE and QMOKE is shown. The MOKE signal which demonstrates the experimental data is composed of a linear part which equates to the linear MOKE as well as a quadratic part which consists of the QMOKE and an offset due to experimental details. The experimentally determined MOKE curve can be separated into its odd and even part in order to obtain the linear MOKE and the quadratic part.

The symmetry of the magnetic reversal process can be described as $\vec{M}_{\text{inc}}(\vec{H}) = -\vec{M}_{\text{dec}}(-\vec{H})$ with $\vec{M}_{\text{inc}}$ as magnetization vector for increasing external field $\vec{H}$ and $\vec{M}_{\text{dec}}$ for decreasing external field. This symmetry is valid if exchange bias effects can be ruled out. Thus, symmetrization and antisymmetrization (odd and even part) of the measured Kerr rotation curve Θ result

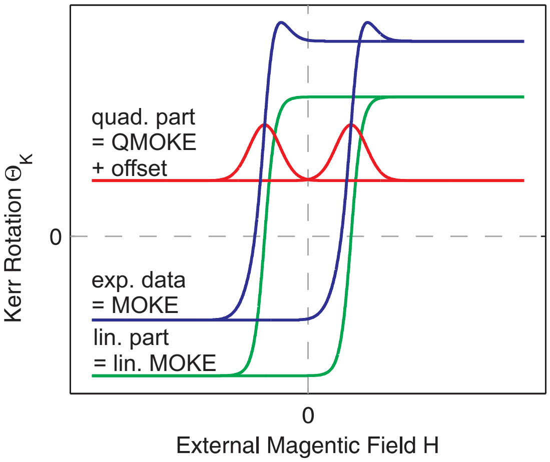

Figure 2.20: Principle curve (blue line) composed of a linear part (green line, linear MOKE) and a quadratic part (red line, QMOKE and experimental offset).

in the linear and quadratic part using [47]

$$\Theta_K^{\text{lin/quad}} = \left[\Theta_{\text{inc}}\left(\vec{H}\right) \mp \Theta_{\text{dec}}\left(-\vec{H}\right)\right]/2\ . \tag{2.44}$$

Here, Θ_{inc} and Θ_{dec} are the Kerr rotations for increasing and decreasing external magnetic field, respectively. The strength of QMOKE is larger for smaller incidence angles β and reaches its maximum for $\beta = 0°$ comparable to PMOKE. This behavior is opposed to the angular dependence of LMOKE and TMOKE.

QMOKE was reported for magnetic systems like Fe films on MgO [48], Mo/Al_2O_3 [49], Au/Fe/GaAs [50] and Ag/Au/GaAs/Ag [51]. Furthermore, the magnetization curves of Co films [49, 52] and Co-based Heusler alloys [47, 53, 54] are influenced by QMOKE. Although the origin of QMOKE is not completely understood up to now, it is supposed that the effect can mainly be traced back to spin-orbit coupling of second order [55, 56].

For vectorial magnetometry we only use the linear MOKE. Hence, the quadratic part of the magnetization curves has to be separated from the linear part, before further processing is performed. The exact composition of the linear MOKE and the QMOKE, i.e. which component of the magnetization vector contributes to the linear and to the quadratic part, respectively, is calculated in the next chapter.

2.2.2.3 Description of magnetooptic Kerr effect by permittivity tensor

Permittivity tensor

The interaction between light and matter can be described by the permittivity tensor $\hat{\epsilon}$. For isotropic media $\hat{\epsilon}$ has zero ranking and is a scalar. For anisotropic media $\hat{\epsilon}$ depends on the orientation of the sample and therefore it is a matrix (second-order ranked tensor). For a detailed definition of $\hat{\epsilon}$ we need a coordinate system in the laboratory frame of reference. This is x_1, x_2 and x_3 presented in Fig. 2.21.

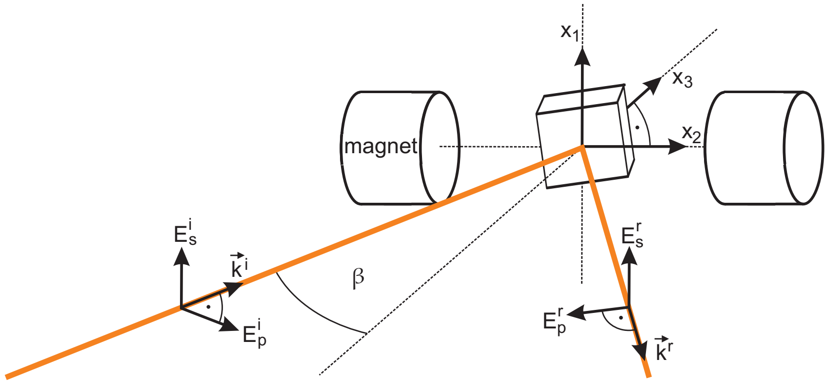

Figure 2.21: Definition of the coordinate system of the laboratory frame of reference x_1, x_2 and x_3. The polarization of incident (superscript i) and reflected light (superscript r) with wave vector $\vec{k}$ can be described by s- and p-polarized partial light waves (E_s and E_p, respectively). β denotes the incidence angle of light.

In this laboratory frame of reference x_1 is transversal aligned (in-plane and perpendicular to incidence plane of light), x_2 has longitudinal direction (in-plane and parallel to incidence plane of light) and x_3 is directed polar (out-of-plane) pointing away from the observer. Therefore, we can write the permittivity tensor relating to x_1, x_2 and x_3 as

$$\hat{\epsilon} = \begin{pmatrix} \epsilon_{11} & \epsilon_{12} & \epsilon_{13} \\ \epsilon_{21} & \epsilon_{22} & \epsilon_{23} \\ \epsilon_{31} & \epsilon_{32} & \epsilon_{33} \end{pmatrix} . \tag{2.45}$$

For a usual non-magnetic material the off-diagonal elements of $\hat{\epsilon}$ are zero. If the material is ferromagnetic, the off-diagonal elements are non-zero and generate a rotation of the polarization as explained in the following on the example of electric displacement.

Electric displacement

The permittivity tensor $\hat{\epsilon}$ defines the dependence of the electric displacement $\vec{D}$ on the electric field $\vec{E}$. If $\vec{E}$ is the electric field of the incident light, then $\vec{D}$ reveals the influence of $\hat{\epsilon}$ to the rotation of polarization of the incident light. In a first simple approach we want to calculate $\vec{D}$ for s- and p-polarized incident light using

$$\vec{D} = \epsilon_0 \, \hat{\epsilon} \, \vec{E} \tag{2.46}$$

with vacuum permittivity ϵ_0. In Fig. 2.21 it is shown, that the polarization of the incident light is described by the linear polarized light waves E_s^i and E_p^i as already introduced in Chap. 2.2.1.3. Now, we want to define this polarization in the laboratory frame of reference. Obviously, E_s^i is parallel to the x_1 direction and E_p^i is aligned in the $x_2 x_3$-plane. Therefore, one can write for s- and p-polarized incident light

$$\vec{E}_s = E_0 \begin{pmatrix} 1 \\ 0 \\ 0 \end{pmatrix} \quad \text{and} \quad \vec{E}_p = E_0 \begin{pmatrix} 0 \\ \cos(\beta) \\ \sin(\beta) \end{pmatrix} \text{, respectively.} \tag{2.47}$$

where E_0 is the initial amplitude of the electric field and β denotes the incidence angle. Hence, insertion of Eq. (2.45) and Eq. (2.47) into Eq. (2.46) yields

$$\vec{D}_s = \epsilon_0\, E_0 \begin{pmatrix} \epsilon_{11} \\ \epsilon_{21} \\ \epsilon_{31} \end{pmatrix} \quad \text{and} \quad \vec{D}_p = \epsilon_0\, E_0 \left(\cos(\beta) \begin{pmatrix} \epsilon_{12} \\ \epsilon_{22} \\ \epsilon_{32} \end{pmatrix} + \sin(\beta) \begin{pmatrix} \epsilon_{13} \\ \epsilon_{23} \\ \epsilon_{33} \end{pmatrix} \right) . \tag{2.48}$$

The electric displacement $\vec{D}_s$ for s-polarized incident light is only rotated compared with $\vec{E}_s$ when ϵ_{21} and/or ϵ_{31} are non-zero, so that $\vec{D}_s$ gains further components in x_2 and/or x_3 direction. For p-polarized incident light the electric displacement $\vec{D}_p$ is obviously rotated compared with $\vec{E}_p$ when ϵ_{12} and/or ϵ_{13} are non-zero, because then $\vec{D}_p$ gains an additional component in x_1 direction.

In conclusion, without non-zero off-diagonal elements in the permittivity tensor no rotation of polarization would occur. For s-polarized incident light the important off-diagonal elements for rotation are ϵ_{21} and ϵ_{31}, for p-polarized incident light the off-diagonal elements ϵ_{12} and ϵ_{13} are essential to generate a rotation.

4×4 matrix calculus

In order to calculate a mathematical relationship between the complex Kerr amplitude $\Phi_{s/p}$ and the permittivity tensor $\hat{\epsilon}$, we have to relate the reflection coefficients to the elements of the permittivity tensor. This is done using the 4×4 matrix calculus basically developed by Yeh [57] for anisotropic media. Here, the propagation of light through an anisotropic medium is described by four proper mode waves having proper polarizations by the layered medium. Proper polarization means that the light polarization does not change during propagation through a given medium. However, the intensity of a given mode can change due to absorption.

Each layer in the sample is described by a propagation matrix which consists of the information of propagation (dispersion, absorption) of the four proper mode waves. Furthermore at the interface, the tangential components of the electric and magnetic field are continuous. Hence, the interfaces of the layers are represented by so-called dynamic matrices which convert intensities of the proper modes into the tangential components of the electric and magnetic field.

Višňovský has extended this calculus to magnetic media [58] and described PMOKE [59] as well as LMOKE [60] by these 4×4 matrices. Also Zak et al. [61] used this formalism to derive analytical MOKE expressions in ferromagnetic multilayers. A complete calculation for a general permittivity tensor is reported by You and Shin [62]. In most cases the ultra thin ferromagnetic layer approximation is assumed which signifies that the film thickness of the ferromagnetic layer is much smaller than the wavelength of the probing light. For the reflection coefficients r_{ps} and r_{sp} one can obtain [63]

$$\begin{aligned} r_{ps} &= -\widetilde{N}\left(N_3\,\epsilon_{21} - \frac{N_3\,\epsilon_{23}\epsilon_{31}}{\epsilon_d} + \frac{N_2\,N^2\,\epsilon_{31}}{\epsilon_d}\right) \qquad \text{and} \\ r_{sp} &= \widetilde{N}\left(N_3\,\epsilon_{12} - \frac{N_3\,\epsilon_{32}\epsilon_{13}}{\epsilon_d} - \frac{N_2\,N^2\,\epsilon_{13}}{\epsilon_d}\right) \end{aligned} \tag{2.49}$$

with N_2 and N_3 as components of the normalized wave vector of light $\vec{k}/|\vec{k}| = (N_1, N_2, N_3)$. N_1 is zero, since the incidence plane of light is defined in the x_2x_3-plane (cf. Fig. 2.21). Furthermore, N is the complex refraction index for the non-magnetic surroundings like substrate (or capping layer) and ϵ_d describes the permittivity of zeroth order of the magnetic layer. The prefactor $\widetilde{N}$ depends on wavelength and incidence angle of light as well as the optical surroundings, but is independent on off-diagonal elements of the permittivity tensor.

As already mentioned in Chap. 2.2.2.1, the MOKE is assumed to have negligible influence to the diagonal reflection coefficients r_{ss} and r_{pp} concerning complex Kerr amplitude. Therefore, after insertion of Eq. (2.49) into Eq. (2.41) the complex Kerr amplitude for s- and p-polarized incident light can be written as

$$\begin{aligned} \Phi_s &= -\frac{r_{ps}}{r_{ss}} = A_s\left(\epsilon_{21} - \frac{\epsilon_{23}\epsilon_{31}}{\epsilon_d}\right) + B_s\epsilon_{31} \qquad \text{and} \\ \Phi_p &= \frac{r_{sp}}{r_{pp}} = -A_p\left(\epsilon_{12} - \frac{\epsilon_{32}\epsilon_{13}}{\epsilon_d}\right) + B_p\epsilon_{13} \end{aligned} \tag{2.50}$$

using the complex weighting coefficients

$$\begin{aligned} A_s &= \frac{\widetilde{N}\,N_3}{r_{ss}}\,, & B_s &= \frac{\widetilde{N}\,N_2\,N^2}{\epsilon_d\,r_{ss}}\,, \\ A_p &= -\frac{\widetilde{N}\,N_3}{r_{pp}} \quad \text{and} & B_p &= -\frac{\widetilde{N}\,N_2\,N^2}{\epsilon_d\,r_{pp}}\,. \end{aligned} \tag{2.51}$$

Eq. (2.50) shows which elements of the permittivity tensor give rise to the Kerr rotation. As already estimated by rotation of the electric displacement in Eq. (2.48), the elements of the permittivity tensor which are responsible in first order are ϵ_{21} and ϵ_{31} for s-polarized incident light as well as ϵ_{12} and ϵ_{13} for p-polarized incident light.

In conclusion, Eq. (2.50) is the resulting description of the complex Kerr amplitude for s- and p-polarized incident light by the off-diagonal elements of the permittivity tensor, which can be used to calculate the Kerr effect for a specific crystal structure.

2.2.2.4 Magnetooptic Kerr effect of tetragonal and cubic crystal structure

After the presentation how the complex Kerr amplitude is related to the off-diagonal elements of the permittivity tensor, we want to calculate the Kerr effect for a specific crystal structure.

In Ref. [47] the complex Kerr amplitude for cubic crystal structure was calculated including second order MOKE. Furthermore, the magnetization was restricted to in-plane reversal, i.e. no out-of-plane component was supposed.

In Chap. 6 of the present thesis and published in Ref. [20] the complex Kerr amplitude for tetragonal (and cubic) crystal structure was calculated including second order MOKE in combination of all common directions of the magnetization (in-plane and out-of-plane). Here, the theoretic explanations are summarized, since the detailed derivations are presented in Chap. 5.

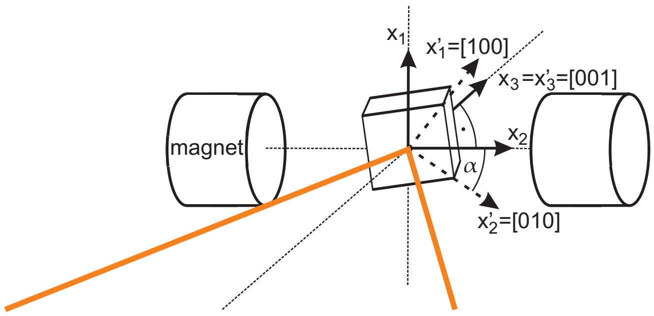

Figure 2.22: Definition of the coordinate system of the crystal frame of reference $x'_1 = [100]$, $x'_2 = [010]$ and $x'_3 = [001]$ with respect to the laboratory frame of reference x_1, x_2 and x_3. α denotes the azimuthal sample angle between x'_2 and x_2.

We introduce a second coordinate system in the crystal frame of reference which is defined as $x'_1 = [100]$, $x'_2 = [010]$ and $x'_3 = [001]$ (cf. Fig. 2.22). This coordinate system is independent from the position of the sample in the setup. Compared to the laboratory frame of reference introduced in Chap. 2.2.2.3 the out-of-plane directions x'_3 and x_3 are parallel pointing away from the observer. The azimuthal sample angle α describes the rotation of the sample with respect to the incidence plane of light and therefore, between x'_2-axis and x_2-axis.

The magnetization $\vec{M}$ can be expressed in both frames of reference. On the one hand, in the laboratory frame of reference $\vec{M}$ is described by the components M_1, M_2 and M_3 which are related to TMOKE, LMOKE and PMOKE (cf. Chap. 2.2.2.1). On the other hand, in the crystal frame of reference the components of $\vec{M}$ are parallel to the crystal axes and independent from the orientation of the sample in the setup.

Since the magnetization $\vec{M} = (M_1, M_2, M_3)$ affects the elements ϵ_{ij} of the permittivity tensor depending on the crystal structure, we want to evolute ϵ_{ij} with respect to the components of $\vec{M}$. Thus, the elements ϵ_{ij} of the permittivity tensor can be expressed as

$$\epsilon_{ij} = \epsilon_{ij}^{(0)} + K_{ijk}M_k + G_{ijkl}M_kM_l + \cdots \tag{2.52}$$

with constant elements $\epsilon_{ij}^{(0)}$ of the non-magnetic permittivity tensor $\hat{\epsilon}_{ij}^{(0)}$, the elements K_{ijk} of the linear magnetooptic tensor $\hat{K}$, the elements G_{ijkl} of the quadratic magnetooptic tensor $\hat{G}$ and the Einstein summation convention. The indices i, j, k can take the values of 1, 2 and 3 representing the three directions in space x_1, x_2 and x_3, respectively.

Taking into account the general symmetry arguments for $\hat{\epsilon}^{(0)}$, $\hat{K}$ and $\hat{G}$ [64] and for tetragonal crystal structure [20], we can express the permittivity tensor as a function of the magnetization $\vec{M}' = (M_1', M_2', M_3')$ in the crystal frame of reference. This is

$$\hat{\epsilon} = \begin{pmatrix} \begin{array}{c} G_{11}M_1'^2 + G_{12}M_2'^2 \\ +G_{13}M_3'^2 + \epsilon_d \end{array} & 2G_{66}M_1'M_2' + K_{12}M_3' & 2G_{44}M_3'M_1' - K_{31}M_2' \\ \\ 2G_{66}M_1'M_2' - K_{12}M_3' & \begin{array}{c} G_{12}M_1'^2 + G_{11}M_2'^2 \\ +G_{13}M_3'^2 + \epsilon_d \end{array} & 2G_{44}M_2'M_3' + K_{31}M_1' \\ \\ 2G_{44}M_3'M_1' + K_{31}M_2' & 2G_{44}M_2'M_3' - K_{31}M_1' & \begin{array}{c} G_{31}\left(M_1'^2 + M_2'^2\right) \\ +G_{33}M_3'^2 + \epsilon_{d_{33}} \end{array} \end{pmatrix} . \tag{2.53}$$

This tensor is valid for a non-rotated sample, i.e. azimuthal sample angle $\alpha = 0$. In order to obtain a general tensor for all azimuthal directions of the sample, one has to rotate the involved tensors $\hat{\epsilon}^{(0)}$, $\hat{K}$ and $\hat{G}$ [20]. The results show that $\hat{\epsilon}^{(0)}$ and $\hat{K}$ for tetragonal symmetry do not change after rotation. However, the quadratic magnetooptic tensor $\hat{G}$ changes.

Using Eq. (2.52) for the rotated tensors $\hat{\epsilon}^{(0)}$, $\hat{K}$ and $\hat{G}$ the results for the off-diagonal elements of the permittivity tensor in the laboratory frame of reference are

$$\begin{aligned} \epsilon_{12/21} =& \left[2G_{66} + \frac{\Delta G}{2}\left(1 - \cos\left(4\alpha\right)\right)\right] M_1M_2 - \frac{\Delta G}{4}\sin\left(4\alpha\right)\left(M_2^2 - M_1^2\right) \pm K_{12}M_3 \ , \\ \epsilon_{23/32} =& 2G_{44}M_2M_3 \pm K_{31}M_1 \quad \text{and} \\ \epsilon_{31/13} =& 2G_{44}M_3M_1 \pm K_{31}M_2 \end{aligned} \tag{2.54}$$

with $\Delta G = G_{11} - G_{12} - 2G_{66}$ as the magnetooptic anisotropy parameter. The diagonal elements are not important, since the complex Kerr amplitude depends only on the off-diagonal elements of the permittivity tensor (cf. Eq. (2.50)). Insertion of Eq. (2.54) into Eq. (2.50) yields the complex Kerr amplitude up to second order in magnetization which is

$$\begin{aligned} \Phi_{s/p} =& \pm A_{s/p}\left[2G_{66} + \frac{\Delta G}{2}\left(1 - \cos\left(4\alpha\right)\right) - \frac{K_{31}^2}{\epsilon_d}\right] M_1M_2 \\ & \mp A_{s/p}\frac{\Delta G}{4}\sin\left(4\alpha\right)\left(M_2^2 - M_1^2\right) + B_{s/p}G_{44}M_3M_1 \\ & \pm B_{s/p}K_{31}M_2 - A_{s/p}K_{12}M_3 \ . \end{aligned} \tag{2.55}$$

This expression of the complex Kerr amplitude contains linear terms proportional to M_2 and M_3 (corresponding to LMOKE and PMOKE, cf. Chap. 2.2.2.1) as well as second-order terms proportional to M_1M_2, $M_2^2 - M_1^2$, and M_3M_1.

In order to convert Eq. (2.55) into cubic crystal symmetry, Eq. (2.55) mainly remains the same, but one can use $K_{12} = K_{31}$, $G_{12} = G_{13} = G_{31}$ and $G_{44} = G_{66}$ [64] due to higher symmetry of cubic crystal compared to tetragonal crystal.

Eq. (2.55) shows that the initial statement in Chap. 2.2.1.1 (the Kerr effect is proportional to the magnetization) has to be observed in more detail. The pure proportionality between Kerr effect and magnetization is only valid if there is no QMOKE and one of the following conditions are fulfilled. Either the magnetization is strictly in-plane ($M_3 = 0$) or there is no magnetization component parallel to the external magnetic field ($M_2 = 0$) as proved by Eq. (2.55). For magnetization in all residual directions the pure proportionality is not given anymore due to the superposition of LMOKE and PMOKE. If QMOKE occurs, the measured Kerr signal is even more complex.

The description of the Kerr effect in Eq. (2.55) can be used to separate the components M_1, M_2 and M_3 of the magnetization from the measured signal as shown in the next chapter.

2.2.2.5 Determination of the separate components of the magnetization

Based on Eq. (2.55) the components of the magnetization vector can be separated by measurement of the Kerr effect for both s- and p-polarized incident light as well as the use of different external magnetic field directions. The development of this theoretical description concerning the experimental processing is also part of the present thesis and published in Ref. [20] (Chap. 6).

The linear and the quadratic part of the measured MOKE signal can be separated as explained in Chap. 2.2.2.2 by symmetrization and antisymmetrization of Eq. (2.55). The result is

$$\begin{aligned} \Phi_{s/p}^{\mathrm{quad}} &= \pm A_{s/p}\left[2G_{66} + \frac{\Delta G}{2}\left(1-\cos\left(4\alpha\right)\right) - \frac{K_{31}^2}{\epsilon_d}\right] M_1 M_2 \\ &\quad \mp A_{s/p}\frac{\Delta G}{4}\sin\left(4\alpha\right)\left(M_2^2 - M_1^2\right) + B_{s/p} G_{44} M_3 M_1 \qquad \text{and} \\ \Phi_{s/p}^{\mathrm{lin}} &= \pm B_{s/p} K_{31} M_2 - A_{s/p} K_{12} M_3 \ . \end{aligned} \tag{2.56}$$

The quadratic part $\Phi_{s/p}^{\mathrm{quad}}$ is not required for vectorial magnetometry. Thus, we focus on the linear part $\Phi_{s/p}^{\mathrm{lin}}$.

The weighting coefficients A_s and A_p (as well as B_s and B_p) depend on the angle of incidence β. For small β there is $A_s = A_p$ and $B_s = B_p$ and the course of M_3 and M_2 can easily be determined by the sum and the difference of $\Phi_{s/p}^{\mathrm{lin}}$ [65]. For larger β (as it is the case in this study) there is $A_s \neq A_p$ and $B_s \neq B_p$. Therefore, we need another processing to separate the components.

During our work we developed a scaling to separate the components even for larger β. For this propose the mean saturation value of s- and p-polarized signal is determined. During external magnetic saturation field $\Phi_{s/p}^{\mathrm{lin,sat}} = \pm B_{s/p} K_{31} M_2$ is valid since it is $M_3 = 0$ in magnetic saturation. Therefore, one can write the scaling factor $k_{s/p}$ as

$$k_{s/p} = \pm\frac{\Phi_s^{\mathrm{lin,sat}} - \Phi_p^{\mathrm{lin,sat}}}{2\Phi_{s/p}^{\mathrm{lin,sat}}} = \frac{B_s + B_p}{2B_{s/p}} \ . \tag{2.57}$$

The calculation of the sum and the difference of $\Phi_{s/p}^{\text{lin,scaled}}$ using Eqs. (2.56) and (2.57) yields

$$\begin{aligned}\Phi_+ &= -\frac{\Phi_s^{\text{lin,scaled}} + \Phi_p^{\text{lin,scaled}}}{2} = -\frac{k_s\Phi_s^{\text{lin}} + k_p\Phi_p^{\text{lin}}}{2} = \frac{B_s + B_p}{2} C K_{12} M_3 \quad \text{and} \\ \Phi_- &= \frac{\Phi_s^{\text{lin,scaled}} - \Phi_p^{\text{lin,scaled}}}{2} = \frac{k_s\Phi_s^{\text{lin}} - k_p\Phi_p^{\text{lin}}}{2} = \frac{B_s + B_p}{2} K_{31} M_2 \ . \end{aligned} \tag{2.58}$$

Here, $A_s/B_s = A_p/B_p =: C$ was used which is valid as provable by Eq. (2.51). The processing explained here results in two curves: Φ_+ proportional to M_3 and Φ_- proportional to M_2. Thus, the separation of magnetization components is fulfilled just by the right scaling.

For cubic crystal structure this processing is also valid, but one has to exchange K_{31} by K_{12} in Eq. (2.58) due to the higher symmetry compared to tetragonal crystal structure.

However, the processing is valid for complex description of Kerr effect. In the experiment we measure Kerr rotation which is the real part of the complex Kerr amplitude. Nevertheless, Eq. (2.58) can be used for separating the magnetization components M_2 and M_3. An error estimation can be found in Ref. [20].

In order to obtain the magnetization component M_1 the external magnetic field and the sample have to be rotated by 90°. Thus, the coordinate system in Fig. 2.21 also rotates. The x_1 direction is after rotation longitudinal instead of transversal and M_1 now causes the LMOKE. Therefore, the Kerr rotation is now generated by M_1 and M_3. The x_2 direction is now transversal and not longitudinal anymore. So, after rotation the M_2 component causes the TMOKE, which has only evanescent influence on the Kerr rotation as explained in Chap. 2.2.2.1. Hence, the Kerr rotation and therefore our measurements are now sensitive to the magnetization component perpendicular to the external field.

All equations in this chapter are now valid with M_2 exchanged by M_1 except the scaling, since the component perpendicular to the external field is not saturated during the reversal process. Hence, the scaling factor from external field parallel to the incidence plane of light is also used for the curves measured with perpendicular external field. Both components M_2 (measured with external field parallel to plane of incidence) and M_1 (obtained with external field perpendicular) have the same proportionality constant between Kerr rotation and magnetization because both are determined with the same Kerr effect, the LMOKE. The complete processing can also be done for this kind of setup to separate the linear part from the quadratic one as well as to separate the in-plane component from the out-of-plane component.

In conclusion, all components of the magnetization can be obtained in units of Kerr rotation. The complete reversal process can be reconstructed by calculating the magnitude and the direction of the magnetization vector from the determined magnetization components. Thus, conclusions concerning the domain states (monodomain and multidomain state) can be made as exemplarily performed in Ref. [20].

2.3 Investigation of thin film structure via x-ray radiation

In order to characterize thin films structurally they are examined by reflection and diffraction of x-rays. Therefore, x-ray reflectivity (XRR) and x-ray diffraction (XRD) are introduced in Chap. 2.3.1 and Chap. 2.3.2, respectively.

2.3.1 X-ray reflectivity

XRR measurements of thin films and multilayer systems reveal structural properties like layer thicknesses, refractive indices and interface roughnesses. The principles of this technique and exemplary reflectivity curves are presented in this chapter. Furthermore, the influence of surface roughness on the reflected reflectivity is discussed.

2.3.1.1 Principles of x-ray reflectivity

Incident light with wave vector $\vec{k}^i$ is reflected from an interface as pictured in Fig. 2.23. It has to be noted, that the incidence angle ϑ^i of the incoming light is defined with respect to the surface plane in contrast to the incidence angle in common optics where it is defined with respect to the surface normal. While the reflected part of the light with wave vector $\vec{k}^r$ propagates with the reflection angle $\vartheta^r = \vartheta^i$, the residual part (with wave vector $\vec{k}^t$) is refracted with the transmission angle ϑ^t.

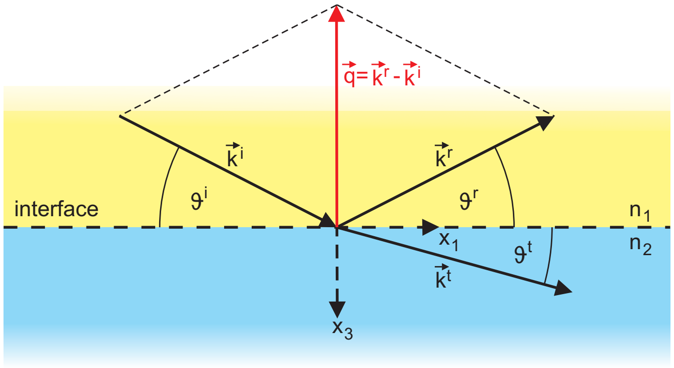

Figure 2.23: Reflection and transmission of an incident wave (wave vector $\vec{k}^i$ with incidence angle ϑ^i) at an interface between two optically different media with the refraction indices n_1 and n_2. One part of the incident wave is reflected (wave vector $\vec{k}^r$ with reflection angle $\vartheta^r = \vartheta^i$) and the residual part is refracted (wave vector $\vec{k}^t$ with transmission angle ϑ^t). The scattering vector $\vec{q} = \vec{k}^r - \vec{k}^i$ is varied during XRR measurements by changing the incident angle ϑ^i and keeping $\vartheta^r = \vartheta^i$. The x_1 axis is in-plane aligned parallel to the incidence plane and the x_3 axis is normal to the surface pointing into the sample.

Here, all wave vectors $\vec{k}$ are directed in the propagation direction of the respective light. The magnitude of $\vec{k}$ is defined as $|\vec{k}| = k = 2\pi/\lambda$ with the wavelength λ. Since $\vartheta^i = \vartheta^r$ and

$|\vec{k^i}| = |\vec{k^r}|$ due to energy conservation, the magnitude of the scattering vector $\vec{q} = \vec{k^r} - \vec{k^i}$ can be expressed as

$$q = 2\,k\,\sin(\vartheta^i) = \frac{4\,\pi}{\lambda}\,\sin(\vartheta^i)\ . \tag{2.59}$$

Hence, the scattering vector $\vec{q}$ is always normal to the surface and can be varied during XRR measurements by changing the incident angle ϑ^i and keeping $\vartheta^r = \vartheta^i$.

The transmission angle ϑ^t depends on the incidence angle ϑ^i and on the refraction indices n_1 and n_2 of the two optically different media. This relation can be expressed by the Snell's law

$$\frac{\cos(\vartheta^i)}{\cos(\vartheta^t)} = \frac{n_2}{n_1}\ . \tag{2.60}$$

In the classical image of harmonic oscillating atoms, the refractive index n for x-rays is given by [66]

$$n = 1 - \delta + i\,\beta \quad \text{with dispersion} \quad \delta = \frac{\lambda^2}{2\,\pi}\,r_e\,\rho \quad \text{and absorption} \quad \beta = \frac{\lambda}{4\,\pi}\,\mu\ . \tag{2.61}$$

Here, r_e is the classical electron radius, ρ the electron density and μ the absorption coefficient. Eq. (2.61) is valid for small incidence angles of light and x-ray photons with an energy far away from the absorption edges. A derivation in more detail can be found for example in Ref. [67].

Since the dispersion δ can only be positive (in the range of 10^{-6}), the real part of the refractive index n for x-rays is always slightly smaller than one. Thus, for x-ray reflection at an interface between air/vacuum ($n = 1$) and matter there is always total reflection at small incidence angles. No light is transmitted until the critical angle $\vartheta_c \approx \sqrt{2\,\delta}$ is reached. Above ϑ_c the reflected intensity is decreasing due to partially transmitted light.

If the reflected intensity I^r is scaled to the incident intensity I^i, it equates to the reflectivity $R = I^r/I^i = |r_{s/p}|^2$ with r_s and r_p as complex reflection coefficients for s- and p-polarized light, respectively. In the same way, the transmittivity $T = |t_{s/p}|^2$ is connected to the complex transmission coefficients $t_{s/p}$.

The tangential components of the electric and magnetic field of the light must be continuous at the surface. Thus, the reflection and transmission can be described by the Fresnel formulas. Since for x-rays s- and p-polarized light behaves in a similar way due to $n \approx 1$ for x-rays, the optical coefficients can be expressed as

$$r_{s/p} = \frac{k_3^i - k_3^t}{k_3^i + k_3^t} \quad \text{and} \quad t_{s/p} = \frac{2\,k_3^i}{k_3^i + k_3^t}\ \text{, respectively.} \tag{2.62}$$

Here, $k_3^i = k\,\sin(\vartheta^i)$ and $k_3^t = n\,k\,\sin(\vartheta^i) = k\,\sqrt{n^2 - \cos^2(\vartheta^i)}$ denote the x_3 component of $\vec{k^i}$ and $\vec{k^t}$, respectively. The x_3 axis is aligned normal to the surface as shown in Fig. 2.23, while the x_1 axis is directed in-plane parallel to the incidence plane.

The reflected intensity depending on the scattering vector q for a pure substrate is shown in Fig. 2.24(a). The inset shows the total reflection and the critical angle ϑ_c followed by the decrease of intensity proportional to q^{-4}.

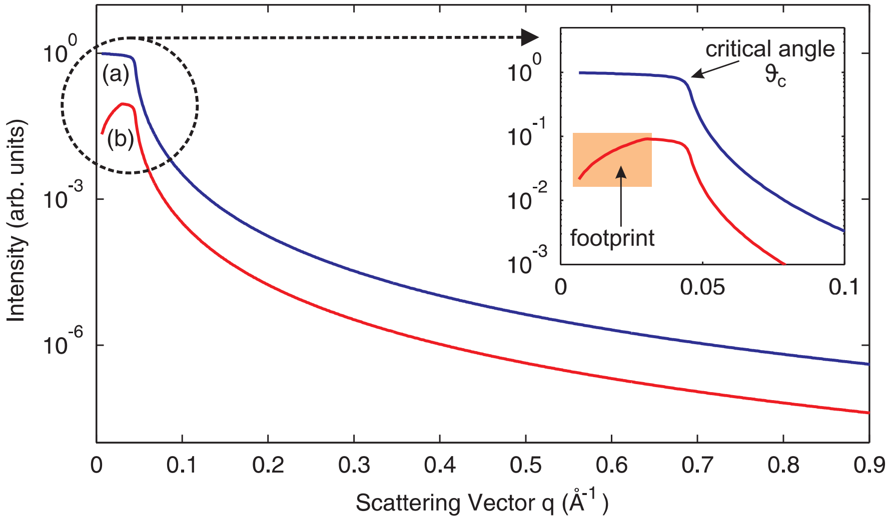

Figure 2.24: Reflectivity curves for the reflection at a surface (a) without footprint and (b) with footprint. The inset presents the curves (a) and (b) for small scattering vector q. The curves are shifted for clarity.

For small incidence angles the sample surface is only illuminated by a part of the x-ray beam due to spatial extension of the beam and finite size of the sample. By increasing the incidence angle this effect causes a linear increase of the intensity up to the point of complete illumination as presented in Fig. 2.24(b). This effect is called footprint.

2.3.1.2 Reflectivity of a multilayer system

For a multilayer system the reflected intensity is a more complicated expression. Part of the transmitted beam can be reflected at the next interface in the multilayer system and transmitted back at the first interface. Therefore, this part contributes to the part which is directly reflected at the topmost interface. In 1954 Parratt developed a recursive approach in order to calculate the total reflectivity of a multilayer system [68].

This algorithm for N layers can be described by the recursive expression of the reflectivity of the interface between the j-th and the $(j-1)$-th layer which is denoted by $R_{j-1,j}$. Using the Fresnel coefficient $r_{j-1,j}$ for the interface between the j-th and the $j-1$-th layer as well as the layer thickness D_j and the scattering vector q_j of the j-th layer, one can write [69]

$$R_{j-1,j} = \frac{r_{j-1,j} + R_{j,j+1}\,\mathrm{e}^{i\,D_j\,q_j}}{1 + r_{j-1,j}\,R_{j,j+1}\,\mathrm{e}^{i\,D_j\,q_j}} \qquad \text{for } j \in \{1, \dots, N\}\ . \tag{2.63}$$

Furthermore, the reflectivity of the lowest interface between the N-th layer and the substrate is denoted by $R_{N,N+1} = r_{N,N+1}$. By successive insertion of $R_{j-1,j}$ in Eq. (2.63) the reflectivity of the complete system is given by the reflectivity of the topmost interface $R = I^r/I^i = |R_{0,1}|$.

For a substrate and one layer of a specific thickness D the reflected intensity is pictured in Fig. 2.25(a). The oscillations are due to interference of the different contributions of the beam reflected at the surface and the part which is first transmitted and afterwards reflected at the interface. The thickness of the layer D can be obtained by determination of the distance between two oscillations Δq, since $D = 2\,\pi/\Delta q$.

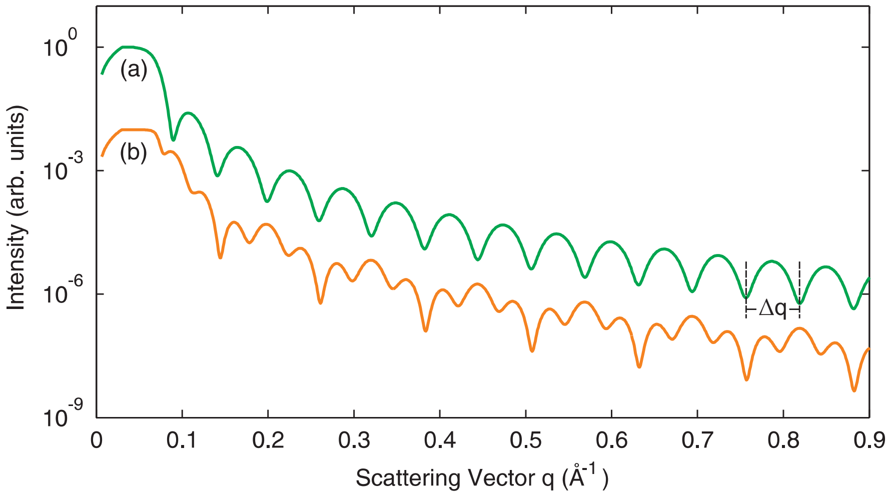

Figure 2.25: Reflectivity curves for the reflection at a substrate (a) with a thin layer and (b) with two thin layers of different thicknesses. The distance between two oscillations Δq reveals the thickness of the layer $D = 2\,\pi/\Delta q$. The curves are shifted for clarity.

For a multilayer system on a substrate the oscillations are more complicated as exemplarily shown in Fig. 2.25(b) for two thin layers of different thicknesses on a substrate. Therefore, the reflected intensity has to be simulated using an expected layer system. By fitting the modeled reflectivity to the experimental data the layer thickness, the dispersion and the absorption of each layer can be identified. In the present work, the in-house developed analysis tool *i*XRR was used for the fitting [67]. A further fitting parameter is the roughness of each interface which is introduced in the following.

2.3.1.3 Influence of interface roughness

Up to here, the reflectivity model has sharp interfaces with an abrupt change of the refraction index from one layer to the next. In nature, the interfaces are rough which leads to a more continuous change of the refractive index. This effect can be considered by a distributed height $x_{3,j}$ of the j-th layer.

Thus, the constant refractive index is replaced by a continuous distribution $n_j(x_1, x_2, x_3)$. Since the scattering vector $\vec{q}$ contributes only in x_3 direction (cf. Fig. 2.23), the refractive index can be laterally averaged depending on the x_3 direction. One obtains the refractive index

$$n_j(x_3) = \int\int n_j(x_1, x_2, x_3)\, dx_2\, dx_1\ . \tag{2.64}$$

We assume a Gaussian distribution

$$P_j(x_3) = \frac{1}{\sqrt{2\,\pi}\,\sigma_j}\, \mathrm{e}^{-\frac{x_3^2}{2\,\sigma_j^2}} \tag{2.65}$$

of the interface heights with standard deviation σ_j. Therefore, the continuous change of refractive index from the j-th layer to the $(j+1)$-th layer can be described by

$$n_j(x_3) = \frac{n_j + n_{j+1}}{2} - \frac{n_j - n_{j+1}}{2}\ \mathrm{erf}\left(\frac{x_3 - x_{3,j}}{\sqrt{2}\,\sigma_j}\right) \tag{2.66}$$

using the error function

$$\mathrm{erf}(x_3) = \frac{2}{\sqrt{\pi}} \int\limits_0^{x_3} \mathrm{e}^{-t^2}\, dt\ . \tag{2.67}$$

The continuous variation of the refractive index results in a modificated Fresnel coefficient

$$\tilde{r}_{j-1,j} = r_{j-1,j}\, \mathrm{e}^{-2\,k_{3,j-1}\,k_{3,j}\,\sigma_j^2}\ , \tag{2.68}$$

which has to be replaced in the recursive formula of Eq. (2.63). The exponential factor is called the Nevot-Crocet factor [70].

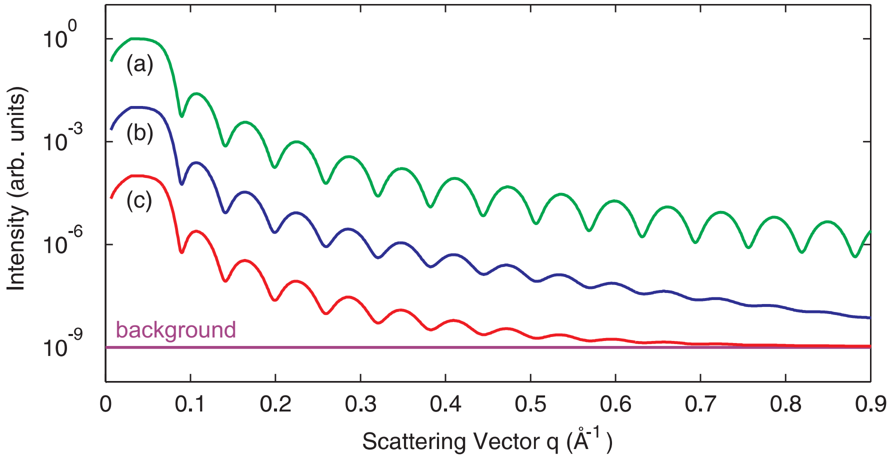

Figure 2.26: Reflectivity curves for the reflection at a substrate (a) with a thin layer, (b) considering the roughness of substrate and layer, (c) considering the roughness and the background. The curves are shifted for clarity.

The influence of the interface roughness is presented in Fig. 2.26 for the reflectivity of a substrate with a thin layer. Compared to the reflectivity of a sharp interface (Fig. 2.26(a)) the reflectivity of a rough interface (Fig. 2.26(b)) shows oscillations which are damped for larger scattering vectors q. Furthermore, a rough substrate interface amplifies the decrease of the reflected intensity for increasing q values.

The consideration of surface roughness is implemented in the analysis tool *i*XRR [67] as well as the insertion of an intensity background which is generated by diffuse background and by the flank of the first diffraction peak. This intensity background affects only the last part of the reflectivity curve with low intensity values due to the huge amount of intensity decades. An exemplary reflectivity curve including an intensity background is shown in Fig. 2.26(c).

2.3.2 X-ray diffraction

The structural parameters of a crystalline film like lattice constants and crystallite sizes can be obtained by XRD measurements. The principles of this technique are explained in this chapter. Additionally, specular diffraction and grazing incidence x-ray diffraction (GIXRD) is described. The latter technique is very sensitive to thin films compared to the substrate due to small incidence angles. For amorphous or polycrystalline films grazing incidence wide angle x-ray scattering (GIWAXS) was used which is also introduced in this chapter.

2.3.2.1 Principles of x-ray diffraction

X-rays are diffracted at the electrons of the atoms in matter. Therefore, periodically ordered atoms in crystalline structures lead to constructive interference of the diffracted light. These characteristic diffraction patterns can be correlated to the specific atomic lattices. In order to obtain such diffraction patterns the wavelength of the diffracted light must be in the range of the atomic layer distances which is of the order $10^{-10}\,\mathrm{m}$. Therefore, x-rays with a wavelength from $0.8\,\text{Å}$ to $1.24\,\text{Å}$ are used.

Bragg and Laue conditions

The principle of diffraction can be explained by the Bragg condition which relates to the atomic layer distance d, the wavelength λ and the incidence angle ϑ of the x-ray beam to determine constructive interference. Therefore, the path difference Δ for the reflection of light at two parallel lattice planes is shown in Fig. 2.27.

The path difference can expressed by

$$\Delta = \Delta_2 - \Delta_1 \quad \text{with the paths} \quad \Delta_1 = \Delta_2 \cos(2\,\vartheta) \quad \text{and} \quad \Delta_2 = \frac{d}{\sin\vartheta} \; . \tag{2.69}$$

For constructive interference the path difference has to equate to an integer multiple n of the wavelength λ. Using the trigonometric rule $1 - \cos(2\,\vartheta) = 2\,\sin^2\vartheta$ we obtain the Bragg condition

$$n\,\lambda = 2\,d \sin\vartheta \; . \tag{2.70}$$

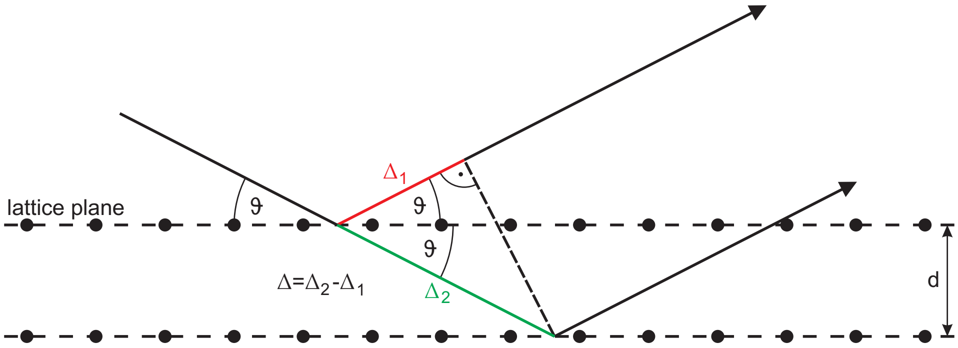

Figure 2.27: Determination of the path difference $\Delta = \Delta_2 - \Delta_1$ for the reflection at two parallel lattice planes. The incidence angle is ϑ and the atomic layer distance is d.

The Bragg condition is extended to three dimensions and leads to the Laue condition for elastic scattering

$$\vec{q} = \vec{G} \ , \tag{2.71}$$

which describes constructive interference, if the scattering vector $\vec{q}$ (cf. Chap. 2.3.1.1) corresponds to a reciprocal lattice vector $\vec{G}$. A reciprocal lattice is defined in the reciprocal space which is introduced in the following.

Reciprocal space

The reciprocal space describes the periodicity in real space. Thus, parallel lattice planes in real space corresponds to a point in the reciprocal space and its higher orders, for example. A lattice in real space with primitive lattice vectors $\vec{a}$, $\vec{b}$ and $\vec{c}$ can be converted into a reciprocal lattice with reciprocal primitive lattice vectors

$$\vec{a}^* = \frac{2\,\pi}{V_{UC}}\,(\vec{b}\times\vec{c}) \ , \quad \vec{b}^* = \frac{2\,\pi}{V_{UC}}\,(\vec{c}\times\vec{a}) \quad \text{and} \quad \vec{c}^* = \frac{2\,\pi}{V_{UC}}\,(\vec{a}\times\vec{b}) \ . \tag{2.72}$$

Here, $V_{UC} = \vec{a}\cdot(\vec{b}\times\vec{c})$ is the volume of the unit cell in real space.

Any reciprocal lattice vector $\vec{G}$ can now be expressed by a linear combination of $\vec{a}^*$, $\vec{b}^*$ and $\vec{c}^*$. This leads to another expression of the Laue condition in three dimensions

$$\vec{q}\cdot\vec{a} = 2\,\pi\,h \ , \quad \vec{q}\cdot\vec{b} = 2\,\pi\,k \quad \text{and} \quad \vec{q}\cdot\vec{c} = 2\,\pi\,l \ . \tag{2.73}$$

Here, h, k and l are integer values which means $\vec{q}$ is directed on a reciprocal lattice point. Thus, the Laue condition is fulfilled leading to constructive interference. The integers h, k and l are identical to the Miller indices already introduced in Chap. 2.1.1.2. At these reciprocal lattice points also the Bragg condition is fulfilled for the specific directions. Therefore, these points are called Bragg peaks.

As an example, a simple cubic lattice in real space with lattice constant a converts into a simple cubic lattice in reciprocal space with $a^* = 2\,\pi/a$. However, a bcc and an fcc lattice in real space convert into an fcc and a bcc lattice in reciprocal space, respectively, with $a^* = 4\pi/a$ in both cases. Generally, larger distances of periodic structure in real space yield smaller distances in reciprocal space and vice versa.

In Fig. 2.28(a) an exemplary reciprocal lattice of simple cubic bulk structure is shown. The coordinate axes are labeled by the reciprocal directions H, K and L. The Bragg peaks are placed on the integer positions $H = h$, $K = k$ and $L = l$ with $h, k, l \in \mathbb{N}$.

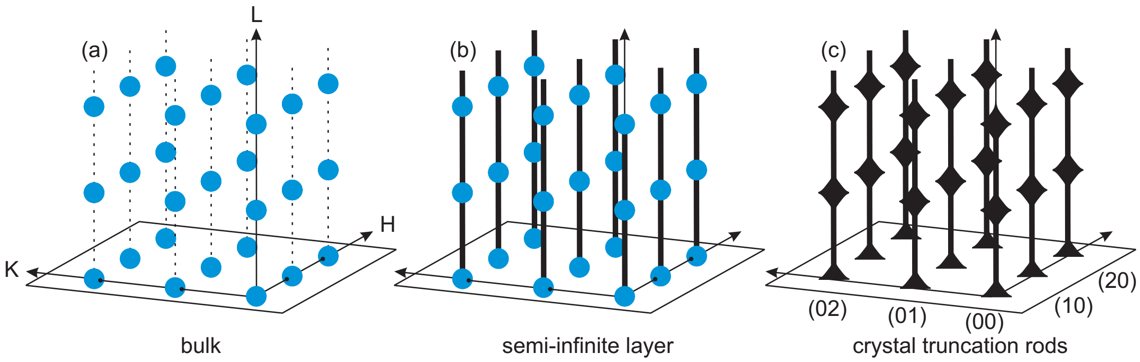

Figure 2.28: Reciprocal space of (a) bulk, (b) a semi-infinite layer and (c) a semi-infinite layer considering the limited penetration depth yielding the crystal truncation rods. These rods are labeled by (HK).

The crystalline sample can be treated as semi-infinite crystal lattices because of the symmetry break of the lattice at the surface. Above the surface no atomic layer contributes to the interference of the diffracted light. Thus, in reciprocal space the distance between the diffraction points in out-of-plane direction becomes infinitesimal and diffraction rods are formed. In Fig. 2.28(b) the reciprocal space including the diffraction rods of a thin film with simple cubic structure is sketched in comparison to the reciprocal space of a bulk sample (Fig. 2.28(a)).

Theoretically, the intensity of the Bragg peaks is infinite due to the semi-infinite crystal. But the incident x-rays have a limited penetration depth and therefore, the Bragg peak intensity is also limited. These peaks which have a Lorentzian shape and the diffraction rods form the crystal truncation rods, which are pictured in Fig. 2.28(c) and labeled by (HK).

Kinematic diffraction theory

In order to describe the diffracted intensity mathematically the kinematic diffraction theory is used. In a simplified model of the diffraction process the following assumptions are made.

1. Multiple scattering is neglected. It is assumed that each x-ray photon is scattered only once.
2. Absorption effects are not taken into account for thin films. Therefore, the different atomic layers are illuminated with the same intensity independent from their depth in the film. Furthermore, the energy of the x-ray light is far away from the absorption edges of the material.

3. Refraction is ignored. This assumption is only valid for incidence angles larger than the critical angle.

The amplitude $A(\vec{q})$ of the light which is diffracted at the electrons of the atoms depending on the scattering vector $\vec{q}$ is given by

$$A(\vec{q}) = A_0\, C\, F(\vec{q})\, G(\vec{q}) \tag{2.74}$$

with structure factor $F(\vec{q})$, lattice factor $G(\vec{q})$ as well as the constant prefactors A_0 (amplitude of incident light) and C containing different natural constants.

The structure factor $F(\vec{q})$ describes the contribution of a unit cell. It is the Fourier transformed atomic distribution of the unit cell and is expressed as

$$F(\vec{q}) = \sum_{j=1}^{N} f_j(q)\, \mathrm{e}^{i\,\vec{q}\cdot\vec{r}_j} \ . \tag{2.75}$$

The atomic form factor $f_j(q)$ corresponds to the Fourier transformed electron distribution of the j-th atom in the unit cell with N atoms. The position vector $\vec{r}_j$ defines the place of the j-th atom in the unit cell.

The lattice factor $G(\vec{q})$ depends on the primitive lattice vectors $\vec{a}$, $\vec{b}$ and $\vec{c}$ and is defined as

$$G(\vec{q}) = \sum_{n_1=0}^{N_1-1} \mathrm{e}^{i\,n_1\,\vec{q}\cdot\vec{a}} \sum_{n_2=0}^{N_2-1} \mathrm{e}^{i\,n_2\,\vec{q}\cdot\vec{b}} \sum_{n_3=0}^{N_3-1} \mathrm{e}^{i\,n_3\,\vec{q}\cdot\vec{c}} \ . \tag{2.76}$$

Here, the numbers of the unit cells in the spatial directions are N_1, N_2 and N_3. An exemplary detailed derivation of all relevant physical values can be found in Ref. [71].

One dimensional grating

In order to present an exemplary intensity distribution, a one dimensional periodicity is assumed. For the periodicity length a of N periodic structure elements we obtain the expression

$$S_{0,N}(q) = \sum_{n=0}^{N-1} \mathrm{e}^{i\,n\,q\,a} = \frac{1-\mathrm{e}^{i\,N\,q\,a}}{1-\mathrm{e}^{i\,q\,a}} \ . \tag{2.77}$$

By calculating the intensity $|S_{0,N}(q)|^2$ we determine

$$|S_{0,N}(q)|^2 = \frac{\sin^2(N\,q\,a/2)}{\sin^2(q\,a/2)} \ , \tag{2.78}$$

which is called N-slit function describing the diffracted intensity distribution of a one dimensional grating of N slits.

In Fig. 2.29 the diffracted intensity distribution for $N = 10$ is presented. The major Bragg peaks have a distance of $\Delta q = \frac{2\pi}{a}$ with minor maxima beside the major peaks. These oscillations (so-called fringes) have a distance of $\Delta q_0 = \frac{2\pi}{N\,a}$.

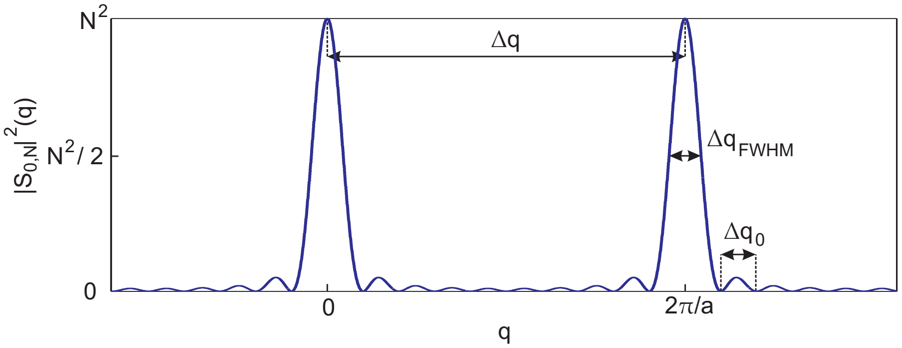

Figure 2.29: Diffracted intensity of a one dimensional grating with $N = 10$ slits. The Bragg peak distance $\Delta q = \frac{2\pi}{a}$ and the distance of oscillations $\Delta q_0 = \frac{2\pi}{N\,a}$ deliver the distance of the periodic elements in real space and the size of the grating, respectively.

From the distance of the Bragg peaks Δq one can obtain the distance of the periodic elements

$$a = \frac{2\,\pi}{\Delta q}\ . \tag{2.79}$$

The distance of the fringes Δq_0 yield the size of the grating $S = N\,a$ by the Scherrer formula

$$S = \frac{2\,\pi}{\Delta q_0}\ . \tag{2.80}$$

Therefore, from the diffraction pattern of a thin film the atomic layer distance can be obtained from the Bragg peak distance. The distance of the fringes gives the crystallite size. However, in some diffraction patterns the fringes can not be detected due to inhomogeneity of the film. In that case the Bragg peak distance can still be determined, but Δq_0 is not estimable. Therefore, the crystallite size is calculated by the full with of half maximum (FWHM) Δq_{FWHM} of the Bragg peak. The Scherrer formula has to be modified to

$$S = K_S\,\frac{2\,\pi}{\Delta q_{\mathrm{FWHM}}} \tag{2.81}$$

with the Scherrer factor $K_S = \frac{\Delta q_{\mathrm{FWHM}}}{\Delta q_0} = 0.89$. This factor is valid for all N-slit functions and can be numerically determined as exemplarily done in Ref. [72].

For a three dimensional lattice of a thin film the diffraction is more complicated because of the film morphology. Mosaics, facettes and vicinal surfaces can influence the position and the shape of the Bragg peaks.

Furthermore, the intensity of the Bragg peaks is affected by different correction factors (e.g. Debye-Waller factor, polarization factor, Lorentz factor, geometry factor) which are summarized in Ref. [73]. Since these correction factors have no effect on the position and on the FWHM of the Bragg peaks, they are not considered in the processing of the present work.

2.3.2.2 Specular diffraction

The most common x-ray diffraction technique is specular diffraction, which is presented in Fig. 2.30. Here, the incidence angle ϑ with respect to the lattice plane defines the scattering angle $\Theta = 2\,\vartheta$ and therefore, the magnitude of the scattering vector $\vec{q}$. Fig. 2.30(a) shows how the wave vectors $\vec{k^i}$ and $\vec{k^f}$ of incident and diffracted light are aligned for the specular diffraction. The scattering vector $\vec{q}$ has to hit a Bragg peak to fulfill the Laue condition and to determine constructive interference.

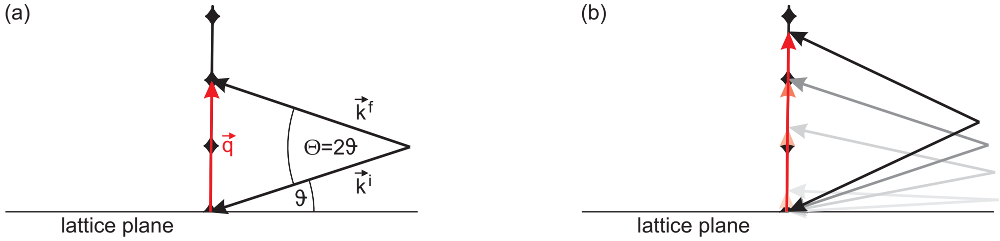

Figure 2.30: Sketch of the reciprocal space for specular diffraction. (a) The incidence angle ϑ defines the scattering angle $\Theta = 2\,\vartheta$ and the scattering vector $\vec{q}$. (b) Variation of the incidence angle leads to a change of the magnitude of the scattering vector.

Since $\Theta = 2\,\vartheta$ is always valid for specular diffraction, the scattering vector $\vec{q}$ is always normal to the lattice plane. The magnitude of $\vec{q}$ can be varied by change of ϑ as sketched in Fig. 2.30(b). This diffraction geometry is also called $\vartheta/2\vartheta$ geometry.

By specular diffraction one observes the intensity distribution of the (00) rod of the investigated film. Therefore, one can determine the vertical atomic lattice distance d of the film from the Bragg peak position and the vertical crystallite size S from the distance of the fringes (or alternatively from the FWHM of the Bragg peaks).

If the reciprocal space is scaled to the lattice of the substrate and expressed by H, K and L coordinates, the structural parameters can be calculated by

$$d = \frac{d_{sub}}{L_{peak}} \ . \tag{2.82}$$

with the vertical atomic lattice distance d_{sub} of the substrate and the Bragg peak position L_{peak} of the film.

The FWHM ΔL_{FWHM} gives the vertical crystallite size

$$S = K_S \,\frac{d_{sub}}{\Delta L_{\mathrm{FWHM}}} \ . \tag{2.83}$$

2.3.2.3 Grazing incidence x-ray diffraction

In order to observe the diffraction pattern of other rods than the (00) rod, grazing incidence x-ray diffraction (GIXRD) is performed. Here, the scattering angle Θ is independent from the incidence angle ϑ, since ϑ is kept constant. A small incidence angle is chosen, since the penetration path into the film for the x-rays is enhanced. Thus, the measured signal is relatively more affected by the contributions of the film compared to the substrate. However, the incidence angle should be larger than the critical angle to have no total reflection.

Fig. 2.31(a) shows the reciprocal space for the observation of the (02) rod. Since the incidence angle is fixed, one has to rotate the sample azimuthally while Θ is varied to hit different positions on the (02) rod. These Bragg peaks on higher diffraction rods yield vertical as well as lateral information of the film.

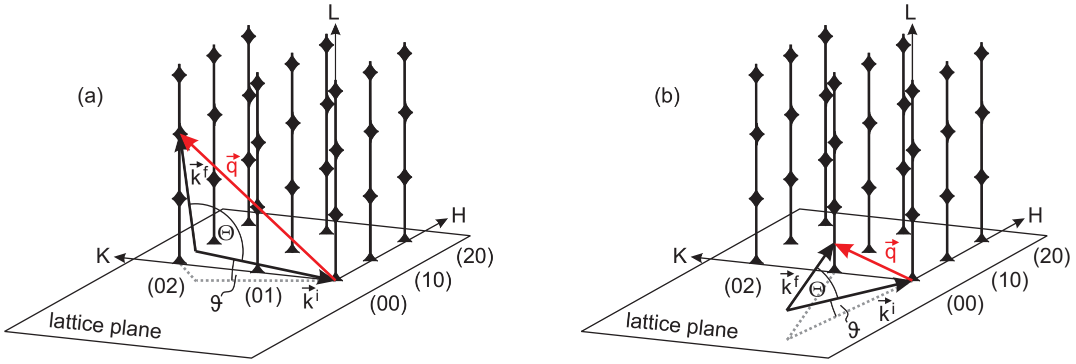

Figure 2.31: Sketch of the reciprocal space for GIXRD with small constant incidence angle ϑ and independent scattering angle Θ. (a) Observation of the (02) rod. (b) Lateral observation of the (01) rod near $L = 0$.

For the determination of lateral atomic lattice distances and lateral crystallite sizes the diffraction patterns for low L values have to be observed. Therefore, the wave vectors of incidence and diffracted light ($\vec{k^i}$ and $\vec{k^f}$, respectively) are nearly parallel in-plane aligned. The reciprocal space for this geometry is shown in Fig. 2.31(b). Since $\vartheta \neq 0$, the Bragg peaks with $L = 0$ values can not be completely reached. Thus, in-plane measurements show only the diffraction patterns of the in-plane Bragg peak flanks.

2.3.2.4 Grazing incidence wide angle x-ray scattering

For amorphous and polycrystalline films we use grazing incidence wide angle x-ray scattering (GIWAXS). As for GIXRD a small constant incidence angle ϑ is used to have a larger diffraction contribution of the film compared to the substrate.

Amorphous and polycrystalline films show no Bragg peaks, but broadened diffraction areas and large diffraction rings, respectively. Therefore, it is advantageous to observe a huge part of the reciprocal space at once using wide scattering angles Θ.

In Fig. 2.32 the reciprocal space for GIWAXS is pictured for a polycrystalline film. The observed part of the Ewald sphere (indicated by a straight line) shows polycrystalline diffraction rings due to the constructive interference for the intersections of Bragg sphere and Ewald sphere.

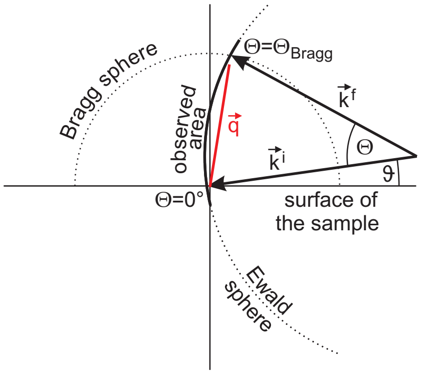

Figure 2.32: Sketch of the reciprocal space for GIWAXS with small constant incidence angle ϑ and wide scattering angle Θ. The observed area is the part of the Ewald sphere indicated by a straight line. Here, constructive interference can be observed for the intersections of Bragg sphere and Ewald sphere.

Since we observe polycrystalline rings and no Bragg peaks, the reciprocal lattice units H, K and L are not implemented here. Therefore, the conclusions to the distance of atomic lattice planes and to the crystallite sizes have to be drawn directly from the scattering angle Θ of the polycrystalline rings and from the magnitude of the scattering vector (cf. Eq. (2.59))

$$q = \frac{4\,\pi}{\lambda}\,\sin\left(\frac{\Theta}{2}\right)\ . \tag{2.84}$$

Since the distance of the atomic lattice planes is $d = \frac{2\,\pi}{q}$, one can write

$$d = \frac{\lambda}{2\,\sin\left(\frac{\Theta}{2}\right)}\ . \tag{2.85}$$

This equation is again the Bragg condition for $n = 1$ already presented in Eq. (2.70). Since for grazing incidence generally $\Theta \neq 2\,\vartheta$, Eq. (2.85) can not be expressed by using the incidence angle ϑ as in Eq. (2.70).

For determination of the crystallite sizes we use the derivation of Eq. (2.84)

$$\frac{dq}{d\Theta} = \frac{2\,\pi}{\lambda}\,\cos\left(\frac{\Theta}{2}\right) \qquad \Longrightarrow \Delta q_{\mathrm{FWHM}} = \frac{2\,\pi}{\lambda}\,\cos\left(\frac{\Theta}{2}\right)\,\Delta\Theta_{\mathrm{FWHM}}\ . \tag{2.86}$$

Insertion of Eq. (2.86) into the Scherrer formula (Eq. (2.81)) yield

$$S = K_S\,\frac{\lambda}{\cos\left(\frac{\Theta}{2}\right)\,\Delta\Theta_{\mathrm{FWHM}}}\ . \tag{2.87}$$

3 Investigated materials

In the present work different ferromagnetic material systems are analyzed. The investigations start with structures of single elements like amorphous and polycrystalline Co on glass and crystalline Fe on MgO. Furthermore, intermetallic structures like $Co_{50}Fe_{50}$ on MgO were examined. In the following all systems are described in detail.

3.1 Co on glass

The transition metal cobalt (Co) is ferromagnetic and has a Curie temperature of 1120°C. The common crystalline structures of Co up to a temperature of 400°C is hexagonal close-packed (hcp), which equates to a hexagonal lattice structure with a biatomic base (Fig. 3.1(a)). The lattice parameters of this so-called α-Co are $a_{\text{hcp-Co}} = 2.51\,\text{Å}$ and $c_{\text{hcp-Co}} = 4.07\,\text{Å}$.

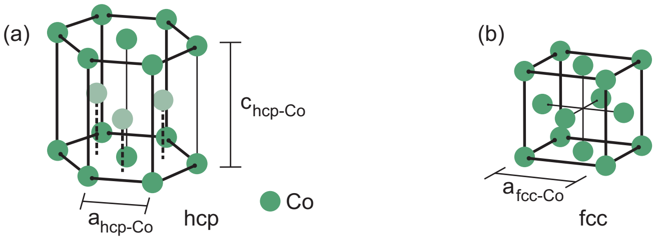

Figure 3.1: Crystalline structures of Co. (a) hcp structure with the lattice parameters $a_{\text{hcp-Co}} = 2.51\,\text{Å}$ and $c_{\text{hcp-Co}} = 4.07\,\text{Å}$. (b) fcc structure with the lattice parameter $a_{\text{fcc-Co}} = 3.55\,\text{Å}$.

For temperatures above 400°C Co forms a fcc structure (cubic close-packed) with the lattice parameter $a_{\text{fcc-Co}} = 3.55\,\text{Å}$ (Fig. 3.1(b)). This Co structure is named β-Co.

Glass consists mainly of SiO_2 and has an amorphous structure. If Co is deposited on glass, amorphous as well as polycrystalline Co films were assembled [74, 75]. The growth mode depends on the film thickness as shown in Ref. [76, 77]. Thinner films prefer to have amorphous structure while thicker ones are polycrystalline.

The Co films are capped by amorphous Si to avoid the oxidation of Co under ambient conditions. The Si capping layer has no influence on the MOKE measurements [78], since it is diamagnetic. Furthermore, part of the Si capping layer is oxidized due to the large reactivity of Si. Thus, the band gap of 1.1 eV for Si is increased to 9 eV for SiO_2 [79]. Hence, the used laser energy (He-Ne laser) of 2 eV has no influence on the Si capping layer. Therefore, the MOKE investigations are focussed on the magnetic Co film.

3.2 Fe on MgO(001)

Iron (Fe) is also a ferromagnetic transition metal and has a Curie temperature of 770°C. The favored crystalline structure of Fe at room temperature is bcc with the lattice parameter

$a_{\mathrm{Fe}} = 2.87\,\text{Å}$ (Fig. 3.2(a)). Further Fe structures like γ-Fe (fcc) and δ-Fe (bcc) can be grown above 900°C and 1400°C, respectively.

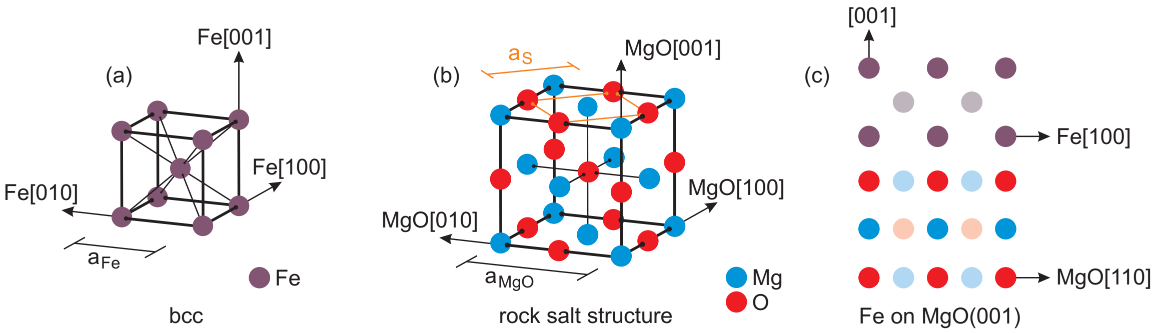

Figure 3.2: Crystalline growth of Fe on MgO. (a) bcc structure of Fe with lattice parameter $a_{\mathrm{Fe}} = 2.87\,\text{Å}$. (b) Rock salt structure of MgO with the lattice parameter $a_{\mathrm{MgO}} = 4.21\,\text{Å}$. The lattice parameter of the surface unit cell amounts to $a_{\mathrm{S}} = 2.98\,\text{Å}$. (c) Sideview of the growth with Fe(001)[100]||MgO(001)[110].

Magnesiumoxide (MgO), which is diamagnetic and insulating, is used as substrate. The crystalline structure of MgO is composed by Mg^{2+} and O^{2-} ions arranged in a rock salt structure (also known as NaCl lattice). This structure is equivalent to an fcc lattice with a biatomic base as presented in Fig. 3.2(b). The lattice parameter of the bulk lattice is $a_{\mathrm{MgO}} = 4.21\,\text{Å}$.

The surface unit cell on the MgO(001) surface is rotated by 45° with respect to the bulk surface unit cell. The surface lattice parameter is $a_{\mathrm{S}} = 2.98\,\text{Å}$ and fits well to the Fe lattice constant. The mismatch amounts to about 4%. Therefore, Fe grows on MgO(001) with Fe(001)[100]||MgO(001)[110] as shown in a sideview in Fig. 3.2(c) [80].

The Fe films grow in the Vollmer-Weber growth mode, since the surface tension of the Fe film is larger than the surface tension of MgO [80]. The Fe/MgO(001) samples are also capped by amorphous Si to avoid the oxidation of Fe under ambient conditions.

The cubic magnetocrystalline anisotropy of thin Fe films yields magnetic easy axes in Fe[100] and Fe[010] directions as well as magnetic hard axes in Fe[110] and Fe$[1\bar{1}0]$ directions [81].

3.3 $\mathrm{Co}_{50}\mathrm{Fe}_{50}$ on MgO(001)

$\mathrm{Co}_{50}\mathrm{Fe}_{50}$ films have a Curie temperature of about 1000°C and exhibit two different growth types. If the films are deposited at room temperature, they have bcc-like structure with randomly occupied sites of Co and Fe, the so-called A2-type. The position of both elements is statistically distributed as sketched in Fig. 3.3(a).

For annealing temperatures of 400°C after deposition the Co an Fe atoms form a ordered CsCl lattice named B2-type [82]. Here, the Co and Fe atoms alternately occupy the sites of the bcc lattice (Fig. 3.3(b)).

$\mathrm{Co}_{50}\mathrm{Fe}_{50}$ grows in the same way on MgO(001) as Fe. Thus, the $\mathrm{Co}_{50}\mathrm{Fe}_{50}$ unit cell is rotated

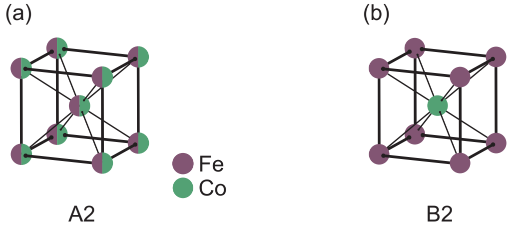

Figure 3.3: Crystalline structure of $Co_{50}Fe_{50}$. (a) bcc-like structure (A2-type) with randomly occupied sites by Co and Fe. (b) CsCl structure (B2-type) with ordered occupied sites by Co and Fe.

by 45° with respect to the MgO unit cell with $Co_{50}Fe_{50}$(001)[100]||MgO(001)[110] (cf. Ref [83]).

The investigated samples have a Cr/Au/Cr buffer layer between substrate and film to reduce stress. In order to avoid oxidation under ambient conditions, the films have a Au capping layer. The complete stacking is explained in more detail in Chap. 7 (Ref. [21]).

Thin $Co_{50}Fe_{50}$ films also have a cubic magnetocrystalline anisotropy, but in contrast to thin Fe films the magnetic easy axes are rotated in-plane by 45°. Therefore, the magnetic easy axes for thin $Co_{50}Fe_{50}$ films point in $Co_{50}Fe_{50}[110]$ and $Co_{50}Fe_{50}[1\bar{1}0]$ directions and the magnetic hard axes are aligned in $Co_{50}Fe_{50}[100]$ and $Co_{50}Fe_{50}[010]$ directions [83].

4 Experimental details

In this chapter the experimental details of the sample preparation are presented. Furthermore, the experimental setup for the magnetooptic Kerr effect technique is introduced. At last, the synchrotron beamlines and the diffractometer setups for the structural measurement techniques are described.

4.1 Sample preparation techniques

The investigated films in the present work are prepared by physical vapor deposition (PVD) under ultra high vacuum (UHV) conditions to avoid contamination of the prepared films. The Co on glass samples as well as the Fe films on MgO(001) are deposited by molecular beam epitaxy in Osnabrück. Furthermore, some Co on glass samples are prepared at the Freie Universität Berlin. The $Co_{50}Fe_{50}$ films on MgO(001) are fabricated by sputter deposition at the Tohoku University of Sendai, Japan. Both preparation techniques are described in the following.

4.1.1 Molecular beam epitaxy for Co on glass and Fe on MgO(001)

In order to prepare the investigated samples the according material is evaporated by direct or indirect heating. In the first case the evaporated material forms a massive rod (as e.g. for Fe or Co) and in the second case the material is put into a conduction crucible (as e.g. for Si). Both rod and crucible are set to positive high voltage (>1000 V) compared to a heat filament nearby as sketched in Fig. 4.1, so that they are heated up by electron bombardment. This bombardment is increased by the raise of the electron current until the material forms a

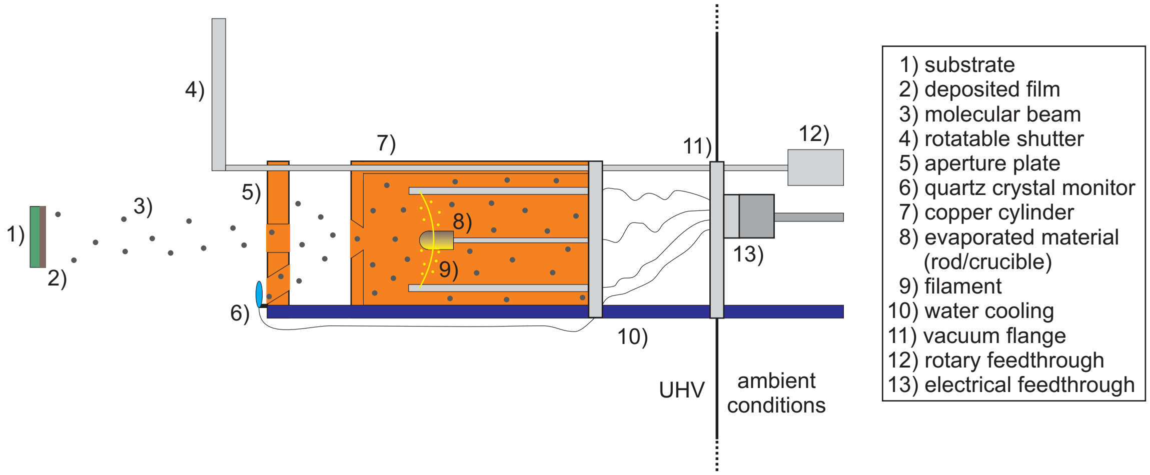

Figure 4.1: Principal drawing of a molecular beam evaporator. The rod/crucible is heated by electron bombardment and the material is evaporated towards the substrate. The coverage of the quartz monitor is an indication for the amount of deposited material on the substrate.

molecular beam which is directed onto the substrate.

Additionally, an oscillating quartz crystal monitor is mounted on the aperture plate in order to determine the amount of deposited material. Here, the variation of the oscillation frequency is proportional to the amount of material deposited on the quartz crystal. If the distance between rod/crucible, quartz crystal and substrate is constant, the variation of the oscillation frequency can be calibrated to the film thickness of the prepared samples (e.g. by XRR measurements).

Since the quartz crystal changes its oscillation frequency with a variation of the temperature, the thermal equilibrium should be reached before the deposition starts. Therefore, the copper cylinder and the aperture plate are cooled by water to avoid excessive heat. Furthermore, a rotatable shutter is used to avoid the deposition before the thermal equilibrium is reached. Furthermore, the shutter system allows to deposit for a defined time by quickly blocking the beam. The evaporation system is mounted on a vacuum flange with an electric feedthrough for the filament, the quartz and the rod/crucible as well as an rotary feedthrough for the shutter.

Co and Fe are deposited by a power between 25 W and 30 W (800°C-900°C), while Si needs a power between 90 W and 120 W (1200°C-1400°C) to be evaporated. Both substrates (glass and MgO) are heated up prior to the deposition in order to clean the surface and to anneal the crystal structure. The deposition is performed at room temperature. While the Co film preparation is done at a pressure of $p = 10^{-6}\,\mathrm{mbar}$ (base pressure at $p = 10^{-7}\,\mathrm{mbar}$) using a deposition rate of 0.3 nm/min, the Fe films are prepared at $p = 10^{-7}\,\mathrm{mbar}$ (base pressure at $p = 10^{-8}\,\mathrm{mbar}$) using a deposition rate of 1 nm/min.

Thicker Co films (>50 nm thickness) are assembled in the group of Prof. Fumagalli at the Freie Universität Berlin using a commercial electron beam evaporator. Here, the Co is heated up by an electron beam which is directed onto the evaporated material by a magnetic field. The base pressure during deposition is $p = 10^{-9}\,\mathrm{mbar}$ using a deposition rate of 12 nm/min.

More details to the preparation procedure are summarized for the Co on glass samples in Chap. 5 (Ref. [19]) and for the Fe films on MgO in Chap. 6 (Ref. [20]).

4.1.2 Sputter deposition for $Co_{50}Fe_{50}$ films on MgO(001)

Sputter deposition is performed by ion bombardment of a target which consists of the evaporated material. Here, a plasma is produced in the UHV chamber and the ions are accelerated by negative high voltage towards the target (Fig. 4.2).

When the plasma ions hit the target, atoms are sputtered out by a cascade of collisions in the target material. Beside the atoms, also some ions of the target material are sputtered out. The plasma should consist of inert ions to avoid reactions with the target atoms. Therefore, the amount of ions which are sputtered out is negligible. Hence, often a noble gas like Ar is used for the plasma. The target atoms reach the substrate and condensate on the substrate surface.

The $Co_{50}Fe_{50}$ films are prepared by sputter deposition in the group of Prof. Takanashi at the Tohoku University of Sendai, Japan. The films are deposited at a base pressure less than

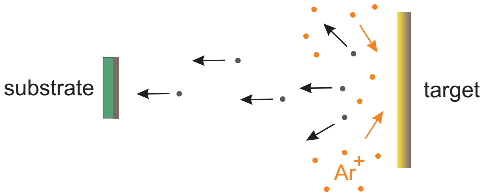

Figure 4.2: Principal drawing of sputter deposition. The target is penetrated by ions. Atoms are sputtered out and reach the substrate.

10^{-9} mbar on MgO(001) with a Cr/Au/Cr buffer stack in between and a Au capping layer as already mentioned in Chap. 3.3. After deposition of $Co_{50}Fe_{50}$ the films are annealed at different temperatures from RT up to 400° as explained in detail in Chap. 7 (Ref. [21]).

4.2 Determination of magnetic properties

The MOKE setup in the group of Prof. Wollschläger was built up in 2007 as the diploma thesis of the present author. In Ref. [18] the initial setup is introduced. During the present work the MOKE was improved to perform vectorial magnetometry by the use of different incidence polarizations and variation of the external magnetic field among other improvements. The current setup and the actual measurement procedure are described in this chapter. Furthermore, the proportionality between the measured signal and the Kerr rotation is proved.

4.2.1 Principle MOKE setup

The current MOKE setup consists of four elements: the optical branch of the incident light, the optical branch of the reflected light, the sample holder and adjustment unit as well as the external magnet. The complete setup is shown in Fig. 4.3 and explained in the following.

Optical branch of the incident light

The used light source is a He-Ne laser with a wavelength of $\lambda = 632.8\,\text{nm}$ and an output power of 5 mW. The diameter of the laser beam is about 1 mm, which guarantees that a huge amount of magnetic domains in the sample are probed. The linear polarization of the light is generated by a polarizer at 0° for p-polarized light and at 90° for s-polarized light.

Since the laser light is already slightly polarized when leaving the light source, the intensity of light can be controlled by insertion of a $\lambda/2$ plate between light source and polarizer. The $\lambda/2$ plate rotates the polarization. Therefore, the projection of polarization to the direction of the polarizer varies. Thus, the intensity of light behind the polarizer changes, but the polarization direction is kept constant.

The incidence angle of light is 45°. Hence, the reflectivity of s- and p-polarized light differs. As introduced in Chap. 2.2.2.5 and detailed explained in Chap. 6 (Ref. [20]) we developed a scaling of the magnetization curves in order to obtain all magnetization components independent

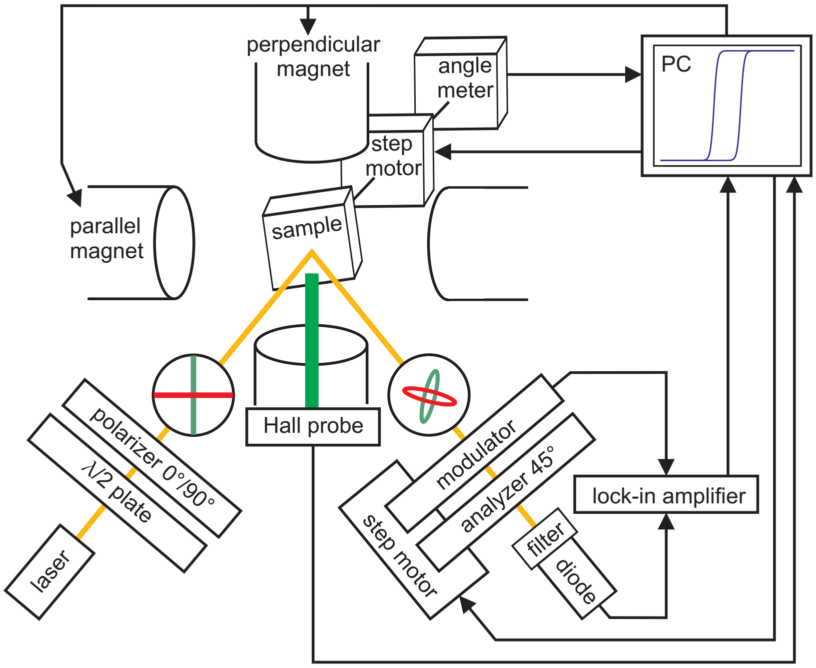

Figure 4.3: MOKE setup for s- and p-polarized incident light and external magnetic field parallel and perpendicular to the incidence plane.

from the incidence angle and therefore, independent from the different reflectivity of s- and p-polarized light.

Optical branch of the reflected light

The reflected light is modulated by a photoelastic modulator (PEM) which consists of a quartz with the modulation axis parallel to the incidence plane of light. AC voltage is applied to obtain an oscillating refractive index in the quartz due to the photoelastic effect. The quartz is stretched and shrunk by the piezoelectric effect because of the AC voltage. Therefore, the electron density is also oscillating which leads to a variation of the refractive index.

Since this oscillating refractive index only affect the p-polarized part of the reflected light while the s-polarized part has constant refractive index, the quartz becomes birefringent. Thus, the polarization generated by the PEM is oscillating as well. This periodic variation includes the direction of the polarization as well as the ellipticity.

The analyzer behind the PEM (polarizer at 45°) converts the polarization signal into an intensity signal due to the polarization projection to the direction of the analyzer. The intensity signal is detected by a Si photo diode. In order to reduce noise and to avoid the detection of other light sources, an interference filter is placed on the diode. Hence, only light with a wavelength of $\lambda \approx 632.8\,\mathrm{nm}$ can pass by and hit the diode.

The detected oscillating signal is composed of signal contributions corresponding to different frequencies which are integer multiples of the modulation frequency Ω of the AC voltage applied on the PEM. The contributions corresponding to once and twice the modulation frequency are proportional to the Kerr ellipticity and Kerr rotation, respectively, as proved in Chap. 4.2.3. These contributions are called Ω signal and $2\,\Omega$ signal. In most cases, the modulation frequency amounts to $\Omega = 50\,\mathrm{kHz}$ for the present setup. Some measurements are done with a different PEM having a modulation frequency of $\Omega = 42\,\mathrm{kHz}$.

Both modulation frequency and measured signal are given to a lock-in amplifier which separates the contributions of different frequencies. Thus, all unwanted signal contributions (including noise) are filtered out. The retardation of the PEM which is the amplitude of the oscillating effect can be varied. Since the retardation contributes with a Bessel function (Chap. 4.2.3), the retardation concerning the maximum of the Bessel function is chosen to obtain the maximum signal [55, 84].

The alignment of the PEM with respect to the polarization direction of the reflected light affects the signal to noise ratio. As shown in Ref. [72] the signal-to-noise ratio is maximized for zero modulation. Thus, the change of intensity signal is maximal for small changes of the reflected polarization, which then induce a modulation. The point of vanishing modulation can be reached by a small tilt of the PEM around the direction of the reflected beam until the polarization direction of the reflected light is either parallel or perpendicular to the modulation axis of the PEM depending on the incidence polarization.

In the present thesis, the Kerr rotation is observed, not the Kerr ellipticity. Therefore, the lock-in amplifier is adjust to separate the $2\,\Omega$ signal. Observation of the Kerr rotation has the advantage to calibrate the measured signal as described in Chap. 4.2.2 using a step motor which rotates the PEM an the analyzer simultaneously. The calibration of the Kerr ellipticity would need more optical alignment (e.g. $\lambda/4$ plate), because it can not be directly calibrated.

Sample holder and adjustment unit

The sample is mounted on a sample holder which can be automatically rotated by a step motor. The sample holder can be tilted in order to adjust the sample surface perpendicular to the rotation axis of the holder and to the incidence plane of light. The complete holder system is mounted on a three dimensional xyz-translation table. Thus, the position of the sample between the magnetic poles can be varied. This also changes the position of the illuminated area on the sample.

Additionally, the sample holder is connected to an angle meter which gives the exact angle of the holder with an accuracy of at least $\pm 0.01°$. It has to be noticed, that the step width of the step motor is $0.005°$, which is due to the fact that 72000 steps are needed for a full rotation of $360°$. However, the absolute accuracy of the step motor varies sinusoidal $\pm 0.2°$ depending on the absolute position [72]. A feedback loop between step motor and angle meter is implemented to reach the accuracy of the angle meter. Thus, the sample can be aligned very precisely concerning the position in the setup and also concerning the azimuthal sample angle.

The external magnet

The external magnet consists of two water cooled coils. The magnetic poles can be shifted to vary the pole distance. For most measurements a pole distance of 5-8 cm is used. The maximum current of 10 A (at maximal 50 V) gives a maximum magnetic field of $\mu_0 H \approx 100 - 150\,\mathrm{mT}$. A detailed characterization of the used magnet including induction curves for different pole distances and the examination of the homogeneity of the magnetic field between the poles can be found in Ref. [18].

For measurements with perpendicular external magnetic field the magnet is rotated by 90°. Thus, the second in-plane magnetization component can be determined. In both magnet geometries the magnet field is detected by a Hall probe.

All measurement signals which are magnetic field, intensity at the diode and angle of the sample observed by the angle meter are collected by a computer. The current of the magnet and all step motors are also controlled by the computer during the experiment.

4.2.2 Measurement procedure including calibration of Kerr rotation

After the sample is mounted on the holder, the sample surface is adjusted perpendicular to the rotation axis of the sample holder and therefore, perpendicular to the incidence plane of light. This is performed by insertion of a mirror in front of the diode. The position of the reflected light at the wall is more sensitive to a tilt of the sample surface due to the long path of light. Now, the sample surface is tilted until the laser spot on the wall does not move anymore, if the sample is azimuthally rotated.

After adjustment of the incidence intensity and polarization, the PEM is tilted to optimize the signal-to-noise ratio as described above. Therefore, the light reaching the diode is observed by a oscilloscope to find the point of vanishing modulation. Subsequently, the measured lock-in signal is calibrated to the Kerr rotation under maximum external field to keep the magnetization constant during the calibration.

For the calibration the PEM and the analyzer are rotated simultaneously by a step motor keeping the polarization direction of the reflected light constant. The rotation angle is 0.2°. This rotation changes the angle between PEM and polarization direction of reflected light as well. The variation is the same as if the alignment of PEM is kept constant and the polarization of reflected light would be rotated by the Kerr rotation of 0.2°. In both cases, the $2\,\Omega$ signal from the lock-in amplifier varies relatively in the same way. Thus, the intensity difference of the $2\,\Omega$ signal before and after rotation corresponds to 0.2° Kerr rotation. The calibration factor for each sample is calculated equivalently. A more detailed description of the calibration can be found in Ref. [84].

After calibration a typical measurement is performed in four parts. The sample is either illuminated by s- or p-polarized light and magnetized by an external field either parallel or perpendicular aligned with respect to the incidence plane of light. During each part of the measurement the magnetization curves are obtained for different azimuthal angles of the sample. The complete procedure of the measurement is controlled by an in-house developed program [85].

Afterwards, the four data sets are processed as described in Chap. 2.2.2.5 and Chap. 6 (Ref. [20]) including separation of linear and quadratic MOKE, adequate scaling of the curves and determination of all three magnetization components. The processing is also performed by an in-house developed analysis tool [86].

4.2.3 Proportionality between measured signal and MOKE

In the theoretic part of this thesis the relation between Kerr rotation and magnetization is discussed, which is in some special cases proportional (cf. Chap. 2.2.2.4). In order to prove, that the measured $2\,\Omega$ intensity signal is proportional to the Kerr rotation, the Jones matrix calculus [43] is used to describe the influence of the optical elements on the polarization of light.

The Jones vector $\vec{E}_s$ and $\vec{E}_p$ of incident s- and p-polarized light, respectively, are defined as

$$\vec{E}_s = E_0 \begin{pmatrix} 1 \\ 0 \end{pmatrix} \quad \text{and} \quad \vec{E}_p = E_0 \begin{pmatrix} 0 \\ 1 \end{pmatrix} . \tag{4.1}$$

The Jones matrix of the sample can be described by the complex reflection matrix $\hat{R}$ which is already defined in Eq. (2.32). The Jones matrix of the modulator $\hat{M}(\mu)$ with the angle μ between the modulation axis and the incidence plane of light is given by

$$\hat{M}(\mu) = \begin{pmatrix} \mathrm{e}^{i\,\Delta} \sin^2 \mu + \cos^2 \mu & \frac{1}{2}\,(\mathrm{e}^{i\,\Delta} - 1)\,\sin(2\,\mu) \\ \frac{1}{2}\,(\mathrm{e}^{i\,\Delta} - 1)\,\sin(2\,\mu) & \mathrm{e}^{i\,\Delta} \cos^2 \mu + \sin^2 \mu \end{pmatrix} \tag{4.2}$$

with the oscillating phase shift Δ between the modulated polarization part and the unmodulated polarization part of the light passing the modulator. Although μ is varied to obtain an optimum signal-to-noise ratio, this variation is so small, that $\mu \approx 0$ can be assumed. Therefore, Eq. (4.2) can be simplified to

$$\hat{M}(0^\circ) = \begin{pmatrix} 1 & 0 \\ 0 & \mathrm{e}^{i\,\Delta} \end{pmatrix} . \tag{4.3}$$

The analyzer Jones matrix $\hat{A}$ is generally defined as

$$\hat{A}(\nu) = \begin{pmatrix} \cos^2 \nu & \cos\nu\,\sin\nu \\ \cos\nu\,\sin\nu & \sin^2 \nu \end{pmatrix} \tag{4.4}$$

with the angle ν between polarization axis and the incidence plane of light. For an analyzer at $\nu = 45^\circ$ we obtain

$$\hat{A}(45^\circ) = \frac{1}{2} \begin{pmatrix} 1 & 1 \\ 1 & 1 \end{pmatrix} . \tag{4.5}$$

The intensity of the light reaching the diode I_s and I_p for s- and p-polarized incident light can be calculated via

$$I_{s/p} = \left| \hat{A}\,\hat{M}\,\hat{R}\,\vec{E}_{s/p} \right|^2 . \tag{4.6}$$

We obtain the proportionalities

$$\begin{aligned} I_s &\propto \sin\Delta\,\Im\left(-\frac{r_{ps}}{r_{ss}}\right) - \cos\Delta\,\Re\left(-\frac{r_{ps}}{r_{ss}}\right) \qquad \text{and} \\ I_p &\propto -\sin\Delta\,\Im\left(\frac{r_{sp}}{r_{pp}}\right) + \cos\Delta\,\Re\left(\frac{r_{sp}}{r_{pp}}\right)\ . \end{aligned} \tag{4.7}$$

After insertion of the oscillating phase shift $\Delta = \Delta_0\,\sin(\Omega\,t)$ with retardation Δ_0, modulation frequency Ω and time t into Eq. (4.7), the intensities can be expressed by the Bessel functions J_n of the n-th order. We use

$$\begin{aligned} \sin\left(\Delta_0\,\sin\left(\Omega\,t\right)\right) &= \sum_{n=0}^{\infty} 2\,J_{2\,n+1}\left(\Delta_0\right)\,\sin\left(\left(2\,n+1\right)\,\Omega\,t\right) \qquad \text{and} \\ \cos\left(\Delta_0\,\sin\left(\Omega\,t\right)\right) &= J_0\left(\Delta_0\right) + \sum_{n=1}^{\infty} 2\,J_{2\,n}\left(\Delta_0\right)\,\cos\left(2\,n\,\Omega\,t\right)\ . \end{aligned} \tag{4.8}$$

to conclude for the intensities

$$\begin{aligned} I_s &\propto J_1(\Delta_0)\,\Re\left(-\frac{r_{ps}}{r_{ss}}\right)\,\sin(\Omega\,t) - J_2(\Delta_0)\,\Re\left(-\frac{r_{ps}}{r_{ss}}\right)\,\cos(2\,\Omega\,t) \qquad \text{and} \\ I_p &\propto -\,J_1(\Delta_0)\,\Re\left(\frac{r_{sp}}{r_{pp}}\right)\,\sin(\Omega\,t) + J_2(\Delta_0)\,\Re\left(\frac{r_{sp}}{r_{pp}}\right)\,\cos(2\,\Omega\,t)\ . \end{aligned} \tag{4.9}$$

For small Kerr effects the real part and the imaginary part can be exchanged by the Kerr rotation and the Kerr ellipticity using Eq. (2.41). The lock-in amplifier separates the Ω and the $2\,\Omega$ contributions from the residual signal. The results prove the proportionality between the measured signal, either Ω or $2\,\Omega$, and the Kerr ellipticity or Kerr rotation, respectively. We obtain

$$\begin{aligned} I_s^{\Omega} &\propto J_1(\Delta_0)\,\epsilon_s\ , \qquad I_s^{2\,\Omega} \propto -J_2(\Delta_0)\,\Theta_s\ , \\ I_p^{\Omega} &\propto -\,J_1(\Delta_0)\,\epsilon_p\ , \qquad I_p^{2\,\Omega} \propto J_2(\Delta_0)\,\Theta_p\ . \end{aligned} \tag{4.10}$$

4.3 Determination of structural properties

The XRR and XRD experiments for the determination of structural properties are performed at synchrotron beamlines. The synchrotron radiation has a high brilliance compared to laboratory x-ray tubes. Therefore, the measurements are less time-consuming and have improved statistically accuracy. The setups of the beamlines W1 and BW2 at HASYLAB (DESY, Hamburg) and of the beamline BL9 at DELTA (Dortmund) are introduced in the following.

4.3.1 Beamline W1 and BW2 at HASYLAB (DESY)

X-rays at the beamlines W1 and BW2 are provided by the storage ring DORIS III at HASYLAB. Here, synchrotron radiation is generated by the acceleration of positrons to a velocity near the speed of light and a maximum kinetic energy of 4.45 GeV. The positrons are guided through a linear array of alternating oriented dipole magnets (so-called wiggler). Thus, the tangential emitted radiation is channeled and divergent, broadband synchrotron radiation is emitted with high intensity.

The wiggler at BW2 consists of 56 dipole magnets compared to the W1 wiggler which has 32 dipole magnets. Since the intensity of the light is proportional to the number of dipole magnets, the intensity of the x-rays obtained at beamline BW2 is higher than at beamline W1. This is the main difference between both beamlines. The further experimental setup is almost identical.

In order to obtain monochromatic radiation double crystal Si(111) monochromators are implemented to extract x-rays with a specific wavelength. In this work, x-ray light with a wavelength of $\lambda = 1.18\,\text{Å}$ and $\lambda = 1.24\,\text{Å}$ is used according to the photon energies of $E = 10.5\,\text{keV}$ and $E = 10\,\text{keV}$, respectively.

The beam can be focussed onto the sample by a system of Au-coated mirrors, while the form of the beam can be varied by a slit system. A motor controlled Al-absorber system is implemented to prevent the detector from damage through higher radiation intensities. The Al-absorber plates have different thicknesses and can be moved into the beam depending on the intensity signal obtained by the monitor counter which is placed before the absorber unit. The scattered x-ray photons are detected by a MYTHEN line detector [87].

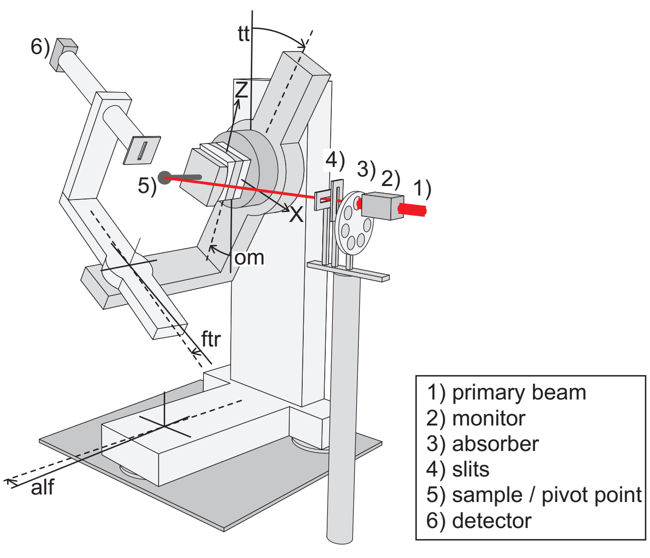

Figure 4.4: Experimental diffractometer setup at beamlines W1 and BW2 (adopted from Ref. [71] and edited).

The six-circle diffractometer at the beamlines W1 and BW2 is sketched in Fig. 4.4. The most important angles which can be varied during the measurements are om, tt, ftr and alf. The sample can be mounted in the pivot point of the diffractometer in two different ways.

In the horizontal alignment, alf and ftr are constant at 0°. Then, the rotation axis of om which rotates the sample is perpendicular to the incidence plane of the x-rays. The detector is rotated by tt within the incidence plane. Therefore, its rotation axis is also perpendicular to the incidence plane. Thus, the sample surface is parallel to the rotation axis of the om and tt circle. Here, om defines the incidence angle and tt the scattering angle. In this geometry, the XRR and XRD measurements are performed by variation of om and tt.

In the vertical alignment the sample surface is perpendicular to the rotation axis of om and tt. In this geometry, the detector can be rotated out of the incidence plane by ftr which has its rotation axis parallel to the incidence plane and perpendicular to the rotation axes of om and tt. The complete diffractometer can be tilted by alf. The rotation axis of alf is also parallel to the incidence plane and perpendicular to the rotation axes of om and tt, but in general, it is not parallel to the rotation axis of ftr. Now, alf is the incidence angle and tt in combination to ftr defines the scattering angle. Furthermore, om rotates the sample azimuthally around the sample normal. Using small constant alf angles in this geometry (above the critical angle of total reflection), GIXRD measurements are performed.

4.3.2 Beamline BL9 at DELTA

The storage ring of the synchrotron radiation source DELTA is operated with electrons at a maximum energy of 1.5 GeV [88]. Since this energy (and also the intensity of the beam) is smaller than the energy (and the intensity) at DORIS III, the statistically accuracy is lower than at HASYLAB. Thus, the measurement time has to be increased to observe reliable experimental data.

In principle, the beamline and the diffractometer at BL9 are identical to the W1/BW2 setup for XRR. However, a NaI point detector is used instead of the MYTHEN line detector as implemented at W1/BW2. Furthermore, the wavelength of the used x-ray photons is $\lambda = 0.80\,\text{Å}$ according to a photon energy of $E = 15.5\,\text{keV}$.

For the GIWAXS setup a 2D MAR345 image plate detector is used and an additional sample

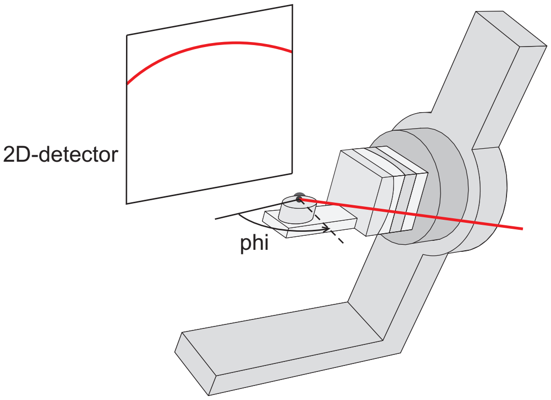

Figure 4.5: Experimental diffractometer setup at beamlines BL9 using a 2D-detector (adopted from Ref. [71] and edited).

station is built in (cf. Fig 4.5). This station includes a phi motor to rotate the sample azimuthally in horizontal alignment. Thus, 2D GIWAXS pattern of e.g. polycrystalline rings can be detected for different azimuthal sample angles.

The scattering geometry for the GIWAXS setup is additionally sketched in Fig. 4.6. Here, the constant incidence angle ϑ and the wide scattering angle Θ are marked. This sketch corresponds to Fig. 2.32 which shows the reciprocal space in GIWAXS geometry. The intersection area of Bragg sphere and Ewald sphere is observed on the 2D detector.

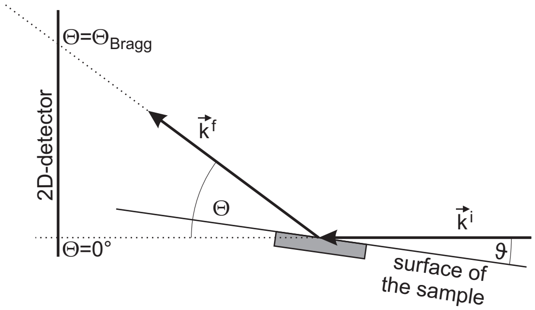

Figure 4.6: Sketch of scattering geometry for GIWAXS with small constant incidence angle ϑ and wide scattering angle Θ. The 2D-detector observes the intersection area of Bragg sphere and Ewald sphere of Fig. 2.32.

Original publication: Journal of Applied Physics **109**, 093907 (2011)
available at `http://dx.doi.org/10.1063/1.3576135`

Uniaxial magnetic anisotropy for thin Co films on glass studied by magnetooptic Kerr effect

T. Kuschel*, T. Becker*, D. Bruns*, M. Suendorf*, F. Bertram**, P. Fumagalli***, and
J. Wollschläger*, [1]

* *Fachbereich Physik, Universität Osnabrück, Barbarastraße 7, D-49069 Osnabrück, Germany*
** *Hamburger Synchrotronstrahlungslabor am Deutschen Elektronen-Synchrotron, Notkestraße 85, D-22607 Hamburg, Germany*
*** *Institut für Experimentalphysik, Freie Universität Berlin, Arnimallee 14, D-14195 Berlin, Germany*

Abstract

Thin Co films of different thickness deposited on glass are investigated by magnetooptic Kerr effect to study the uniaxial magnetic anisotropy of these films. The direction of the uniaxial magnetic anisotropy is determined from the azimuthal dependence of the magnetic remanence and differs with increasing thickness of the Co film investigated by x-ray reflectivity. Our experiments reveal that preparation conditions like temperature, deposition rate, or obliqueness of deposition cannot be the reason for this rotation effect of the uniaxial magnetic anisotropy. Also, strain in the substrate and possible textures in the film structure can be excluded as the origin of the magnetic behavior as studied by grazing incidence wide angle x-ray scattering. Thus, probably only the substrate shape in connection with the amorphous or polycrystalline film structure can explain the rotation of the uniaxial magnetic anisotropy.

---

[1] Electronic mail: joachim.wollschlaeger@uos.de

Original publication: Journal of Physics D: Applied Physics **44**, 265003 (2011)
available at `http://dx.doi.org/10.1088/0022-3727/44/26/265003`

Vectorial magnetometry using magnetooptic Kerr effect including first- and second-order contributions for thin ferromagnetic films

T. Kuschel*, H. Bardenhagen**, H. Wilkens*, R. Schubert*, J. Hamrle***, J. Pištora***, and J. Wollschläger* [2]

* *Fachbereich Physik, Universität Osnabrück, Barbarastraße 7, D-49069 Osnabrück, Germany*
** *Physikalisches Institut, Universität Würzburg, Am Hubland, D-97074 Würzburg, Germany*
*** *Department of Physics and Nanotechnology Centre, VSB - Technical University of Ostrava, 17. listopadu 15, 70833 Ostrava-Poruba, Czech Republic*

Abstract

A new combination of different vectorial magnetometry techniques using magnetooptic Kerr effect is described. The processing of the experimental data contains the separation of linear and quadratic parts of the magnetization curves and determination of all three components of the magnetization vector in units of Kerr rotation without any normalization to the saturation values. The experimental procedure includes measurements with parallel and perpendicular polarized incident light and an external magnetic field parallel and perpendicular to the plane of incidence of light. The determination of the complex Kerr amplitude and the theoretic description of the data processing in assumption of small angles of incidence and also for larger angles of incidence using adequate scaling to the mean saturation value validate this vectorial magnetometry method. In case of an absent out-of-plane component of the magnetization vector, the complete reversal process can easily be reconstructed and interpreted by monodomain states and domain splitting. The measurement procedure and the processing of the data is demonstrated for an ultra-thin epitaxial Fe film on MgO(001).

---

[2] Electronic mail: joachim.wollschlaeger@uos.de

Original publication: Journal of Physics D: Applied Physics **45**, 495002 (2012)
available at `http://dx.doi.org/10.1088/0022-3727/45/49/495002`

Magnetic characterization of thin $Co_{50}Fe_{50}$ films by magnetooptic Kerr effect

T. Kuschel*, J. Hamrle**, J. Pištora**, K. Saito***, S. Bosu***, Y. Sakuraba***, K. Takanashi*** and J. Wollschläger* [3]

* *Fachbereich Physik, Universität Osnabrück, Barbarastraße 7, D-49069 Osnabrück, Germany*
** *Department of Physics and Nanotechnology Centre, VSB - Technical University of Ostrava, 17. listopadu 15, 70833 Ostrava-Poruba, Czech Republic*
*** *Institute for Materials Research (IMR), Tohoku University, Katahira 2-1-1, Aoba-ku, Sendai 980-8577, Japan*

Abstract

Magnetic properties of thin $Co_{50}Fe_{50}$ films on MgO(001) prepared with different annealing temperatures between room temperature and 300°C are studied by vectorial magnetometry based on magnetooptic Kerr effect. Independent from the annealing the $Co_{50}Fe_{50}$ films reveal some similar magnetic properties as no quadratic magnetooptic Kerr effect and a magnetic reversal process which is completely in-plane with magnetic easy axes in $Co_{50}Fe_{50}$ $\langle 110 \rangle$ directions. If the alignment of the external magnetic field is close to the magnetic hard axes, incoherent rotation of magnetic moments between saturation and remanence occurs instead of coherent rotation as for the other directions. If the magnitude of the magnetization is polar plotted with respect to the azimuthal magnetization angle, sequential switching of magnetic moments from one magnetic easy axis to another can be proved by the course of the magnetization. Here, a two-domain switching process can be distinguished from a four-domain switching process generated by the incoherent rotation between saturation and remanence. Furthermore, both the uniaxial magnetic anisotropy constants and the domain wall pinning energies are determined from the magnetic switching fields using the Stoner-Wohlfarth model while the cubic magnetic anisotropy constants are obtained from fitting the magnetization curves. The domain wall pinning energies obtained from these analyses decrease with increasing annealing temperature due to fewer defects in the film. The cubic magnetic anisotropy also decreases slightly which can be attributed to relaxation of the crystal lattice for increasing annealing temperature due to a small change of spin-orbit coupling. Compared to the cubic magnetic anisotropy the uniaxial magnetic anisotropy is very small. This may be attributed to the reduction of strain in the film caused by a buffer stack Cr/Au/Cr between the $Co_{50}Fe_{50}$ film and MgO(001).

---

[3] Electronic mail: joachim.wollschlaeger@uos.de

Original publication: Journal of Physics D: Applied Physics **45**, 205001 (2012)
available at `http://dx.doi.org/10.1088/0022-3727/45/20/205001`

Magnetization reversal analysis of a thin B2-type ordered $Co_{50}Fe_{50}$ film by magnetooptic Kerr effect

T. Kuschel*, J. Hamrle**, J. Pištora**, K. Saito***, S. Bosu***, Y. Sakuraba***, K. Takanashi*** and J. Wollschläger* [4]

* *Fachbereich Physik, Universität Osnabrück, Barbarastraße 7, D-49069 Osnabrück, Germany*
** *Department of Physics and Nanotechnology Centre, VSB - Technical University of Ostrava, 17. listopadu 15, 70833 Ostrava-Poruba, Czech Republic*
*** *Institute for Materials Research (IMR), Tohoku University, Katahira 2-1-1, Aoba-ku, Sendai 980-8577, Japan*

Abstract

The magnetic structure of a thin B2 ordered $Co_{50}Fe_{50}$ film is determined by vectorial magnetometry using magnetooptic Kerr effect including different polarizations of the incident light and varied directions of the external magnetic field. Both the magnetic reversal process and the magnetic remanence reveal two in-plane magnetic easy axes of different strengths which are not orthogonal. Atypical magnetization curves including multidomain states in magnetic remanence with some magnetic moments providing antiparallel alignment to the direction of the previously applied external field (if projected to the direction of the external field) confirm the appearance of different strong magnetic easy axes. This magnetic structure can be explained by a cubic magnetic anisotropy (CMA) induced by the crystalline film structure superimposed by an additional uniaxial magnetic anisotropy (UMA) which is not parallel to one of the magnetic easy axes of the CMA. The results are compared with the regular magnetic behavior of a thin A2 ordered $Co_{50}Fe_{50}$ film with UMA parallel to one of the magnetic easy axes of the CMA.

---

[4] Electronic mail: joachim.wollschlaeger@uos.de

9 Structural and magnetic properties of Fe films on MgO(001)

In Chap. 6 (Ref. [20]) the basic MOKE analysis of an exemplary Fe film on MgO(001) is shown. In order to extend the magnetic characterization, the magnetic anisotropy properties are obtained from the Stoner-Wohlfarth model in the present chapter and compared with the structural properties determined by XRR and XRD.

9.1 Structural properties

XRR measurements for Fe films of different thicknesses are performed. Two exemplary reflectometry curves are shown in Fig. 9.1 for a 7 nm Fe film and a 22 nm Fe film.

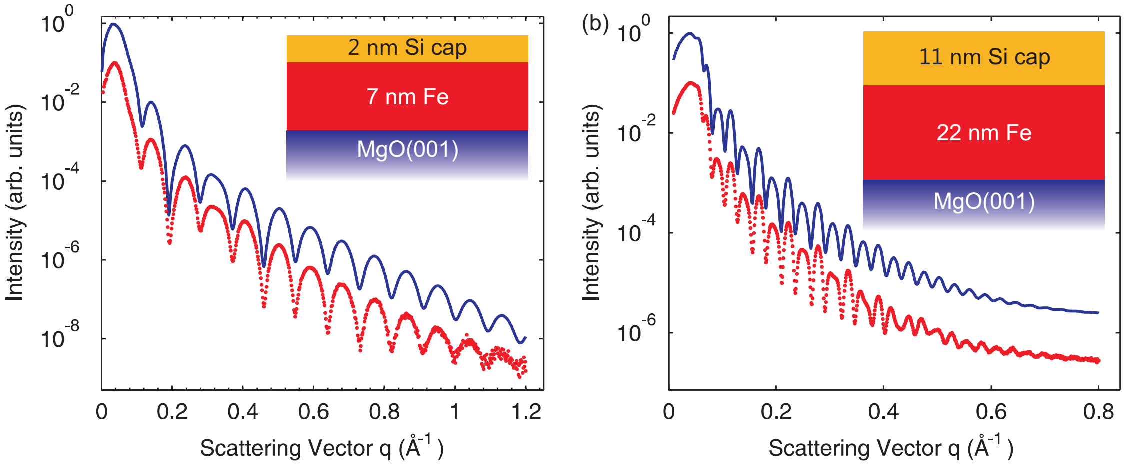

Figure 9.1: XRR measurements of exemplary Fe films (dots, lower curves) and simulation of the data (solid line, upper curves) by means of the respective structure models (insets). (a) The 2 nm Si capping layer and the 7 nm Fe film exhibit a surface roughness of 0.6 nm and 0.2 nm, respectively. The roughness of the MgO substrate amounts to 0.2 nm. (b) The 11 nm Si capping layer and the 22 nm Fe film exhibit a surface roughness of 0.5 nm and 0.2 nm, respectively. The roughness of the MgO substrate amounts to 0.4 nm. The curves are shifted for clarity.

The model shown in the inset of Fig. 9.1(a) describes the reflectometry curve of the 7 nm Fe film accurately. The thickness of the Si capping layer amounts to 2 nm. The surface roughness of each interface is about 0.2 nm up to 0.6 nm. The reflectometry curve of the 22 nm film reveals a Si capping layer thickness of 11 nm and interface roughnesses of 0.2 nm up to 0.5 nm, respectively. Additional Fe films of 4 nm and 6 nm are investigated.

Exemplary specular diffraction measurements in Fig. 9.2 present the (00) diffraction rod with substrate Bragg peaks at the reciprocal lattice values $L = 1$ and $L = 2$. The Bragg peaks of Fe film and MgO substrate are separated, since the atomic lattice distances d of both structures differ. The bulk values are $d_{\text{bulk}} = 2.11\,\text{nm}$ for MgO and $d_{\text{bulk}} = 1.43\,\text{nm}$ for Fe, respectively.

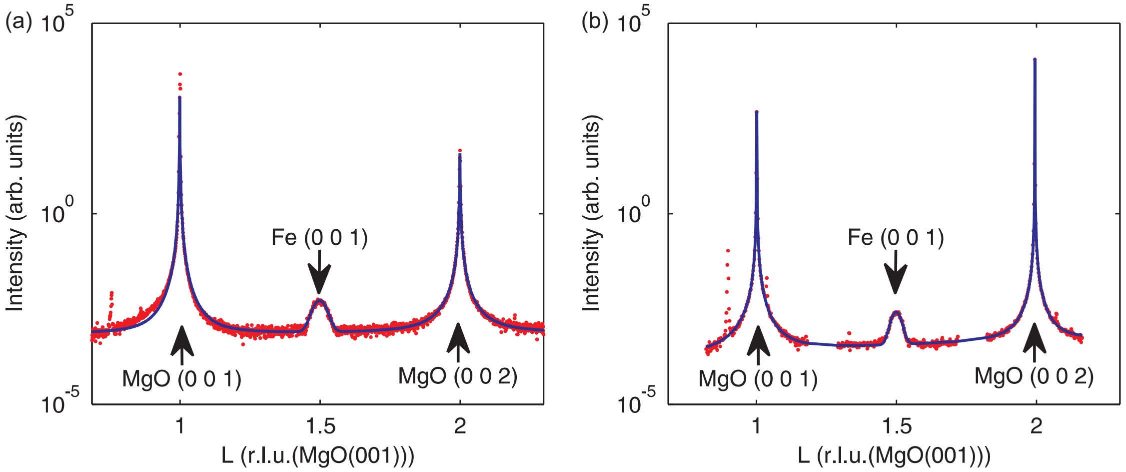

Figure 9.2: XRD measurement of exemplary Fe films (dots) and fit of the Bragg peaks (solid lines). (a) The Fe(001) Bragg peak of the 4 nm Fe film is located at $L = 1.498$ with a FWHM of $\Delta L_{\mathrm{FWHM}} = 0.052$. (b) The Fe(001) Bragg peak of the 22 nm Fe film is located at $L = 1.480$ with a FWHM of $\Delta L_{\mathrm{FWHM}} = 0.012$. Some small peaks beside the MgO(001) Bragg peak can be attributed to higher harmonics.

For the 4 nm film (Fig. 9.2(a)) the Fe(001) Bragg peak position is $L = 1.498$ which corresponds to an atomic layer distance of 1.41 Å and a vertical lattice constant of $c = 2.81$ Å. This value is 2% decreased compared with the bulk value of $c_{\mathrm{bulk}} = 2.87$ Å.

Since the Fe(001) Bragg peak shows no oscillations, the film is not completely homogeneous. Therefore, the vertical crystallite size has to be determined by the FWHM of ΔL_{FWHM} of the Fe(001) peak instead of the oscillation distances. We obtain $\Delta L_{\mathrm{FWHM}} = 0.052$ which leads to a vertical crystallite size of $S_{\mathrm{vert}} = 4$ nm. This value is in accordance with the film thickness. Thus, we have no disordered interfaces.

The 22 nm film (Fig. 9.2(b)) reveals a Fe(001) Bragg peak at $L = 1.480$ according to an atomic layer distance of 1.42 Å and a vertical lattice constant of $c = 2.85$ Å, which is 0.8% decreased compared with the bulk value.

The Fe(001) peak exhibits a FWHM of $\Delta L_{\mathrm{FWHM}} = 0.012$ corresponding to a vertical crystallite size of $S_{\mathrm{vert}} = 15$ nm. This value is quite smaller than the film thickness. Probably, there are interfaces which are not crystalline. The vertical lattice constants c and the vertical crystallite sizes S_{vert} of all four samples are summarized in Tab. 9.1.

Furthermore, GIXRD measurements are performed on the Fe films. Exemplary diffraction patterns in $H = K$ direction are presented in Fig. 9.3 projected to the H direction. The Fe(110) Bragg peak is next to the MgO(110) Bragg peak, since the surface lattice constant of MgO(001) ($a_S = 2.98$ Å) differs only 3.7% from the lattice constant of Fe.

Here, the substrate peak shape is not as sharp as the substrate peak shape of the specular rod Bragg peaks. This is reasonable, since the origin of the in-plane peaks can not be reached with the given technique as already explained in Chap. 2.3.2.3. Thus, the diffraction pattern

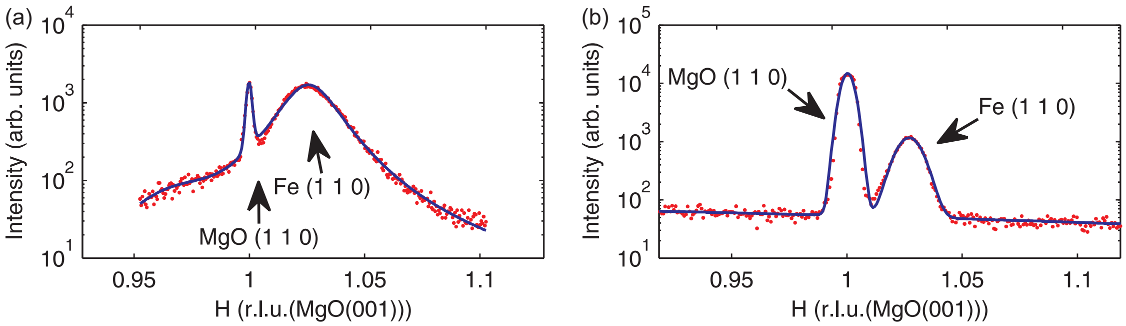

Figure 9.3: GIXRD measurement of exemplary Fe films (dots) and fit of the Bragg peaks (solid lines). (a) The Fe(110) Bragg peak of the 4 nm Fe film is located at $H = 1.023$ with a FWHM of $\Delta H_{\mathrm{FWHM}} = 0.024$. (b) The Fe(110) Bragg peak of the 22 nm Fe film is located at $H = 1.026$ with a FWHM of $\Delta H_{\mathrm{FWHM}} = 0.013$.

shows the flank of the peaks. Nevertheless, it is assumed that the center of an in-plane peak differs in its L value from the obtained pattern, but has similar H and K values.

The Fe(110) peak position of the 4 nm film (Fig. 9.3(a)) amounts to $H = 1.023$ and corresponds to a lateral lattice constant of $a = 2.91$ Å. This value is 1.5% increased compared to the bulk value because the film lattice adapts the given substrate structure. Due to volume conservation the vertical lattice constant is therefore decreased. Thus, the Fe film is tetragonal distorted. The 22 nm film shows the similar tetragonal distortion in the GIXRD pattern (Fig. 9.3(b)), since the Fe(001) peak is located at $H = 1.026$ according to $a = 2.90$ Å.

Assuming no mosaics or other effects which could influence the peak shape, we also use the FWHM to calculate the lateral crystallite size. The FWHM of the Fe(110) peaks reveal $\Delta H_{\mathrm{FWHM}} = 0.024$ and $\Delta H_{\mathrm{FWHM}} = 0.013$ for the 4 nm and the 22 nm film, respectively. The resulting lateral crystallite sizes are $S_{\mathrm{lat}} = 8$ nm and $S_{\mathrm{lat}} = 15$ nm. All lateral lattice constants a and lateral crystallite sizes S_{lat} of all four samples are summarized in Tab. 9.1.

thickness D (nm)	vert. lattice constant a (Å)	vert. cryst. size S_{vert} (nm)	lat. lattice constant c (Å)	lat. cryst. size S_{lat} (nm)
4	2.81	4	2.91	8
6	2.81	5	2.96	7
7	2.84	5	2.91	11
22	2.85	15	2.90	15

Table 9.1: Determination of the film thickness D by XRR, the vertical and lateral lattice constants a and c, respectively, as well as the vertical and lateral crystallite sizes S_{lat} and S_{vert}, respectively.

9.2 Magnetic properties

All Fe films have a cubic magnetocrystalline anisotropy as exemplarily shown in Chap. 6 (Ref. [20]) for the magnetic remanence. Nevertheless, all samples reveal an additional UMA superimposed to the CMA. The UMA is supposed to be parallel to one of the easy axes of the CMA for all four samples. Thus, the processing of the switching field analysis introduced in Chap. 7 (Ref. [21]) is performed to obtain the domain wall pinning energy ϵ_{90° and the uniaxial magnetic anisotropy constant K_U.

In Fig. 9.4 the reciprocal switching fields H_A and H_B are plotted against the azimuthal sample angle α and fitted to a phase shifted sine curve by the use of Eq. (2.17). The amplitudes $A_{A/B}$ of the sine curves yield the magnetic constants by Eq. (2.19). The exemplary processing is done for the 4 nm Fe film.

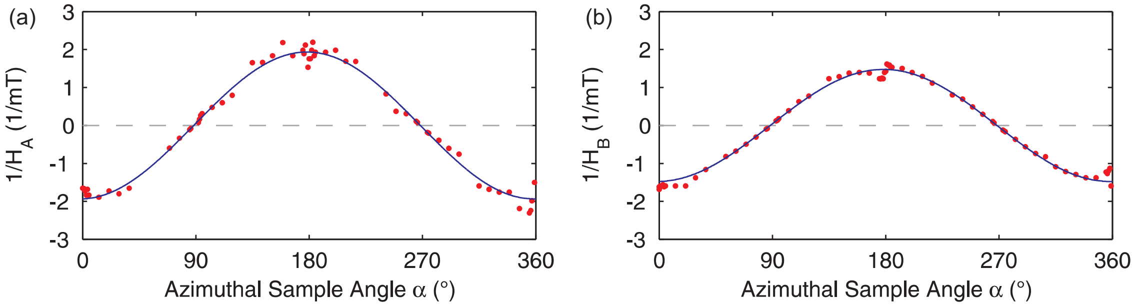

Figure 9.4: Fitting of the reciprocal switching field depending on the sample angle α for the 4 nm Fe film. (a) Reciprocal switching field $1/H_A$ with amplitude $A_A = -1.94\,\mathrm{mT}^{-1}$. (b) Reciprocal switching field $1/H_B$ with amplitude $A_B = -1.48\,\mathrm{mT}^{-1}$.

The resulting magnetic constants are $\frac{\epsilon_{90^\circ}}{M_S} = 0.84\,\mathrm{mT}$ and $\frac{K_U}{M_S} = 0.11\,\mathrm{mT}$ for the 4 nm Fe film. After determination of the magnetic constants for all four samples we obtain UMA constants K_U with different sign. This is due to the definition of the $\alpha = 0^\circ$ direction in relation to the direction of the UMA and has no influence on the further results. Therefore, we just table the absolute values. The domain wall pinning energy ϵ_{90° and the UMA constant K_U for all samples are summarized in Tab. 9.2.

We now examine the CMA constant K_1 and the maximum Kerr rotation representing the saturation magnetization M_S in units of Kerr rotation by fitting the coherent reversal part of the hystereses. As similarly done for the $\mathrm{Co}_{50}\mathrm{Fe}_{50}$ samples in Chap. 7 (Ref. [21]) we use the Stoner-Wohlfarth model from Eq. 2.20 to fit simultaneously all magnetization curves of one Fe film.

In Fig. 9.5 the fitting result for some exemplary sample angles α is shown. The curve fitting of the 7 nm Fe film yield a CMA constant $\frac{K_1}{Ms} = 29.3\,\mathrm{mT}$ and a saturation magnetization $M_s = 74.3\,\mathrm{mdeg}$ according to the maximum Kerr rotation of that sample.

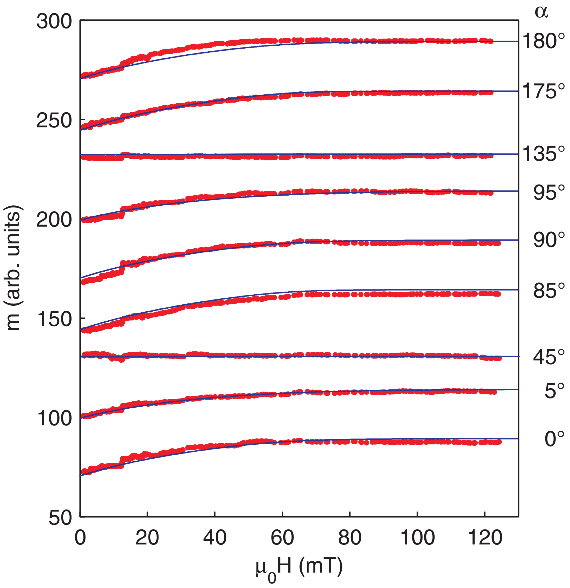

Figure 9.5: Coherent reversal part of the magnetization curves $m(H)$ (dots) for some exemplary azimuthal angles and simultaneous fit (solid line) of all curves for the 7 nm Fe film using the Stoner-Wohlfarth model. The curves are shifted for clarity.

thickness D (nm)	ϵ_{90°/M_S (mT)	K_U/M_S (mT)	K_1/M_S (mT)	M_S (mdeg)
4	0.84	0.11	19.1	63.5
6	1.41	0.09	44.0	17.4
7	0.40	0.24	29.3	74.3
22	0.20	0.03	41.9	93.3

Table 9.2: Determination of the domain wall pinning energy ϵ_{90°/M_S, the UMA constant K_U/M_S, the CMA constant K_1/M_S and the saturation magnetization M_S in units of Kerr rotation (i.e. maximum Kerr rotation in magnetic saturation) for all Fe samples.

9.3 Discussion

Some of the structural and magnetic parameters obtained from the Fe films relate to each other as discussed in the following. The tetragonal distortion of the cubic Fe lattice is decreasing with increasing film thickness, since the Fe film lattice constants and Fe bulk value converge with larger thicknesses. This can be explained by relaxation of the Fe lattice to its bulk size for thicker films.

The CMA constant K_1 increases for thicker films (except for the 7 nm film). This tendency is due to an influence of the interface anisotropy for thinner films. Thus, the effective CMA constant is reduced for thin films and reaches the bulk value for thicker films.

The UMA constant is independent from the film thickness. Its origin is growth-induced and can be caused by preparation conditions like substrate influence (stress, shape) or deposition parameters (angle of incidence, magnetic fields). The anisotropy constant ratio $\frac{K_U}{K_1}$ is for all samples below 1%, which is relatively low compared to literature values of about 10% [34] or even 40-90% [89].

The proportionality factor between Kerr rotation and magnetization can differ from sample to sample. Therefore, a strict interpretation of the devolution of the magnetization in SI units between different samples can not be done. Nevertheless, neglecting again the 7 nm film, the maximum Kerr rotation M_S increases with larger film thickness. This could be a hint to larger magnetization values (in SI units), but it is no prove.

The domain wall pinning energy ϵ_{90° is related to the defects in the film. In a magnetic film with a large defect density the magnetic domains need higher opposed fields to switch the magnetic moment into another direction. We assumed in Chap. 7 that different annealing temperatures of $Co_{50}Fe_{50}$ yield different defect densities. Furthermore, we obtained for increasing annealing temperatures that the domain wall pinning energy (and therefore, also the defect density) is reduced.

In order to confirm this statement, we want to plot ϵ_{90° of the Fe films against the lateral crystallite size S_{lat}, which is an indicator for the defect density. Films with larger lateral crystallite sizes have a lower defect density and vice versa. Fig. 9.6(a) shows that the expected relation between S_{lat} and ϵ_{90° is approved. The decrease of S_{lat} leads to an larger domain wall pinning energy. For reciprocal ϵ_{90° the relation is even linear (Fig. 9.6(b)).

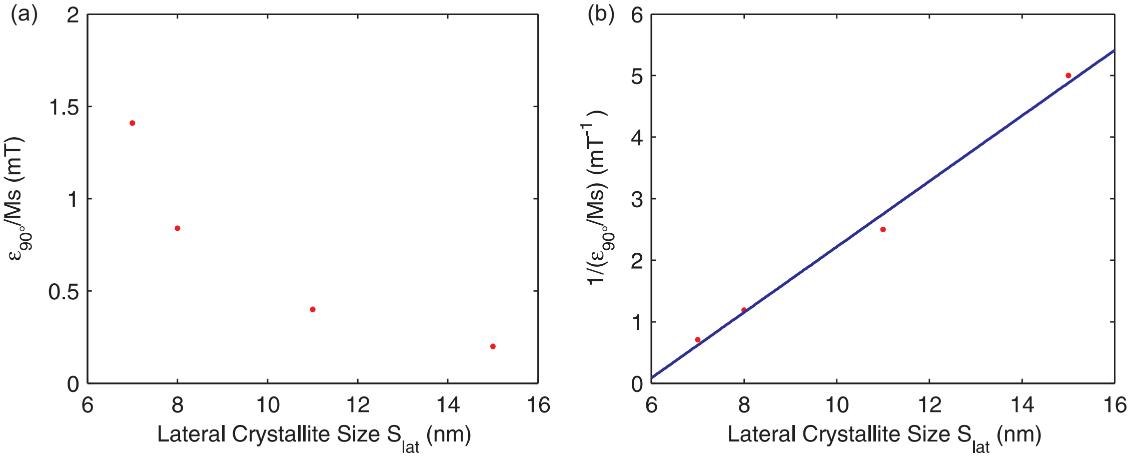

Figure 9.6: Domain wall pinning energy ϵ_{90° plotted against the lateral crystallite size S_{lat}. (a) Direct comparison. (b) Reciprocal plotting.

10 Summary and Outlook

The most important results of the present thesis are summarized in the following. Additionally, a short outlook to future investigations is given.

The studied amorphous and polycrystalline Co films on glass with thicknesses of 9 nm up to 90 nm are investigated by magnetooptic Kerr effect (MOKE) which is sensitive to the magnetization in the probed film. The thicknesses are determined by x-ray reflectivity (XRR). The MOKE results show mostly a uniaxial magnetic anisotropy (UMA) observable by the magnetic remanence depending on the azimuthal sample angle. Thus, the magnetization is aligned along the magnetic easy axis induced by the UMA for vanishing external magnetic field. This favored magnetic axis is aligned in different directions varying from sample to sample. The experiments reveal that preparation conditions like temperature, deposition rate and obliqueness of deposition can be excluded as an origin of the UMA.

Grazing incidence wide angle x-ray scattering (GIWAXS) measurements present amorphous and polycrystalline diffraction patterns. The hexagonal lattice constants and the sizes of the Co crystallites obtained from the diffraction rings are analyzed with respect to the azimuthal sample angle in order to search for structural preferred directions which induce the UMA. However, we did not observe a correlation between structural properties and direction of the UMA.

The anisotropy measurements show that the direction of the UMA depends on the thickness of the Co films. Amorphous ultrathin films and polycrystalline films of a thickness larger than 50 nm have a UMA directed parallel to the substrate edge. Only films of intermediate thickness show UMAs aligned in different directions. A probable explanation could be that for homogeneous amorphous and homogeneous polycrystalline films the shape anisotropy induces a favored magnetic axis. The anisotropy contribution of the shape anisotropy has no appreciable influence to the magnetic direction in the intermediate thickness range, since the inhomogeneous film structure already induces a randomly distributed magnetically favored direction.

For the investigations on crystalline films with cubic lattice structures, a new combination of different vectorial magnetometry techniques is developed in the present work on the base of the MOKE setup. Incident light with different linear polarizations (s and p) is used to separate the in-plane and the out-of-plane component of the magnetization vector by calculating the sum and the difference of the detected signals. Furthermore, a magnetic field parallel and perpendicular to the incidence plane of light is applied to obtain both in-plane components of the magnetization vector.

The measured magnetization curves are scaled to the mean saturation value of s- and p-polarized signal. Thus, the processing of the experimental data is valid for all incidence angles as theoretically derived by the analytical expressions of the permittivity tensor for cubic and tetragonal magnetic structures. One of the advantages of the introduced technique is the quantitative comparability of the magnetic behavior of different samples in units of Kerr rotation. The standard normalization of the magnetization curves which allows only qualitative estimations is not necessary due to the described adequate scaling.

The separation of the magnetization components is done after the linear and the quadratic part of the magnetization curves are determined by symmetrization and antisymmetrization of the hysteresis curves. These parts are due to the linear and the quadratic MOKE, respectively. The latter effect is huge in Fe films as well as in Co based intermetallic compounds and is assumed to be generated by a spin orbit interaction of the second order. The separation of linear and quadratic MOKE is valid for thin films without exchange bias effects.

The vectorial magnetometry analysis is performed on the crystalline cubic structured system Fe on MgO(001) with varied film thickness from 4 nm up to 22 nm. Furthermore, cubic structured $Co_{50}Fe_{50}$ films on MgO(001) with different annealing temperature from room temperature up to 400°C are investigated. All structures reveal a cubic magnetic anisotropy (CMA) due to the cubic crystal structure superimposed by a weak UMA, which is directly observable from the coercive field of the magnetization curves in different azimuthal sample directions. However, the magnetic remanence reveals in most cases only the fourfold CMA structure. Thus, the coercive field is more sensitive to the contributions of the UMA. In most cases the UMA is parallel aligned to one of the magnetic easy axes of the CMA resulting in orthogonal overall easy axes which have different strengths.

The determination of the magnetization components shows a negligible out-of-plane component for both investigated systems. Thus, the complete reversal process of the magnetization vector is performed in-plane. Furthermore, QMOKE is obtained for nearly all Fe films, but the effect is negligible in all $Co_{50}Fe_{50}$ films. The magnetic easy axes of the Fe films are parallel aligned to the edges of the cubic unit cell Fe<100>, while the magnetic easy axes of the $Co_{50}Fe_{50}$ films are parallel to the $Co_{50}Fe_{50}$<110> directions.

Since the magnitude of the magnetization can be determined by the magnetization components, the reversal process can be sectioned into coherent rotation parts with maximum magnetization and incoherent rotation parts regarding to the splitting of domains. This multidomain state is characterized by magnetic moments aligned in different directions. Thus, the total magnetization is reduced. For both investigated systems magnetization curves with incoherent rotation are observed, if the external magnetic field is aligned parallel to the magnetic hard direction which is energetically unfavorable for the magnetization. This incoherent rotation parts between the magnetization saturation and the magnetic remanence (when the external field is decreased) can be explained by the different rotation sense of different magnetic domains.

The magnetization switching for opposed applied external magnetic field can be advantageously visualized by polar plotting the magnitude of the magnetization vector against the rotation angle of the magnetization. If this switching is performed by sequential jumping of the magnetic moments from one magnetic easy axis to the next magnetic easy axis, the polar curve shows a straight line which is the vectorial summation of the magnetic moments aligned in two different magnetic easy directions.

This straight line characteristic occurs also for the reversal process, if the external field is aligned parallel to the magnetic hard direction. However, during the switching of the magnetization the straight line in the polar plot is composed of magnetic moments directing in all four different magnetic easy axes due to the different rotation sense of the magnetic moments. These four 90° multidomain states lead to a reduced switching magnetization compared to the reversal process where only two magnetic easy axes are involved in the switching.

The different anisotropy contributions can be described by the Stoner-Wohlfarth model which is valid for the coherent parts of the magnetization curves. Therefore, the reversal process for an external magnetic field parallel to different azimuthal sample directions is determined for both investigated systems. The external magnetic field for the switching process can be used to calculate the UMA constant K_U and the domain wall pinning energy ϵ_{90°, if this field is reciprocally plotted against the azimuthal sample angle. Furthermore, these magnetic constants can be used to fit the coherent rotation part of the magnetization curves resulting in the CMA constant K_1 and the maximum Kerr rotation which corresponds to the saturation magnetization M_S in units of Kerr rotation.

The different annealed $Co_{50}Fe_{50}$ films which reveal a UMA parallel to one of the CMA easy axes have similar CMA constants K_1 and similar saturation magnetizations M_S. This is an indication for comparable atomic and electronic structures in the film. The UMA constant K_U seems to be independent from the annealing temperature. Thus, this growth-induced anisotropy is generated by deposition parameters which are independent from the annealing temperature. The ratio $\frac{K_U}{K_1}$ is relatively low compared to the literature. The reason could be the stress reduction due to the Cr buffer layer which was implemented between MgO substrate and $Co_{50}Fe_{50}$ film during sample preparation. The domain wall pinning energy ϵ_{90° decreases with increasing annealing temperature. An interpretation could be that the amount of defects in the film which influence the domain wall creation and propagation is reduced for higher annealing temperatures and therefore, the magnetization can switch more easily than in a film with a larger amount of defects.

The $Co_{50}Fe_{50}$ film with the annealing temperature of 400°C reveals different magnetic behavior. Here, the vectorial magnetometry data shows two overall magnetic easy axes which are not orthogonal and which have not the same strength. This resulting magnetic anisotropy could be caused by a CMA in combination to a UMA which is not parallel to one of the magnetic easy CMA axes. Since the anisotropy constant determination using the Stoner-Wohlfarth model can not be applied in this case due to symmetry reasons, further processing can not be done.

For the Fe films on MgO with different thicknesses obtained by XRR several specular diffraction patterns are observed using x-ray diffraction (XRD). From the Fe peak positions and the FWHM of the peaks the vertical lattice constants and the vertical crystallite sizes are determined. Furthermore, grazing incidence x-ray diffraction (GIXRD) was performed to obtain the lateral lattice constants and the lateral crystallite sizes. All samples show tetragonal distortion of the crystal unit cell due to the fitment of lateral lattice constant to the surface lattice constant of the substrate. The vertical crystallite sizes matches to the film thicknesses for thinner films. The vertical crystallite sizes of the thicker films are smaller than the film thicknesses which is related to some disordered interfaces.

The determination of the magnetic constants by fitting the switching fields of the magnetization curves yield increasing CMA constants K_1 with larger film thicknesses. This can be explained by a decreasing influence of the interface anisotropy for thicker films. For thinner films this interface anisotropy reduces the effective CMA constants. Similar to the $Co_{50}Fe_{50}$

films the obtained UMA constant K_U seems to be independent from the varied parameters and the ratio $\frac{K_U}{K_1}$ is again relatively low compared to the literature.

Comparison of the domain wall pinning energy ϵ_{90° and the lateral crystallite sizes of the Fe films reveals a reciprocal dependence. For larger lateral crystallite sizes we obtain smaller ϵ_{90° values due to a smaller amount of defects in the films. This interpretation of the ϵ_{90° development is consistent to the $Co_{50}Fe_{50}$ films.

For future investigations, the magnetic constant determination using the Stoner-Wohlfarth model has to be extended to obtain these constants also for magnetic anisotropies with a UMA not parallel to one of the CMA easy axes. The origin of the varying direction between UMA and CMA should be investigated.

Furthermore, the vectorial magnetometry technique should also be applied on magnetic thin films with an reversal process including all three magnetization components (not only in-plane) in order to absolutely verify the experimental approach and the theoretical derivation of the technique. Thin films with different crystal structures (not only cubic and tetragonal) should be observed by the MOKE technique attendant to theoretical calculations of the processing steps for separation of the magnetization components. Here, the processing of the obtained data for all general crystal structures is not clear up to now.

The magnetic easy directions of the $Co_{50}Fe_{50}$ films are 45° rotated to the magnetic easy axes of the Fe films concerning the cubic unit cell of the crystal. The transition of this rotation from pure cubic Fe films to films with Co contributions should be analyzed also concerning the magnetic anisotropy constants.

In order to verify the dependence between the domain wall pinning energy and the lateral crystallite size more samples with varying parameters have to be investigated. Additionally, more in-plane Bragg peaks have to be studied for each sample by GIXRD to consider possible mosaic effects or variations of the lateral lattice constants.

Bibliography

[1] G. Binasch, P. Grünberg, F. Saurenbach, and W. Zinn. Enhanced magnetoresistance in layered magnetic structures with antiferromagnetic interlayer exchange. *Phys. Rev. B*, 39(7):4828, 1989.

[2] M. N. Baibich, J. M. Broto, A. Fert, F. Nguyen Van Dau, F. Petroff, P. Eitenne, G. Creuzet, A. Friederich, and J. Chazelas. Giant magnetoresistance of (001)Fe/(001)Cr magnetic superlattices. *Phys. Rev. Lett.*, 61(21):2472, 1988.

[3] M. Julliere. Tunneling between ferromagnetic films. *Phys. Lett. A*, 54(3):225, 1975.

[4] S.A. Wolf, D.D. Awschalom, R.A. Buhrman, J.M. Daughton, S. von Molna, M.L. Roukes, A.J. Chtchelkanova, and D.M. Treger. Spintronics: A spin-based electronics vision for the future. *Science*, 294:1488, 2001.

[5] S. Yuasa, T. Nagahama, A. Fukushima, J. Suzuki, and K. Ando. Giant room-temperature magnetoresistance in single-crystal Fe/MgO/Fe magnetic tunnel junctions. *Nature Materials*, 3:868, 2004.

[6] J.S. Moodera, L.R. Kinder, T.M. Wong, and R. Meservey. Large magnetoresistance at room temperature in ferromagnetic thin film tunnel junctions. *Phys. Rev. Lett.*, 74(16):3273, 1995.

[7] T. Miyazali and N. Tezuka. Giant magnetic tunneling effect in Fe/Al_2O_3/Fe junction. *J. Magn. Magn. Mater.*, 139(3):L231, 1995.

[8] J.E. Hirsch. Spin Hall effect. *Phys. Rev. Lett.*, 83(9):1834, 1999.

[9] Y.K. Kato, R.C. Myers, A.C. Gossard, and D.D. Awschalom. Observation of the spin Hall effect in semiconductors. *Science*, 306:1910, 2004.

[10] E. Saitoh, M. Ueda, and H. Miyajima. Conversion of spin current into charge current at room temperature: Inverse spin-Hall effect. *Appl. Phys. Lett.*, 88:182509–1, 2006.

[11] K. Uschida, S. Takanashi, K. Harii, J. Ieda, W. Koshibae, K. Ando, S. Maekawa, and E. Saitoh. Observation of the spin Seebeck effect. *Nature*, 455:778, 2008.

[12] M. Walter, J. Walowski, V. Zbarsky, M. Münzenberg, M. Schäfers, D. Ebke, G. Reiss, A. Thomas, P. Peretzki, M. Seibt, J.S. Moodera, M. Czerner, M. Bachmann, and C. Heiliger. Seebeck effect in magnetic tunnel junctions. *Nat. Mater.*, 10:742, 2011.

[13] W.H. Butler, X.-G. Zhang, T.C. Schulthess, and J.M. MacLaren. Spin-dependent tunneling conductance of Fe/MgO/Fe sandwiches. *Phys. Rev. B*, 63:054416, 2001.

[14] M. Bowen, V. Cros, F. Petroff, A. Fert, C. Martínez Boubeta, J.L. Costa-Krämer, J.V. Anguita, A. Cebollada, F. Briones, J.M. de Teresa, L. Morellón, M.R. Ibarra, F. Güell, F. Peiró, and A. Cornet. Large magnetoresistance in Fe/MgO/FeCo(001) epitaxial tunnel junctions on GaAs(001). *Appl. Phys. Lett.*, 79(11):1655, 2001.

[15] X.-G. Zhang and W.H. Butler. Large magnetoresistance in bcc Co / MgO / Co and FeCo / MgO / FeCo tunnel junctions. *Phys. Rev. B*, 70:172407, 2004.

[16] M. Yamamoto, T. Marukame, T. Ishikawa, K. Matsuda, T. Uemura, and M. Arita. Fabrication of fully epitaxial magnetic tunnel junctions using cobalt-based full-Heusler alloy thin film and their tunnel magnetoresistance characteristics. *J. Phys. D: Appl. Phys.*, 39:824, 2006.

[17] S. Tsunegi, Y. Sakuraba, M. Oogane, N.D. Telling, L.R. Shelford, E. Arenholz, G. van der Laan, R.J. Hicken, K. Takanashi, and Y. Ando. Tunnel magnetoresistance in epitaxially grown magnetic tunnel junctions using Heusler alloy electrode and MgO barrier. *J. Phys. D: Appl. Phys.*, 42:1, 2009.

[18] T. Kuschel. Aufbau einer Apparatur zur Messung des magnetooptischen Kerr-Effekts. Dipoma thesis, Universität Osnabrück, 2007.

[19] T. Kuschel, T. Becker, D. Bruns, M. Suendorf, F. Bertram, P. Fumagalli, and J. Wollschläger. Uniaxial magnetic anisotropy for thin Co films on glass studied by magnetooptic Kerr effect. *J. Appl. Phys.*, 109:093907, 2011.

[20] T. Kuschel, H. Bardenhagen, H. Wilkens, R. Schubert, J. Hamrle, J. Pištora, and J. Wollschläger. Vectorial magnetometry using magnetooptic Kerr effect including first and second-order contributions for thin ferromagnetic films. *J. Phys. D: Appl. Phys.*, 44:265003, 2011.

[21] T. Kuschel, J. Hamrle, J. Pištora, K. Saito, S. Bosu, Y. Sakuraba, K. Takanashi, and J. Wollschläger. Magnetic characterization of thin $Co_{50}Fe_{50}$ films by magnetooptic Kerr effect. *J. Phys. D: Appl. Phys.*, 45:495002, 2012.

[22] T. Kuschel, J. Hamrle, J. Pištora, K. Saito, S. Bosu, Y. Sakuraba, K. Takanashi, and J. Wollschläger. Magnetization reversal analysis of a thin B2-type ordered $Co_{50}Fe_{50}$ film by magnetooptic Kerr effect. *J. Phys. D: Appl. Phys.*, 45:205001, 2012.

[23] M. Volmer and A. Weber. Keimbildung in übersättigten Gebilden. *Z. Phys. Chem.*, 119:277, 1926.

[24] F.C. Frank and J.H. van der Merwe. One-dimensional dislocations. I. Static theory. *Proc. R. Soc. London, Ser. A*, 198:205, 1949.

[25] I.N. Stranski and L. von Krastanov. Zur Theorie der orientierten Ausscheidung von Ionenkristallen aufeinander. *Sitzungsber. Akad. Wiss. Wien. Math.-Naturwiss.*, 146:797, 1938.

[26] L. Vitos, A.V. Ruban, H.L. Skriver, and J. Kollár. The surface energies of metal. *Surf. Sci.*, 411:186, 1998.

[27] K. Kopitzki. *Einführung in die Festkörperphysik*. Teubner, 2. edition, 1989.

[28] E.C. Stoner and E.P. Wohlfarth. A mechanism of magnetic hysteresis in heterogeneous alloys. *Philos. Trans. R. Soc. London*, 240(826):599, 1948.

[29] C. Kittel. *Einführung in die Festkörperphysik*. Oldenbourg Wissenschaftsverlag, 14. edition, 2006.

[30] C. Kittel. Physical theory of ferromagnetic domains. *Rev. Mod. Phys.*, 21(4):541, 1949.

[31] O. Durand, J.R. Childress, P. Galtier, R. Bisaro, and A. Schuhl. Origin of the uniaxial magnetic anisotropy in Fe films grown by molecular beam epitaxy. *J. Magn. Magn. Mater.*, 145:111, 1995.

[32] Y. Park, E.E. Fullerton, and S.D. Bader. Growth-induced uniaxial in-plane magnetic anisotropy for ultrathin Fe deposited on MgO(001) by oblique-incidence molecular beam epitaxy. *Appl. Phys. Lett.*, 66:2140, 1995.

[33] Y.Z. Wu, C. Won, and Z.Q. Qiu. Magnetic uniaxial anisotropy of Fe films grown on vicinal Ag(001). *Phys. Rev. B*, 65:184419, 2002.

[34] J.M. Florczak and E.D. Dahlberg. Magnetization reversal in (100)Fe thin films. *Phys. Rev. B*, 44:9338, 1991.

[35] R.P. Cowburn, S.J. Gray, J. Ferre, J.A.C. Bland, and J. Miltat. Magnetic switching and in-plane uniaxial anisotropy in ultrathin Ag/Fe/Ag(l00) epitaxial films. *J. Appl. Phys.*, 78(12):7210, 1995.

[36] J. Kerr. On rotation of the plane of polarization by reflection from the pole of a magnet. *Phil. Mag.*, 3:321, 1877.

[37] Z.Q. Qiu and S.D. Bader. Surface magneto-optic Kerr effect. *Rev. Sci. Instr.*, 71(3):1243, 2000.

[38] M. Faraday. On the magnetization of light and the illumination of magnetic lines of force. *Philos. Trans. R. Soc. London*, 136(3):1, 1846.

[39] J. Hamrle. Magneto-optical determination of the in-depth magnetization profile in magnetic multilayers. PhD thesis, University Paris XI, Orsay and Charles University, Prag, 2003.

[40] P. Bruno, Y. Suzuki, and C. Chappert. Magneto-optical Kerr effect in a paramagnetic overlayer on a ferromagnetic substrate: A spin-polarized quantum size effect. *Phys. Rev. B*, 53(14):9214, 1996.

[41] C. C. Robinson. Longitudinal Kerr magneto-optic effect in thin films of iron, nickel, and permalloy. *J. Opt. Soc. A.*, 53(6):681, 1963.

[42] W. Reim and J. Schoenes. *Ferromagnetic materials: magneto-optical spectroscopy of f-electron systems*, volume 5, chapter 2, pages 133–236. North-Holland, 1990.

[43] R.C. Jones. A new calculus for the treatment of optical systems. *J. Opt. Soc. A.*, 31:488, 1941.

[44] R. M. A. Azzam and N. M. Bashara. *Ellipsometry and polarized light.* North-Holland, 1977.

[45] G. Metzger, P. Pluvinage, and R. Torguet. Termes linéaires et quadratiques dans l'effet magnéto-optique de Kerr. *Ann. Phys. (Paris)*, 10(5):5, 1965.

[46] Q.-M. Zhong, A.S. Arrott, B. Heinrich, and Z. Celinski. Surface magneto-optical Kerr effect for ultrathin Ni-Fe bilayers. *J. Appl. Phys.*, 67(9):4448, 1990.

[47] J. Hamrle, S. Blomeier, O. Gaier, B. Hillebrands, H. Schneider, G. Jakob, K. Postava, and C. Felser. Huge quadratic magneto-optical Kerr effect and magnetization reversal in the Co_2FeSi Heusler compound. *J. Phys. D: Appl. Phys.*, 40:1563, 2007.

[48] K. Postava, H. Jaffres, A. Schuhl, F. Nguyen van Dau, M. Goiran, and A.R. Fert. Linear and quadratic magneto-optical measurements of the spin reorientation in epitaxial Fe films on MgO. *J. Magn. Magn. Mater.*, 172:199, 1997.

[49] R.M. Osgood III, B.M. Clemens, and R.L. White. Asymmetric magneto-optic response in anisotropic thin films. *Phys. Rev. B*, 55(14):8990, 1997.

[50] S.-s. Yan, R. Schreiber, P. Grünberg, and R. Schäfer. Magnetization reversal in (0 0 1)Fe thin films studied by combining domain images and MOKE hysteresis loops. *J. Magn. Magn. Mater.*, 210:309, 2000.

[51] M. Buchmeier, R. Schreiber, D.E. Bürgler, and C.M. Schneider. Thickness dependence of linear and quadratic magneto-optical Kerr effects in ultrathin Fe(001) films. *Phys. Rev. B*, 79:064402, 2009.

[52] J.A.C. Bland, M.J. Baird, H.T. Leung, A.J.R. Ives, K.D. Mackay, and H.P. Hughes. Magnetic anisotropies and magnetic switching in Co films. *J. Magn. Magn. Mater.*, 113:178, 1992.

[53] O. Gaier, J. Hamrle, S.J. Hermsdoerfer, H. Schultheiß, B. Hillebrands, Y. Sakuraba, M. Oogane, and Y. Ando. Influence of the $L2_1$ ordering degree on the magnetic properties of Co_2MnSi Heusler films. *J. Appl. Phys.*, 103:103910, 2008.

[54] G. Wolf, J. Hamrle, S. Trudel, T. Kubota, Y. Ando, and B. Hillebrands. Quadratic magneto-optical Kerr effect in Co_2MnSi. *J. Appl. Phys.*, 110:043904, 2011.

[55] R.M. Osgood III, S.D. Bader, B.M. Clemens, R.L. White, and H. Matsuyama. Second-order magneto-optic effects in anisotropic thin fims. *J. Magn. Magn. Mater.*, 182:297, 1998.

[56] J. Hamrle, S. Blomeier, O. Gaier, B. Hillebrands, H. Schneider, G. Jakob, B. Reuscher, A. Brodyanski, M. Kopnarski, K. Postava, and C. Felser. Ion beam induced modification of exchange interaction and spin–orbit coupling in the Co_2FeSi Heusler compound. *J. Phys. D: Appl. Phys.*, 40:1558, 2007.

[57] P. Yeh. Optics of anisotropic layered media: 4x4 matrix algebra. *Surf. Sci.*, 96:41, 1980.

[58] Š. Višňovský. Magneto-optical ellipsometry. *Czech. J. Phys. B*, 36:625, 1986.

[59] Š. Višňovský, M. Nývlt, V. Prosser, R. Ropušník, R. Urban, J. Ferré, G. Pénissard, D. Renard, and R. Krishnan. Polar magneto-optics in simple ultrathin-magnetic-film structures. *Phys. Rev. B*, 52(2):1090, 1995.

[60] Š. Višňovský. Magneto-optic effects in ultrathin structures at longitudinal and polar magnetizations. *Czech. J. Phys.*, 48(9):1083, 1998.

[61] J. Zak, E.R. Moog, C. Liu, and S.D. Bader. Additivity of the Kerr effect in thin-film magnetic systems. *J. Magn. Magn. Mater.*, 88:L261, 1990.

[62] C.-Y. You and S.-C. Shin. Generalized analytic formulae for magneto-optical Kerr effects. *J. Appl. Phys.*, 84:541, 1998.

[63] J. Hamrle, J. Ferre, J.P. Jamet, V. Repain, G. Baudot, and S. Rousset. Vicinal interface sensitive magneto-optical Kerr effect: Application to Co/Au(322). *Phys. Rev. B*, 67:155411, 2003.

[64] Š. Višňovský. Magneto-optical permittivity tensor in crystals. *Czech. J. Phys. B*, 36:1424, 1986.

[65] P. Vavassori. Polarization modulation technique for magneto-optical quantitative vector magnetometry. *Appl. Phys. Lett.*, 77(11):1605, 2000.

[66] M Tolan. *X-Ray Scattering from Soft-Matter Thin Films, Materials Science and Basic Research.* Springer, 1998.

[67] F. Bertram. Röntgenreflektometrie an ultradünnen Schichten. Bachelor thesis, Universität Osnabrück, 2007.

[68] L.G. Parratt. Surface studies of solids by total reflection of x-rays. *Phys. Rev.*, 95(2):359, 1954.

[69] J. Als-Nielsen and D. McMorrow. *Elements of Modern X-Ray Physics.* John Wiley & Sons, 2001.

[70] L. Névot and P. Croce. Caractérisation des surfaces par réflexion rasante de rayons X. Application à l'étude du polissage de quelques verres silicates. *Revue de Physique Appliquée*, 15(3):761, 1980.

[71] S. Gevers. Praseodymia on non-passivated and passivated Si(111) surfaces. PhD thesis, Universität Osnabrück, 2010.

[72] H. Wilkens. Röntgen- und Vektor-MOKE-Untersuchung ferromagnetischer Fe-Schichten. Diploma thesis, Universität Osnabrück, 2010.

[73] F. Bertram. Röntgenstrukturanalyse von Oxidschichten. Master thesis, Universität Osnabrück, 2009.

[74] C. Marlière, D. Renard, and J. P. Chauvineau. Study of interface roughness and crystallographic structure of Au/Co/Au sandwiches. *Thin Solid Films*, 201:317, 1991.

[75] J.B. Wedding, M. Li, and G.-C. Wang. Magnetization reversal of a thin polycrystalline cobalt film measured by the magneto-optic Kerr effect (MOKE) technique and field-dependent magnetic force microscopy. *J. Magn. Magn. Mater.*, 204:79, 1999.

[76] A. Kharmouche, S.-M. Chérif, A. Bourzami, A. Layadi, and G. Schmerber. Structural and magnetic properties of evaporated Co/Si(100) and Co/glass thin films. *J. Appl. Phys.*, 37:2583, 2004.

[77] B. Presa, R. Matarranz, M.C. Contreras, J.F. Calleja, L.E. Fernandez-Outon, and K. O'Grady. Magnetic properties of nanocrystalline Co thin films grown on glass. *IEEE Trans. Magn.*, 44:2788, 2008.

[78] T. Becker. MOKE-Untersuchungen an ferromagnetischen Metallschichten. Dipoma thesis, Universität Osnabrück, 2008.

[79] W. Wang, M. Lüpke, M. Di Ventra, S.T. Pantelides, J.M. Gilligan, N.H. Tolk, I.C. Kizilyalli, P.K. Roy, G. Margaritondo, and G. Lucovsky. Coupled electron-hole dynamics at the Si/SiO_2 interface. *Phys. Rev. Lett.*, 81(19):4224, 1998.

[80] J.F. Lawler, R. Schad, S. Jordan, and H. van Kempen. Structure of epitaxial Fe films on MgO(100). *J. Magn. Magn. Mater.*, 165:224, 1997.

[81] J.L. Costa-Krämer, J.L. Menéndez, A. Cebollada, F. Briones, D. García, and A. Hernando. Magnetization reversal asymmetry in Fe/MgO(001) thin flms. *J. Magn. Magn. Mater.*, 210:341, 2000.

[82] A. Gloskovskii, G. Stryganyuk, S. Ouardi, G.H. Fecher, C. Felser, J. Hamrle, J. Pištora, S. Bosu, Y. Sakuraba, and K. Takanashi. Structure determination of thin CoFe films by anomalous x-ray diffraction. *in preparation.*

[83] K. Shikada, M. Ohtake, F. Kirino, and M. Futamoto. Microstructure and magnetic properties of FeCo epitaxial thin films grown on MgO single-crystal substrates. *J. Appl. Phys.*, 105:07C303, 2009.

[84] H. Bardenhagen. Vektor-MOKE-Untersuchungen an epitaktischen Eisenschichten. Diploma thesis, Universität Osnabrück, 2009.

[85] K. Balinski. Entwicklung einer Ansteuerungssoftware für eine magneto-optische Messapparatur. Bachelor thesis, Universität Osnabrück, 2010.

[86] R. Schubert. Entwicklung einer Software zur Analyse von magnetooptischen Daten. Bachelor thesis, Universität Osnabrück, 2009.

[87] W. Caliebe, U. Brüggmann, M. Lohmann, and P. Machek. *New Equipment at W1 - Technical report*. HASYLAB @ DESY, 2007.

[88] C. Krywka, M. Paulus, C. Sternemann, M. Volmer, A. Remhof, G. Nowak, A. Nefedov, B. Pöter, M. Spiegel, and M. Tolan. The new diffractometer for surface x-ray diffraction at beamline BL9 of DELTA. *J. Synchrotron Rad.*, 13:8, 2006.

[89] N.A. Morley, M.R.J. Gibbs, E. Ahmad, I. Will, and Y.B. Xu. MOKE hysteresis loop method of determining the anisotropy constants of ferromagnetic thin films: Fe on GaAs(1 0 0) with overlayers of Au and Cr. *J. Magn. Magn. Mater.*, 300:436, 2006.

List of Figures

List of peer-reviewed publications

- T. Kuschel, T. Becker, D. Bruns, M. Suendorf, F. Bertram, P. Fumagalli, and J. Wollschläger
  Uniaxial magnetic anisotropy for thin Co films on glass studied by magnetooptic Kerr effect
  Journal of Applied Physics **109**, 093907 (2011).
  available at `http://dx.doi.org/10.1063/1.3576135`
- T. Kuschel, H. Bardenhagen, H. Wilkens, R. Schubert, J. Hamrle, J. Pištora, and J. Wollschläger
  Vectorial magnetometry using magnetooptic Kerr effect including first- and second-order contributions for thin ferromagnetic films
  Journal of Physics D: Applied Physics **44**, 265003 (2011).
  available at `http://dx.doi.org/10.1088/0022-3727/44/26/265003`
- T. Kuschel, J. Hamrle, J. Pištora, K. Saito, S. Bosu, Y. Sakuraba, K. Takanashi, and J. Wollschläger
  Magnetic characterization of thin $Co_{50}Fe_{50}$ *films by magnetooptic Kerr effect*
  Journal of Physics D: Applied Physics **45**, 495002 (2012).
  available at `http://dx.doi.org/10.1088/0022-3727/45/49/495002`
- T. Kuschel, J. Hamrle, J. Pištora, K. Saito, S. Bosu, Y. Sakuraba, K. Takanashi, and J. Wollschläger
  Magnetization reversal analysis of a thin B2-type ordered $Co_{50}Fe_{50}$ *film by magnetooptic Kerr effect*
  Journal of Physics D: Applied Physics **45**, 205001 (2012).
  available at `http://dx.doi.org/10.1088/0022-3727/45/20/205001`

Acknowledgement

I would like to thank all the people, who supported me and my work through the last years. Without you this thesis could not have been written.

First, I want to acknowledge my advisor Prof. Joachim Wollschläger for giving me the possibility to prepare my PhD thesis in his group. He supported me in the topic of x-ray analysis with many good hints and advices, while he gave me the chance to explore the field of magnetooptics.

I thank Prof. Mirco Imlau and his group for the supply of several experimental components and for help in optical questions. Prof. Mirco Imlau is also acknowledged to adopt the secondary advisory part of this thesis. Many thanks to Prof. Alfred Ziegler and Monika Wesner, who also joined the examination commission.

I would like to acknowledge the Deutsche Forschungsgemeinschaft (DFG) via Graduate College 695 and its chair man Prof. Klaus Betzler for financial support during the first month of my PhD work.

I am very thankful for the external support I got. On very first place, I have to name Jaroslav Hamrle. His endless knowledge of magnetooptics and his strong patience made him the best cooperation partner I can think of. I hope this collaboration will last in the future.

Also many thanks to the people who prepared parts of the samples I investigated. This is Prof. Paul Fumagalli and his group and also Yuya Sakuraba and his team. For the support in Hamburg at DESY I want to thank Wolfgang Caliebe and Florian Bertram, for the support in Dortmund at DELTA I thank Christian Sternemann and Michael Paulus.

For technical support in Osnabrück I want to thank the mechanical and electrical workshops as well as Gregor Steinhoff from our group.

I was lucky to have very good co-workers at the MOKE setup, which I want to thank very much. These people are Tobias Becker, Hauke Bardenhagen and Henrik Wilkens. Also many thanks to Robin Schubert and Kamil Balinski for the programming assistance of the MOKE analysis tool and the MOKE setup control. Thanks and good luck to Tobias Schemme, who will manage the MOKE laboratory in the future during his PhD work.

The most important thing during work is to have people, who support you day by day, not only in science but also in the things you do else. These persons for me are my office colleagues Daniel Bruns, Sebastian Gevers and Martin Suendorf, which became really good friends in the last years. Thank you for all the good times, the good food and the important time outside the physics building ('janz piano ...')!

Also a big thanks to the rest of the workgroup. I hope you will enjoy the time here as much as I did. And don't forget: 'Support your local Arbeitsgruppenmitarbeiter!'

For reading parts of the manuscript and giving me very good correction suggestions I would like to thank Florian Bertram, Daniel Bruns, Sebastian Gevers, Jaroslav Hamrle, Tobias Schemme and Henrik Wilkens. I also want to thank the musicians of Billy Talent, Cara, die Toten Hosen, Knochenfabrik and Roxette for their fantastic music, which attended me the entire time in the last weeks during writing.

Now I come to the most important people I can acknowledge for their support, not only in the last years. This is what I call my 'family', which consists not only of my parents, grandparents and my sister's family. It also includes the best friends I have. Some of them I know for my entire life.

I want to say thank you to this complete family for so many years of friendship and support, for each crazy venture we were doing, for the balance from workaday life by making music, for the fact that you are here.

'to all my friends, present, past and beyond
even though they weren't with us too long
life is the most precious thing you can lose

while you were here the fun was never ending
laugh a minute was only the beginning
brothers and sisters, this one's for you!'

Jason Matthew Thirsk & Pennywise